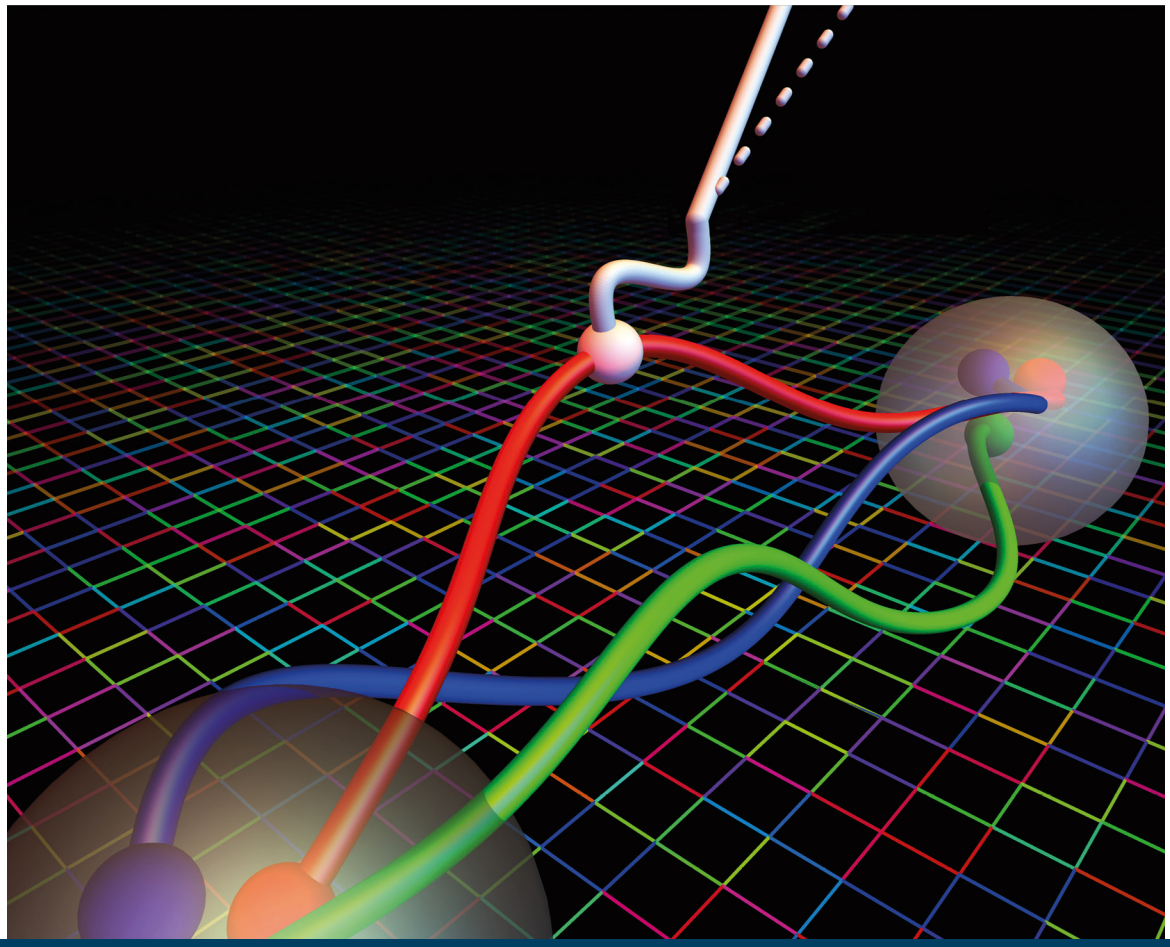

A lattice QCD study of nucleon structure with physical quark masses

Nesreen Hasan

IAS Series
Band / Volume 41
ISBN 978-3-95806-456-0

Mitglied der Helmholtz-Gemeinschaft

JÜLICH
Forschungszentrum

Schriften des Forschungszentrums Jülich
Reihe IAS Band / Volume 41

Forschungszentrum Jülich GmbH
Institute for Advanced Simulation (IAS)
Jülich Supercomputing Centre (JSC)

A lattice QCD study of nucleon structure with physical quark masses

Nesreen Hasan

Schriften des Forschungszentrums Jülich
Reihe IAS

Band / Volume 41

ISSN 1868-8489

ISBN 978-3-95806-456-0

Bibliografische Information der Deutschen Nationalbibliothek.
Die Deutsche Nationalbibliothek verzeichnet diese Publikation in der
Deutschen Nationalbibliografie; detaillierte Bibliografische Daten
sind im Internet über http://dnb.d-nb.de abrufbar.

Herausgeber und Vertrieb:	Forschungszentrum Jülich GmbH Zentralbibliothek, Verlag 52425 Jülich Tel.: +49 2461 61-5368 Fax: +49 2461 61-6103 zb-publikation@fz-juelich.de www.fz-juelich.de/zb
Umschlaggestaltung:	Grafische Medien, Forschungszentrum Jülich GmbH
Titelbild:	Wir danken E. Berkowitz / University of Maryland für das Bild, das für die Gestaltung des Covers verwendet wurde.
Druck:	Grafische Medien, Forschungszentrum Jülich GmbH
Copyright:	Forschungszentrum Jülich 2020

Schriften des Forschungszentrums Jülich
Reihe IAS, Band / Volume 41

D 468 (Diss. Wuppertal, Univ., 2019)

ISSN 1868-8489
ISBN 978-3-95806-456-0

Persistent Identifier: urn:nbn:de:0001-2020012307

Vollständig frei verfügbar über das Publikationsportal des Forschungszentrums Jülich (JuSER)
unter www.fz-juelich.de/zb/openaccess.

Abstract

In this work, we compute various nucleon structure observables using the lattice regularization of quantum chromodynamics, lattice QCD. Our calculations are performed using $2+1$-flavor ensembles with clover-improved Wilson fermions and cover three sets of observables:
The first set includes the computation of nucleon isovector axial, scalar, and tensor charges. In particular, we focus on controlling the unwanted contributions from excited states. Those charges quantify the coupling of nucleons to quark-level interactions and play an important role in the analysis of the Standard Model and Beyond the Standard Model (BSM) physics.
The second set of observables includes the nucleon charge and axial radii measured using a new and model-independent approach. We developed this approach to enable the computation of the nucleon radii directly at zero momentum transfer and avoid the systematic uncertainty originating from the large extrapolation commonly included in the conventional methods used for measuring quantities like the nucleon charge radius. Systematic errors of this kind have been proposed as a possible explanation of the radius puzzle which refers to the $> 5\sigma$ discrepancy between the experimental electronic and muonic determinations of the charge radius of the proton.
We perform the calculations of the nucleon charges and radii on two gauge ensembles at the physical pion mass and with different lattice spacings.
The last set of our calculation is devoted to measuring the nucleon axial form factors. This calculation includes both quark-connected and -disconnected diagrams, which allows us to determine the up, down, and strange form factors. This calculation is done using a single ensemble with pion mass 317 MeV.

Acknowledgments

This thesis would not have been possible without the constant support of many people. First and foremost I wish to express my sincerest gratitude to my advisor Prof.Thomas Lippert, for providing the opportunity to work on such a rich subject and for his nonstop support throughout the years. I also wish to express my gratitude to Stefan Krieg for accompanying me through this journey and for his outstanding support on the scientific level and his wonderful human qualities.

I am very fortunate to have been a part of such a supportive team, in particular, I highly appreciate having the chance to co-work with Jeremy Green who patiently guided me and limitlessly shared his scientific insights and experiences. I wish to extend my thanks to Stefan Meinel, Sergey Syritsyn, Michael Engelhardt, John Negele, and Andrew Pochinsky for the illuminating discussions and their substantial contribution to this study.

I thank my family, especially my parents, for their understanding and selfless support. Last but not least, I like to thank Farzin. He supported me with persistence in doing anything despite all the difficulties we faced together. His encouragements provided the fulfillment of this thesis.

Contents

List of Figures

List of Tables

Chapter 1

Introduction: Nucleon structure

Nucleons (protons and neutrons) are fundamental building blocks of the atomic matter and make up our visible universe. It was long believed that the proton is a point-like particle until the measurement of its magnetic moment by Stern in 1933. It was found that the magnetic moment of the proton is significantly larger than the magnetic moment of a point particle which provided a first evidence for the composite structure of the proton. Electron-nucleon scattering processes have been employed to probe the internal structure of the nucleon, e.g., the charge and magnetization density distributions of the nucleon. There are two classes of the scattering processes: elastic and deep-inelastic scattering. In electron-nucleon elastic scattering, the electron interacts with the nucleon via exchanging photons leaving the nucleon intact. By studying the cross section of this interaction combined with an internal charge density to describe the deviation from a point-like particle, it is possible to extract the electromagnetic form factors which encode the charge and magnetization distributions of the nucleons. While the elastic electron-nucleon scattering occurs at low energies, the deep inelastic scattering (DIS) occurs at high enough energies for the target to "shatter" into many new particles. The findings of the DIS experiments settled the parton picture of the nucleon, where the nucleon is considered as a composite particle consisting of point-like constituents, called partons, off which the electron scatters elastically. DIS guided the way to Quantum chromodynamics (QCD) as the theory describing the nucleons as bound states of quarks and gluons governed by the strong

interaction. Parton distribution functions (PDF) were introduced to describe the distribution of quarks and gluons within the nucleon.

In addition to the electromagnetic form factors, the axial form factor is an important quantity for understanding the spin structure of the nucleon. The axial form factor at zero momentum transfer is called the axial charge and can be interpreted as the fractional contribution from quark and antiquark spins to the nucleon spin. Experimentally, it is extracted from the beta decay of the neutron and its value is very accurately determined. On the other hand, the momentum transfer dependence of the axial form factor is much less well known. Experimentally, the axial form factor can be accessed in neutrino scattering off the nucleon or in the electro-production of charged pions and it is an important input to determine the neutrino flux in neutrino oscillation experiments.

The theory of QCD is a relativistic quantum field theory that describes the strong interaction between quarks which interacts by exchanging gluons. In QCD, both quarks and gluons carry the so-called color charge and thus the gluons not only interact with the quarks but they also experience self-interactions. This leads to *color confinement*, which is a key feature of QCD, according to which the strong coupling becomes large at low energies and only bound states of quarks and gluons exist, i.e., hadrons. At high energies, or equivalently short distances, the coupling becomes small, and quarks and gluons become asymptotically free. In the high energy regime, it is possible to use perturbation theory to perform theoretical calculations of various observables such as interaction cross sections, decay rates, and structure functions in deep inelastic processes. However, for studying nucleon structure we need to be in the low-energy regime, where the coupling is strong and the perturbative approach does not work. At present, the only way to solve QCD is by numerical simulation on an Euclidean space-time grid, i.e., lattice QCD. Lattice QCD is the only bridge between fundamental theory of strong interactions, on one side, and properties of hadrons, on the other. These properties include charge and magnetization distribution in the nucleon, and quark and gluon contributions to the nucleon spin and momentum, to name a few.

In this work, we study nucleon structure observables using the lattice QCD framework. The studies discussed in Chapters 3,4 and,5 were accomplished in collaboration with Jeremy Green, Stefan Krieg, Stefan Meinel, Michael Engelhardt, John Negele, Andrew Pochinsky, and Sergey Syritsyn. They are based on the published papers in Refs. [72, 66, 74, 75] and unpublished work in Ref. [73]. My contributions include:

- Implementing algorithms and writing running scripts.
- Running large scale simulations.
- Analyzing data, such as:
  - Computing nucleon observables, e.g., nucleon charges, form factors, and radii.
  - Performing renormalization [66]

The following sections give a brief description of the nucleon observables in which we are interested. These include the nucleon axial, scalar, and tensor charges, introduced in Sec. 1.1. In addition, we are interested in computing the nucleon electromagnetic and axial form factors, which we will briefly explain in Sec. 1.2. In particular, we measure the nucleon charge and axial radii which can be extracted from the electric and axial form factors. The nucleon charge radius is relevant to the so-called *proton radius puzzle* which we present in Sec. 1.2.1. In addition, we are interested in studying the spin structure of the nucleon through measuring the individual quark contributions to the axial form factors. This is related to the so-called *Nucleon spin puzzle*, which we talk about in Sec. 1.2.2.

1.1 Nucleon charges

Nucleon charges quantify the coupling of nucleons to quark-level interactions and play an important role in the analysis of the Standard Model and Beyond the Standard Model (BSM) physics. The isovector charges, g_X, are associated with the β-decay of the neutron into a proton and are defined via the transition matrix elements

$$\langle p(P,s)|\bar{u}\Gamma_X d|n(P,s)\rangle = g_X \bar{u}_p(P,s)\Gamma_X u_n(P,s) \tag{1.1}$$

where the Dirac matrix Γ_X is $1, \gamma_\mu\gamma_5$ and $\sigma_{\mu\nu}$ for the scalar (S), the axial (A) and the tensor (T) operators, respectively. They are straightforward to calculate in lattice QCD since they receive only connected contributions arising from the coupling of the operator to the valence quarks, i.e., there are no contributions from disconnected diagrams. See the coming section for a brief review on the connected and disconnected diagrams and Sec. 2.2.2 for more details.

The nucleon axial charge is experimentally well determined; the latest PDG value is $g_A = 1.2724(23)$ [117]. In addition to its role in beta decay, the axial charge gives the intrinsic quark spin in the nucleon, and its deviation from unity is a sign of chiral symmetry breaking. Since the axial charge is so well measured, it is considered to be a benchmark quantity for lattice calculations, and it is essential for lattice QCD to reproduce its experimental value.

Unlike the axial charge, the nucleon scalar and tensor charges are difficult to directly measure in experiments. Thus, the computation of these observables within lattice QCD will provide useful input for ongoing experimental searches for BSM physics. The generic BSM contributions to neutron beta decay were studied in Ref. [24], where it was shown that the leading effects are proportional to these two couplings; thus, calculations of g_S and g_T are required in order to find constraints on BSM physics from beta-decay experiments. The scalar charge relates the difference in u and d quark masses, $\delta m_q = m_d - m_u$, to the neutron-proton mass splitting in the absence of electromagnetism, $\delta M_N^{\rm QCD} = (M_n - M_p)_{\rm QCD}$ [58]

$$g_S = \delta M_N^{QCD}/\delta m_q. \tag{1.2}$$

The tensor charge is equal to the isovector first moment of the proton's transversity parton distribution function (PDF), $\langle 1 \rangle_{\delta u - \delta d}$. Constraining the experimental data with lattice estimates of the tensor charge reduces the uncertainty of the transversity PDF significantly [92]. The SoLID experiment at Jefferson Lab will greatly improve the experimental precision for g_T [122], providing a test of predictions from lattice QCD. In addition, the tensor charge controls the contribution of the quark electric

dipole moments (EDM) to the neutron EDM, which is an important observable in the search for new sources of CP violation.

Excited-state contamination is a source of significant systematic uncertainties in the calculation of nucleon structure observables. These contributions to different nucleon structure observables have been studied recently using baryon chiral perturbation theory (ChPT) [118, 70, 16]. Contamination from two-particle $N\pi$ states in the plateau estimates of various nucleon charges, which becomes more pronounced in physical-point simulations, has been studied in Ref. [16]. It was found that this particular contamination leads to an overestimation at the 5–10% level for source-sink separations of about 2 fm. This suggests that the source-sink separations of ~ 1.5 fm reached in present-day calculations may not be sufficient to isolate the contribution of the ground-state matrix element with the desired accuracy. On the other hand, in Ref. [70] a model was used to study corrections to the LO ChPT result for the axial charge; it was found that high-momentum $N\pi$ states with energies larger than about $1.5M_N$ can be the cause for the underestimating of the axial charge observed in lattice QCD calculations. These contributions, however, cannot be estimated in chiral perturbation theory.

Our calculations of the nucleon charges are presented in Chapter 3 where we perform an extensive study of excited-state effects using different analysis and fit strategies.

1.2 Nucleon form factors

Nucleon form factors are fundamental quantities that encode the internal structure of the nucleon. At low momentum transfer, the electromagnetic form factors parametrize the spatial distributions of charge and magnetization in the nucleon. In nonrelativistic systems, the electric and magnetic Sachs form factors, $G_E(Q^2)$ and $G_M(Q^2)$, are the Fourier transforms of the spatial distribution of the charge and magnetization inside the nucleon. The two axial form factors, $G_A(Q^2)$ and $G_P(Q^2)$, resolve the spin structure of the nucleon. The Fourier transform of the axial form factor can

be interpreted as the spatial distribution of polarized quarks in a polarized proton. The axial charge of the nucleon describes the fractional contribution from the quark and antiquark spins to the nucleon spin and is defined as the axial form factor at zero momentum transfer. As mentioned previously, electron scattering and atomic spectroscopy can be used to probe the electromagnetic form factors, whereas for the study of the axial form factors, which are far less known than the electromagnetic form factors, one has to rely on weak probes, i.e., neutrino scattering or muon capture processes.

In general, the different form factors parametrize the transition matrix elements of local operators between nucleon states. The nucleon matrix elements can be parametrized in terms of nucleon form factors as

$$\langle \vec{p}', \lambda' | \mathcal{O}_X^{q,\mu} | \vec{p}, \lambda \rangle = \bar{u}(\vec{p}', \lambda') \mathcal{F}_X^{q,\mu}(\vec{p}, \vec{p}') u(\vec{p}, \lambda), \tag{1.3}$$

where $\vec{p}$, $\vec{p}'$ are the initial and final nucleon momenta, λ, λ' label the different polarization states, and u is the nucleon spinor. We are defining the form factors using a current of flavor q in a proton and $|\vec{p}, \lambda\rangle$ is a proton state. $\mathcal{O}_X^{q,\mu}$ refers to either the vector ($X = V$) or the axial ($X = A$) current.

For the case of the vector current, $\mathcal{O}_V^{q,\mu} = \bar{q}\gamma^\mu q$, $\mathcal{F}_V^{q,\mu}(\vec{p}, \vec{p}')$ can be written in terms of the Dirac and Pauli form factors, $F_1^q(Q^2)$ and $F_2^q(Q^2)$, in Minkowski space as

$$\mathcal{F}_V^{q,\mu}(\vec{p}, \vec{p}') = \gamma^\mu F_1^q(Q^2) + \frac{i\sigma^{\mu\nu}(p'-p)_\nu}{2m_N} F_2^q(Q^2), \tag{1.4}$$

where m_N is the nucleon mass and $Q^2 = -(p'-p)^2 \geq 0$ is the momentum transfer. These form factors can also be expressed in terms of the nucleon electric $G_E(Q^2)$ and magnetic $G_M(Q^2)$ Sachs form factors via

$$G_E(Q^2) = F_1(Q^2) - \frac{Q^2}{4m_N^2} F_2(Q^2), \tag{1.5}$$

$$G_M(Q^2) = F_1(Q^2) + F_2(Q^2). \tag{1.6}$$

The charge and magnetic radii, $r^2_{E,M}$, and the magnetic moment, μ, are defined from the behavior of $G_{E,M}(Q^2)$ near $Q^2 = 0$

$$G^q_E(Q^2) = 1 - \frac{1}{6}(r^2_E)^q Q^2 + O(Q^4), \tag{1.7}$$

$$G^q_M(Q^2) = \mu^q \left(1 - \frac{1}{6}(r^2_M)^q Q^2 + O(Q^4)\right). \tag{1.8}$$

For the axial vector current, $\mathcal{O}^{q,\mu}_A = \bar{q}\gamma^\mu\gamma_5 q$, $\mathcal{F}^{q,\mu}_A(\vec{p},\vec{p}')$ can be expressed in terms of the axial and induced pseudoscalar form factors, $G^q_A(Q^2)$ and $G^q_P(Q^2)$, as

$$\mathcal{F}^{q,\mu}_A(\vec{p},\vec{p}') = \gamma^\mu\gamma_5 G^q_A(Q^2) + \gamma_5 \frac{(p'-p)^\mu}{2m_N} G^q_P(Q^2). \tag{1.9}$$

At small momentum transfer, the axial form factor can be expanded as

$$G^q_A(Q^2) = g^q_A \left(1 - \frac{1}{6}(r^2_A)^q Q^2 + O(Q^4)\right), \tag{1.10}$$

where g^q_A is the axial-vector coupling constant and r^q_A is the axial radius.

For computing the nucleon matrix elements of $\bar{q}q$ current operators on the lattice, we need to compute three-point correlation functions (see Sec. 2.2.2). The fermionic path integral of such functions results in two kinds of quark contractions: *connected*, where the operator is connected to the source and sink via quark propagators; and *disconnected*, where the operator is attached to a quark loop and connects with the valence quarks by gluons. Because nucleons contain only *up* and *down* valence quarks, connected diagrams arise only in the cases of $q \in \{u, d\}$. These connected contributions are easier to compute than the disconnected diagrams that arise for all quark flavours including the strange one. The quantum fluctuations in QCD give rise to contributions from the strange quarks even though those quarks are not part of the valence structure of the nucleon. Disconnected diagrams are thus necessary for all nucleon matrix elements except for those with isovector operators, i.e., $\bar{u}u - \bar{d}d$). The computation of quark-disconnected diagrams is significantly more demanding, since this requires calculating the quark propagator from all to all spatial coordinates, i.e., the exact inversion of the Dirac operator which has a rank $\sim O(10^9)$ for a typical

lattice calculation. This is not feasible even with modern supercomputers. Instead, algorithms have been developed lately which enable estimating the disconnected diagrams stochastically.

1.2.1 Proton radius puzzle

One of the fundamental properties of the proton that is still not completely understood is its charge radius. The proton charge radius has been measured experimentally using both scattering and spectroscopy experiments. The experimental determinations of the proton charge radius have a discrepancy greater than 5-sigma between the value determined from spectroscopy of muonic hydrogen [105, 7] and the CODATA average [99] of experimental results obtained from hydrogen spectroscopy and electron-proton scattering. This presently unresolved "proton radius puzzle" is the focus of various theoretical and experimental efforts. The CREMA collaboration has reported on their study of muonic deuterium [106]. Their experiment corroborates the muonic hydrogen result for the proton charge radius, while finding a similar 6-sigma discrepancy for the deuteron charge radius with the CODATA values, and a 3.5-sigma discrepancy to electronic deuterium spectroscopy results [107]. Thus, having a reliable ab-initio calculation of the proton charge radius is a highly attractive goal for calculations of lattice QCD.

In Chapter 4, we address the model uncertainty in the extraction of the proton charge radius, and similar quantities. The traditional method for computing quantities like the nucleon radius requires interpolation of form factors in the momentum transfer variable Q^2, which is quantized on a finite-size lattice. This interpolation is model-dependent and is difficult to control without increasing the volume of the lattice. In that chapter, we present a model-independent technique which we call *the derivative method*. This technique enables us to compute the nucleon radii exactly at $Q^2 = 0$ and helps to avoid the extrapolation included in the traditional method. In addition to the radii, we will use this technique to compute the values of form factors at zero momentum that cannot be extracted in the forward kinematics, such as the magnetic form factor $G_M(0)$ and the induced pseudoscalar form factor $G_P(0)$.

1.2.2 Proton spin puzzle

The so-called *proton spin puzzle* refers to the fact that up and down quark spins account less than 50% of the total proton spin. This was found by the European Muon Collaboration when measuring the spin asymmetry in polarized deep inelastic scattering [10]. The missing part of the nucleon $\frac{1}{2}$-spin must come from the orbital motion of quarks or from gluon angular momentum. According to the Ji's decomposition [82], the nucleon spin can be written as

$$\frac{1}{2} = J^g + \sum_q \left(\frac{1}{2}\Delta\Sigma^q + L^q \right), \quad \text{where} \quad L^q = J^q - \frac{1}{2}\Delta\Sigma^q, \tag{1.11}$$

where J^g is the gluon contribution, $\Delta\Sigma^q = g_A^q$ is the quark spin contribution, and L^q is the quark orbital momentum contribution.

In Chapter 5, we report a calculation of the nucleon axial form factors. This calculation includes both quark-connected and -disconnected diagrams. The calculation of the disconnected diagrams will be necessary to compute the contributions of individual quark polarizations to the proton spin $\frac{1}{2}\Delta\Sigma^q$. In addition, this calculation will allow us to determine the up, down, and strange axial form factors.

Axial form factors naturally arise in the interactions of nucleons with W and Z bosons. Assuming isospin symmetry, the W boson is sensitive to the $u - d$ flavor combination, whereas the Z boson is also sensitive to strange quarks. Neutron beta decay, mediated by W-boson exchange, is used to determine the "axial charge" $g_A \equiv g_A^{u-d}$. Quasielastic neutrino scattering, $\nu n \to \ell^- p$ or $\bar{\nu} p \to \ell^+ n$, has been used to measure the isovector axial form factor $G_A^{u-d}(Q^2)$, whereas elastic neutrino scattering is also sensitive to $G_A^s(Q^2)$.

A lattice QCD study of the axial form factors of the nucleon is timely not least in view of experimental efforts underway using the MicroBooNE liquid Argon time-projection chamber, which, in particular, will be able to map out the strange axial form factor of the nucleon to momentum transfers as low as $Q^2 = 0.08$ GeV^2 [102]. This is achieved by combining neutrino-proton neutral and charged current scattering

cross section measurements with available polarized electron-proton/deuterium cross section data, and is expected to reduce the experimental uncertainty of the extrapolated value at $Q^2 = 0$, i.e., the strange quark spin contribution Δs, by an order of magnitude. Such an extraction is complementary to polarized DIS determinations that access the strange quark helicity distribution function, but suffer from lack of coverage at low and high momentum fraction x when evaluating the first x-moment. The Q^2 range explored by the MicroBooNE experiment, between $Q^2 = 0.08$ GeV^2 and about $Q^2 = 1$ GeV^2, matches the range covered by the present lattice calculation well, enabling a future comparison of the Q^2-dependence obtained for the strange axial form factor.

Chapter 2

Nucleon structure on the lattice

In this chapter, we present techniques used in lattice QCD to compute nucleon structure observables. We begin with discussing the interpolating operators used for creating and annihilating of nucleons on the lattice in Sec. 2.1. In Sec 2.2, we review the computation of the nucleon two- and three-point correlation functions where we explain techniques for computing both connected and disconnected contributions to the three-point functions. We devote Sec. 2.3 to discuss the smearing of quark fields, Wuppertal smearing in particular. In Sec. 2.4, we describe the ratio and summation methods which are the main approaches we use in this work to extract matrix elements and control the excited-state contaminations. We show how to extract the nucleon electromagnetic and axial form factors from the corresponding matrix elements in Sec. 2.5. Finally, we explain the Rome-Southampton approach for computing renormalization factors on the lattice in Sec. 2.6.

2.1 Nucleon field

The first step for performing nucleon calculations on the lattice is to identify the interpolating operator for creating and annihilating nucleons. This operator should possess the correct quantum numbers (parity, spin, and isospin) of the nucleon and be a color singlet. The interpolating operator of a composite particle like the nucleon is built from the interpolating operators of its constituent quarks. A typical choice

for the interpolating field for the proton which contains uud quark flavours and has an isospin $I = \frac{1}{2}$ and spin $S = \frac{1}{2}$ is

$$\chi_\alpha(x) = \epsilon^{abc} u^a_\alpha(x) \left[u^{b^T}(x) C\gamma_5 d^c(x) \right], \tag{2.1}$$

where ϵ^{abc} is an antisymmetric tensor with color indices which ensures that the interpolator is colorless and thus gauge invariant. The charge conjugation matrix, C, is defined as $C = \gamma_4\gamma_2$ and the transpose acts in Dirac space. The term in the brackets has spin $S = 0$ and $I = 0$ which means that the interpolator has a total spin $I = \frac{1}{2}$ and it is a 4-component spinor field with Dicac index α.

It is important to mention that the interpolating operator in Eq. (2.1) couples to all the particles with the same quantum numbers as the nucleon and it is not unique. In particular, there exist two other site-local interpolating operators for the proton, namely

$$\chi'_\alpha = \epsilon^{abc} u^a_\alpha \left[u^{b^T} C\gamma_5\gamma_4 d^c \right] \text{ and } \chi''_\alpha = \epsilon^{abc} u^a_\alpha \gamma_5 \left[u^{b^T} C d^c \right]. \tag{2.2}$$

Furthermore, one can remove the lower components of the quark fields without significantly reducing the overlap of the nucleon operator with the physical proton. This is done using

$$\psi^+ = \frac{1+\gamma_4}{2}\psi, \tag{2.3}$$

where ψ is the quark field. This process results in an operator which is equivalent to the linear combination of $\chi + \chi'$ and it is practical for two reasons. Firstly, the resulting nucleon operator is projected automatically to the positive parity. Secondly, it reduces the number of Dirac operator inversions required for computing the quark propagator by a factor of two (from $N_s.N_c = 12$ to 6) since only the two upper components of the nucleon operator are involved in the calculation.

In the subsequent sections, we will use the following convenient parametrization of the interpolating operator

$$\chi_\alpha(x) = \epsilon^{abc} f_{\alpha\beta\gamma\delta}\ u^a_\beta(x) u^b_\gamma(x) d^c_\delta(x), \tag{2.4}$$

where $f_{\alpha\beta\gamma\delta}$ is the spin tensor determining the quantum numbers of the nucleon field

$$f_{\alpha\beta\gamma\delta} = \left(\frac{1+\gamma_4}{2}\right)_{\alpha\beta} \left(\frac{1+\gamma_4}{2}\, C\gamma_5\right)_{\gamma\delta}. \tag{2.5}$$

We express the interpolating operator for the antinucleon as

$$\bar{\chi}_{\alpha'} = (\chi)^\dagger_\alpha (\gamma_4)_{\alpha\alpha'} \tag{2.6}$$

$$= \left(f_{\alpha\beta\gamma\delta} u_\beta u_\gamma d_\delta\right)^\dagger (\gamma_4)_{\alpha'\alpha} \tag{2.7}$$

$$= \bar{f}_{\alpha'\beta'\gamma'\delta'} \bar{d}_{\delta'} \bar{u}_{\gamma'} \bar{u}_{\beta'}, \tag{2.8}$$

where

$$\bar{f}_{\alpha'\beta'\gamma'\delta'} = f^*_{\alpha\beta\gamma\delta} (\gamma_4)_{\alpha'\alpha} (\gamma_4)_{\beta'\beta} (\gamma_4)_{\gamma'\gamma} (\gamma_4)_{\delta'\delta}, \tag{2.9}$$

and the antisymmetrization over the color indices is implied.

2.2 Nucleon correlation functions

Hadron structure observables are extracted using the Euclidean correlation functions on the lattice. In this section, we discuss how to construct the two- and three-point nucleon correlation functions. Sec. 2.2.1 includes a discussion about the construction of two-point functions and their spectral decomposition. In Sec. 2.2.2, we discuss the construction of the three-point function.

2.2.1 Two-point correlation function

The basic nucleon two-point function is a Green's function, defined as

$$C_2^{\alpha,\beta}(x, x_0) = \langle \Omega | \chi_\alpha(x) \bar{\chi}_\beta(x_0) | \Omega \rangle, \tag{2.10}$$

where we refer to $x = (\vec{x}, t)$ as the source position and $x_0 = (\vec{x}_0, t_0)$ as the sink position. $\langle \cdots \rangle$ denotes the full QCD expectation value. The time component $t - t_0$ is called the source-sink separation. Translation invariance implies that the two-point

correlator is only a function of $x - x_0$ which allows setting $x_0 = (\vec{0}, 0)$ for simplicity; the x dependency can be restored by replacing $x \to (x - x_0)$ in all expressions.

Spectral decomposition and ground-state contribution

The spectral decomposition of the two-point correlator can be obtained by using the transfer matrix formalism after applying Fourier transform to project the nucleon to a definite momentum

$$C_2^{\alpha\beta}(\vec{p}, t) = \sum_{\vec{x}} e^{-i\vec{p}\vec{x}} \langle \Omega | \chi_\alpha(x) \bar{\chi}_\beta(0) | \Omega \rangle. \tag{2.11}$$

Inserting a complete set of states $I = \sum_n |n\rangle\langle n|$ and exploiting the Euclidean time evolution operator, $\chi_\alpha(\vec{x}, t) = e^{\hat{H}t} \chi_\alpha(\vec{x}, 0) e^{-\hat{H}t}$, lead to

$$C_2^{\alpha\beta}(\vec{p}, t) = \sum_{\vec{x}} e^{-i\vec{p}\vec{x}} \langle \Omega | \chi_\alpha(x) \bar{\chi}_\beta(0) | \Omega \rangle \tag{2.12}$$

$$= \sum_{\vec{x}} e^{-i\vec{p}\vec{x}} \sum_n e^{-E_n t} \langle \Omega | \chi_\alpha(\vec{x}) | n \rangle \langle n | \chi_\beta(0) | \Omega \rangle, \tag{2.13}$$

where the sum is over states with the same quantum numbers as the nucleon and energies E_n.

Next, we label proton states as $|\vec{p}, \lambda\rangle$. Nucleon states are normalized such that

$$\langle p', \lambda' | p, \lambda \rangle = 2E(\vec{p}) L_s^3 \delta_{\vec{p}', \vec{p}} \delta_{\lambda', \lambda}, \tag{2.14}$$

where L_s is the spatial extension of the lattice. This yields the standard relativistic normalization in the infinite-volume limit. The overlap with the nucleon is parametrized as

$$\langle \Omega | \chi_\alpha(\vec{x}) | \vec{p}, \lambda \rangle = Z(\vec{p}) e^{i\vec{p}\vec{x}} u_\alpha(p, \lambda), \tag{2.15}$$

where u_α is the nucleon spinor and the overlap factor $Z(\vec{p})$ measures how much of the state $|\vec{p}, \lambda\rangle$ is created by the nucleon operator χ [31, 38]. Typical calculations of the two-point correlator include tracing $C_2^{\alpha\beta}$ after multiplying it by the parity-spin

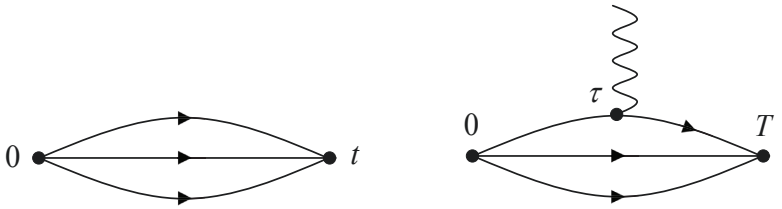

Figure 2-1: Graphical illustration of the two-point (left) and three-point (right) correlation functions.

projector $\Gamma_{\rm pol}$ as

$$C_2(\vec{p},t) = (\Gamma_{\rm pol})_{\beta\alpha} C_2^{\alpha\beta}(\vec{p},t). \tag{2.16}$$

The two-point function can then be written as

$$\begin{aligned} C_2(\vec{p},t) &= \sum_{\vec{x}} e^{-i\vec{p}\vec{x}} (\Gamma_{\rm pol})_{\beta\alpha} \langle\Omega|\chi_\alpha(x)\bar{\chi}_\beta(0)|\Omega\rangle \\ &= \sum_{\vec{p}',\lambda} \frac{e^{-E(\vec{p}')t}}{2E(\vec{p}')L^3} \sum_{\vec{x}} e^{i(\vec{p}'-\vec{p})\vec{x}} Z(\vec{p}')^2 \,\mathrm{Tr}\left[\Gamma_{\rm pol} u(\vec{p}',\lambda)\bar{u}(\vec{p}',\lambda)\right] \left(1+O(e^{-\Delta E_{10}(\vec{p})t})\right) \\ &= \frac{Z(\vec{p})^2 e^{-E(\vec{p})t}}{2E(\vec{p})} \,\mathrm{Tr}\left[\Gamma_{\rm pol}\left(\not{p}+m_N\right)\right] \left(1+O(e^{-\Delta E_{10}(\vec{p})t})\right). \end{aligned} \tag{2.17}$$

In the last step, we use the spin sum completeness relation for spinors

$$\sum_{\lambda} u(\vec{p},\lambda)\bar{u}(\vec{p},\lambda) = \not{p} + m_N, \tag{2.18}$$

with $\not{p} = E(\vec{p})\gamma_4 - i\vec{p}\vec{\gamma}$ in the Euclidean space. $\Delta E_{10}(\vec{p})$ is the energy gap between the ground and the lowest excited state with momentum $\vec{p}$. In our studies, we use $\Gamma_{\rm pol} = \frac{1}{4}(1+\gamma_4)(1-i\gamma_3\gamma_5)$. As the Euclidean time evolves, excited states are exponentially suppressed and the ground-state nucleon dominates.

Two-point correlator at quark level

Here, we express the nucleon two-point correlator in terms of quark propagators. We start from our notation for the nucleon interpolating operator given in Eq. (2.4), the proton two-point correlation function reads

$$\begin{aligned} C_2^{\alpha\beta}(\vec{x},t) &= \langle \chi_\alpha(x)\bar{\chi}_\beta(0)\rangle \\ &= \epsilon^{abc}\epsilon^{efg} f_{\alpha\gamma\delta\epsilon}\bar{f}_{\beta\zeta\eta\theta}\ \left\langle u^a_\gamma(x)u^b_\delta(x)\, d^c_\epsilon(x)\, \bar{d}^e_\zeta(0)\, \bar{u}^f_\eta(0)\, \bar{u}^g_\theta(0)\right\rangle \\ &= \epsilon^{abc}\epsilon^{efg} f_{\alpha\gamma\delta\epsilon}\bar{f}_{\beta\zeta\eta\theta}\times \\ &\quad \left\langle S^{ce}_{d,\epsilon\zeta}(x,0)\left[S^{ag}_{u,\gamma\theta}(x,0)S^{bf}_{u,\delta\eta}(x,0) - S^{af}_{u,\gamma\eta}(x,0)S^{bg}_{u,\delta\theta}(x,0)\right]\right\rangle_U, \end{aligned} \tag{2.19}$$

where in the last step, we contract all possible quark fields and use $S^{ab}_{q,\alpha\beta} = [D_q^{-1}]^{ab}_{\alpha\beta} = \langle q^a_\alpha \bar{q}^b_\beta\rangle_F$ to denote quark propagators where D is the Dirac operator. Above, we refer to the fermionic expectation value by $\langle\cdots\rangle_F$ and to the average over gauge fields by $\langle\cdots\rangle_U$. The nucleon two-point function is schematically illustrated in the left part of Fig. 2-1.

2.2.2 Three-point correlation function

The three-point function is defined as

$$C_3^{\mathcal{O},\alpha\beta}(x,y) = \left\langle \Omega\middle|\chi_\alpha(x)\mathcal{O}(y)\bar{\chi}_\beta(0)\middle|\Omega\right\rangle, \tag{2.20}$$

which is illustrated in the right part of Fig. 2-1, where a particle is created at $t = 0$ by the creation operator, interacts with the generic current $\mathcal{O}(y)$ with $y = (\vec{y},\tau)$ and is annihilated at $x = (\vec{x},T)$ by the annihilation operator. In analogy to the two-point correlator and due to translation invariance of the three-point correlator, we set the source position in Eq. (2.20) to zero for simplicity. We are interested in three-point functions obtained from quark-biliear operators with the form $\mathcal{O} = \bar{q}\Gamma q$ where Γ stands for any combination of γ-matrices and derivatives (e.g. γ_μ for the electromagnetic current).

Spectral decomposition and ground-state contribution

As in the case of the two-point correlation function, we define a momentum-projected three-point function

$$C_3^{\mathcal{O},\alpha\beta}(\vec{p},\vec{p}',\tau,T) = \sum_{\vec{x},\vec{y}} e^{-i\vec{p}'.\vec{x}} e^{i(\vec{p}'-\vec{p}).\vec{y}} \left\langle \chi_\alpha(\vec{x},T)\mathcal{O}(\vec{y},\tau)\bar{\chi}_\beta(\vec{0},0)\right\rangle, \tag{2.21}$$

where $\vec{p}$ and $\vec{p}'$ are the initial- and final-state momenta. The spectral representation of the three-point function can be straightforwardly derived from the transfer matrix formalism

$$\begin{aligned} C_3^{\mathcal{O},\alpha\beta}(\vec{p},\vec{p}',\tau,T) = &\sum_{n,n'} e^{-E_{n'}(T-\tau)} e^{-E_n\tau} \\ &\times \sum_{\vec{x},\vec{y}} e^{-i\vec{p}'\vec{x}} e^{-i(\vec{p}'-\vec{p})\vec{y}} \langle\Omega|\chi_\alpha(\vec{x})|n\rangle\langle n|\mathcal{O}(\vec{y})|n'\rangle\langle n'|\bar{\chi}_\beta(0)|\Omega\rangle. \end{aligned} \tag{2.22}$$

Following the same methodology from previous section (Eq. (2.14) and Eq. (2.15)) and taking the asymptotic limit $T-\tau \to \infty$ and $\tau \to \infty$, the contribution from the ground state dominates and has the following form after applying spin projection

$$\begin{aligned} C_3^{\mathcal{O}}(\vec{p},\vec{p}',\tau,T) =& \frac{Z(\vec{p}')Z(\vec{p})e^{-E(\vec{p}')(T-\tau)}e^{-E(\vec{p})\tau}}{4E(\vec{p}')E(\vec{p})} \sum_{\lambda',\lambda} (\Gamma_{\rm pol})_{\beta\alpha} u_\alpha(p',\lambda')\langle p',\lambda'|O|p,\lambda\rangle \bar{u}_\beta(p,\lambda) \\ &\times \left(1 + O(e^{-\Delta E_{10}(\vec{p})\tau}) + O(e^{-\Delta E_{10}(\vec{p}')(T-\tau)})\right) \\ =& \frac{Z(\vec{p}')Z(\vec{p})e^{-E(\vec{p}')(T-\tau)}e^{-E(\vec{p})\tau}}{4E(\vec{p}')E(\vec{p})} \mathrm{Tr}\left[\Gamma_{\rm pol}(\not{p}' + m_N)\mathcal{F}(\not{p} + m_N)\right] \\ &\times \left(1 + O(e^{-\Delta E_{10}(\vec{p})\tau}) + O(e^{-\Delta E_{10}(\vec{p}')(T-\tau)})\right), \end{aligned} \tag{2.23}$$

where we obtain Eq. (2.23) after assuming $\langle p',\lambda'|\mathcal{O}|p,\lambda\rangle = \bar{u}(p',\lambda')\mathcal{F}u(p,\lambda)$, where $\mathcal{F}$ contains the form factors that we are usually interested in. For extracting the matrix element $\langle p',\lambda'|\mathcal{O}|p,\lambda\rangle$ or the form factors $\mathcal{F}$, we build ratios of three- and two-point functions to remove the unknown overlap with the vacuum and the Euclidean time dependence. This is discussed in Sec. 2.4. Increasing T suppresses excited-state contamination, but it also increases the noise; the signal-to-noise ratio is expected to

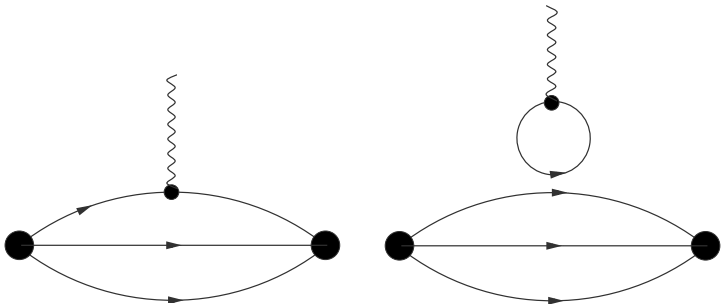

Figure 2-2: Wick contractions of quark fields in three-point correlators. The connected part (left) and disconnected part (right), of a three-point function coupled to a biliear operator.

decay asymptotically as $e^{-(E-\frac{3}{2}m_\pi)T}$ [90].

Three-point correlator at the quark level

As for the two-point function, we want to write the three-point function in terms of quark propagators. The contraction pattern in this case depends on the flavor of the fields q and $\bar{q}$ used in the bilinear operator $\mathcal{O} = \bar{q}\Gamma q$ and we distinguish between this operator inserted on a u- or d-quark lines

$$\mathcal{O}^u(\vec{y},\tau) = \bar{u}(y)\Gamma u(y), \qquad \text{and} \qquad \mathcal{O}^d(\vec{y},\tau) = \bar{d}(y)\Gamma d(y). \tag{2.24}$$

The simpler case is for $\mathcal{O}^d$ where we have

$$C_3^{\mathcal{O}^d,\alpha\beta}(x,y) = \epsilon^{abc}\epsilon^{efg} f_{\alpha\gamma\delta\epsilon}\bar{f}_{\beta\zeta\eta\theta}\Gamma_{\mu\nu}\left\langle u^a_\gamma(x) u^b_\delta(x) d^c_\epsilon(x)\, \bar{d}^h_\mu(y) d^h_\nu(y)\, \bar{d}^e_\theta(0)\bar{u}^f_\eta(0)\bar{u}^g_\zeta(0)\right\rangle . \tag{2.25}$$

After performing all possible connected Wick contractions, we obtain

$$C_3^{\mathcal{O}^d,\alpha\beta}(x,y)\big|_{conn} = \epsilon^{abc}\epsilon^{efg} f_{\alpha\gamma\delta\epsilon}\bar{f}_{\beta\zeta\eta\theta}\Gamma_{\mu\nu}\Big\langle S^{ch}_{d,\epsilon\mu}(x,y) S^{he}_{d,\nu\theta}(y,0)\times \big[S^{af}_{u,\gamma\eta}(x,0)S^{bg}_{u,\delta\zeta}(x,0) - S^{ag}_{u,\gamma\zeta}(x,0)S^{bf}_{u,\delta\eta}(x,0)\big]\Big\rangle_U . \tag{2.26}$$

Inserting the operator onto a u-quark line leads to more Wick contractions and we obtain

$$C_3^{\mathcal{O}^u,\alpha\beta}(x,y)\big|_{conn} = \epsilon^{abc}\epsilon^{efg} f_{\alpha\gamma\delta\epsilon}\bar{f}_{\beta\zeta\eta\theta}\Gamma_{\mu\nu}\Big\langle S^{ce}_{d,\epsilon\theta}(x,0)\times \\ \big[S^{ah}_{u,\gamma\mu}(x,y)S^{bf}_{u,\delta\eta}(x,0)S^{hg}_{u,\nu\zeta}(y,0) \\ + S^{ag}_{u,\gamma\zeta}(x,0)S^{bh}_{u,\delta\mu}(x,y)S^{hf}_{u,\nu\eta}(y,0) \\ - S^{ah}_{u,\gamma\mu}(x,y)S^{bg}_{u,\delta\zeta}(x,0)S^{hf}_{u,\nu\eta}(y,0) \\ - S^{af}_{u,\gamma\eta}(x,0)S^{bh}_{u,\delta\mu}(x,y)S^{hg}_{u,\nu\zeta}(y,0)\big]\Big\rangle_U. \tag{2.27}$$

In Eq. (2.26) and Eq. (2.27), we give only the quark-connected contractions. However, in all cases there are quark-disconnected contractions

$$C_3^{\mathcal{O}^q,\alpha\beta}(x,y)\big|_{disconn} = \epsilon^{abc}\epsilon^{def} f_{\alpha\gamma\delta\epsilon}\bar{f}_{\beta\zeta\eta\theta}\Gamma_{\mu\nu}\Big\langle S^{hh}_{q,\mu\nu}(y,y)S^{ce}_{d,\epsilon\theta}(x,0)\times \\ \big[S^{ae}_{u,\gamma\zeta}(x,0)S^{bf}_{u,\delta\eta}(x,0) - S^{af}_{u,\delta\eta}(x,0)S^{be}_{u,\delta\zeta}(x,0)\big]\Big\rangle_U, \tag{2.28}$$

where $S_q \equiv S_u$ for *up*-quark current insertion and $S_q \equiv S_d$ for *down*-quark current. The disconnected contractions give non-trivial contributions because the quark loop in Fig. 2-2 (right) is evaluated in the presence of the gluon background that connects this loop with the valence quark lines by virtual gluon exchange. Furthermore, the disconnected contributions to the three-point correlation function cancel out in the case of isovector operator, $\mathcal{O}^{u-d} = \bar{u}\Gamma u - \bar{d}\Gamma d$, with two degenerate light flavours.

We evaluate the connected and disconnected diagrams differently. We compute the connected diagrams using sequential propagators through the sink. The disconnected diagrams are equal to the correlation between a nucleon two-point function and a disconnected loop. For evaluating the disconnected loops, we use stochastic-estimation methods. In the coming subsections, we illustrate the approaches we follow for evaluating both the connected and disconnected contributions to the three-point function.

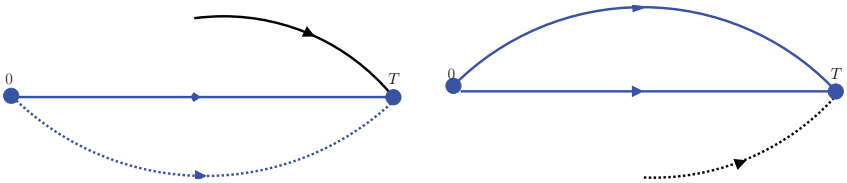

Figure 2-3: Schematic illustration of the Σ term for u-type (left) and d-type operators (right). The dotted lines indicate a d-quark propagator and the solid line indicates a u-quark propagator. The blue combination of propagators refers to $S^{u,d}_{\Gamma_{\rm pol}}$. The black propagator is the sequential one.

Evaluating connected diagrams

For evaluating the connected part of the three-point correlation function, we use the so-called *sequential-propagator technique*. We explain the procedure for computing the sequential propagator using the simpler case of $\mathcal{O}^d(\vec{y},\tau)$ but a similar procedure can be followed for $\mathcal{O}^u(\vec{y},\tau)$. We start by the momentum-projected three-point function

$$C_3^{\mathcal{O}^d}(\vec{p},\vec{p}',\tau,T)\Big|_{conn} = \sum_{\vec{x},\vec{y}} e^{-i\vec{p}'\vec{x}} e^{i(\vec{p}'-\vec{p})\vec{y}}\,\mathrm{Tr}\left[\Gamma_{\rm pol} C_3^{\mathcal{O}^d}(x,y)\Big|_{conn}\right]. \tag{2.29}$$

For evaluating Eq. (2.29) and as we see in Eq. (2.25), we need to compute three propagators

$$S_u(x,0), \qquad S_d(y,0), \text{ and} \qquad S_d(x,y). \tag{2.30}$$

The first two with fixed sources can be computed as point-source propagators. However, for computing $S_d(x,y)$ we need an all-to-all propagator, i.e from all points $\vec{y}$ to all points $\vec{x}$. The computation of such a propagator is a numerically demanding task since it requires inverting the Dirac operator for all L_s^3 lattice sites in the spatial volume. The workaround is to use the sequential-propagator technique [95] in which we fix either the sink position or the operator insertion point.

The main idea of the the sequential-propagator method is to write the three-point correlator as a product of propagators

$$C_3^{\mathcal{O}^d}(\vec{p},\vec{p}',\tau,T)\Big|_{conn} = \sum_{\vec{y}} e^{i(\vec{p}'-\vec{p})\vec{y}} \Big\langle\, \mathrm{Tr}\left[\Sigma^d_{\Gamma_{\rm pol}}(y,0;\vec{p}',T)\Gamma S_d(y,0)\right] \Big\rangle_U. \tag{2.31}$$

The term $\Sigma^d_{\Gamma_{\rm pol}}$ contains a combination of the propagators shown in Fig. 2-3 and can be written as

$$\Sigma^d_{\Gamma_{\rm pol}}(y,0;\vec{p}',T) = \sum_{\vec{x}} S^d_{\Gamma_{\rm pol}}(x,0;\vec{p}')S(x,y), \tag{2.32}$$

where $S^d_{\Gamma_{\rm pol}}$ is defined as

$$S^{d;ce}_{\Gamma_{\rm pol}}(x,0;\vec{p}') = e^{-i\vec{p}'\vec{x}}\epsilon^{abc}\epsilon^{efg}(\Gamma_{\rm pol})_{\beta\alpha}f_{\alpha\gamma\delta\epsilon}\bar{f}_{\beta\zeta\eta\theta} \left[S^{ae}_{u,\gamma\zeta}(x,0)S^{bf}_{u,\delta\eta}(x,0) - S^{ag}_{u,\gamma\zeta}(x,0)S^{bf}_{u,\delta\eta}(x,0)\right]. \tag{2.33}$$

Fixing the sink position allows us to compute the sequential propagator $\Sigma^{u,d}_{\Gamma_{\rm pol}}(y,0;\vec{p}',T)$ via a second inversion by solving the linear system of equations

$$\sum_y D(x,y)\gamma_5\Sigma^{\dagger\,d}_{\Gamma_{\rm pol}}(y,0;\vec{p}',T) = \gamma_5 S^{\dagger\,d}_{\Gamma_{\rm pol}}(x,0;\vec{p}'), \tag{2.34}$$

where we use the γ_5-hermiticity relation of the Dirac operator, $\gamma_5 D(x,y)\gamma_5 = D^\dagger(y,x)$. Constructing the three-point function in Eq. (2.31) can be then achieved by contracting the sequential propagator with the ordinary propagator, $S(y,0)$. We intend to study a large set of operators, so it is advantageous to use the fixed-sink method. The disadvantage of the fixed-sink method is that a new inversion should be done for each source-sink separation T and each projector $\Gamma_{\rm pol}$.

Evaluating disconnected diagrams

The contribution to the three-point nucleon function from disconnected diagrams is given in Eq. (2.28). Evaluating this contribution requires computing a *disconnected loop* which is defined as

$$T_q(\vec{p},\vec{p}',t,\Gamma) \equiv -\sum_{\vec{y}} e^{i(\vec{p}'-\vec{p})\cdot\vec{y}}\,{\rm Tr}\left[\Gamma S_q(y,y)\right], \tag{2.35}$$

where $y=(\vec{y},t)$, $q\in\{u,d\}$, and the trace is over color and spin indices. An exact computation of the trace of the all-to-all propagator in Eq. (2.35) would be proportional

to the lattice volume, instead, stochastic methods are employed. The disconnected contribution to C_3 can then be obtained from the correlation between this loop and the nucleon two-point function.

The standard method for evaluating the disconnected loops stochastically involves computing the Monte Carlo averaging over matrix quadratures with random noise vectors

$$\mathrm{Tr}(\Gamma S_q) = \frac{1}{N}\sum_{n=1}^{N} \eta_n^\dagger \Gamma S_q \eta_n, \tag{2.36}$$

where the η_n are random noise vectors. In this work, we generate noise fields $\eta_{a\alpha}(x)$ that have color, spin, and space-time indices but with support only on a single timeslice, t. We use one $\mathbb{Z}_2 + i\mathbb{Z}_2$ noise vector for each chosen timeslice and gauge configuration, i.e., the components of η are randomly chosen from $\{\frac{1+i}{\sqrt{2}}, \frac{1-i}{\sqrt{2}}, \frac{-1+i}{\sqrt{2}}, \frac{-1-i}{\sqrt{2}}\}$. As a result, the diagonal elements of $\eta\eta^\dagger$ are equal to 1, and the off-diagonal elements are random with expectation value zero.

In order to reduce noise by replacing statistical zeros with exact zeros in targeted off-diagonal components of $\eta\eta^\dagger$, we use color and spin dilution [120, 55], as well as hierarchical probing [115]. The former makes use of a complete set of twelve projectors in color and spin space, P_d, such that $P_d\eta$ has support on only one color and one spin component. The latter makes use of N_{hvec} specially-constructed spatial *Hadamard vectors*, z_n, which have values ± 1 on the lattice sites and provide a scheme for progressively eliminating the spatially near-diagonal contributions to the noise. Combining these yields $12N_{\mathrm{hvec}}$ modified noise fields

$$\eta_{a\alpha}^{[d,n]}(\vec{y}) = \sum_{b,\beta} (P_d)_{a\alpha}^{b\beta} z_n(\vec{y}) \eta_{b\beta}(\vec{y}). \tag{2.37}$$

We use these as sources for quark propagators, $\zeta^{[d,n]} = S_q \eta^{[d,n]}$, and obtain an estimator for $T(\vec{p}, \vec{p}', t, \Gamma)$

$$\frac{-1}{N_{\mathrm{hvec}}} \sum_{d,n} \sum_{\vec{y}} e^{i(\vec{p}'-\vec{p})\cdot\vec{y}} \eta^{[d,n]\dagger}(\vec{y}, t) \Gamma \zeta^{[d,n]}(\vec{y}, t). \tag{2.38}$$

2.3 Smearing of quark fields

As mentioned previously, the local and point-like nucleon interpolating field used so far (see Eq. (2.1)) contains all physical states with the allowed symmetries and is known to have a poor overlap with the ground state. An extended nucleon creation operator can be constructed using smeared quark fields which enhances the overlap with the ground state and thus reduces contamination from excited states at early Euclidean times. For smearing sources in our study, we use the Wuppertal smearing where a smooth kernel $K(x)$ is applied to a regular quark field $\psi(x)$ which yields a smeared quark field $\tilde{\psi}(x)$

$$\tilde{\psi}(x) = \int dx K(x - x')\psi(x'). \tag{2.39}$$

The smeared nucleon field becomes

$$\tilde{\chi}(x) = \chi\left(\tilde{u}(x), \tilde{u}(x), \tilde{d}(x)\right). \tag{2.40}$$

The Gaussian or Wuppertal smearing kernel has the form

$$K = \left(1 - \frac{\sigma^2}{4N_W}\nabla^2\right)^{N_W} = \left(1 - \frac{3\sigma^2}{2N_W}\right)^{N_W} (1 + \alpha H)^{N_W}, \tag{2.41}$$

where Δ is the gauge-covariant spatial Laplacian, $\alpha = \frac{\sigma^2/4N_W}{1-3\sigma^2/2N_W}$ and H is the hopping matrix

$$H\psi(x) = \sum_{i=1}^{3} \left(\tilde{U}_i(x)\psi(x + \hat{i}) + \tilde{U}_i^{\dagger}(x - \hat{i})\psi(x - \hat{i})\right), \tag{2.42}$$

where $\tilde{U}$ is the gauge field. Typically, one uses smeared gauge fields to reduce fluctuations. In this study, we use the HEX gauge-covariant procedure [34] to obtain $\tilde{U}$. The Gaussian smearing parameters, σ and N_W of the smearing kernel in Eq. (2.41), influence the size and shape of the "Gaussian" profile and both are used to tune the

Ensemble	α	N_W	σ
Fine	3	100	7.95
Coarse	3	60	6.16

Table 2.1: The parameters of the Wuppertal smearing for lattices used in this work.

r.m.s radius of the smeared quark fields. The r.m.s radius is defined as

$$r_{\mathrm{rms}} = \langle r^2 \rangle^{\frac{1}{2}} = \left[\frac{d^3x |\vec{x}|^2 |\psi(\vec{x})|^2}{\int d^3x |\psi(\vec{x})|^2} \right]^{\frac{1}{2}}. \tag{2.43}$$

The r.m.s radius describes the width of the quark wave function. We list the parameters of the Wuppertal smearing used in this work in Tab. 2.1. The smearing results in an approximately Gaussian shaped sources with $r_{\mathrm{rms}} \sim 0.56$ fm on both ensembles.

The quark smearing is achieved by applying the smearing kernel to a point-source vector before inversion (source smearing)

$$\sum_{y,\beta,d} D(x,y)^{cd}_{\alpha\beta} \tilde{S}(y,x_0)^{dc_0}_{\beta\alpha_0} = K(x,z)^{ce}_{\alpha\gamma} \delta_{zx_0} \delta_{\gamma\alpha_0} \delta_{ec_0}. \tag{2.44}$$

Applying the smearing kernel also to the source-smeared propagator leads to the smeared-smeared quark propagator $\tilde{\tilde{S}}$, which is smeared at the source and at the sink

$$\tilde{\tilde{S}}(x,z)^{ce}_{\alpha\gamma} = K(x,y)^{cd}_{\alpha\beta} \tilde{S}^{de}_{\beta\gamma}. \tag{2.45}$$

In this way, we obtain a symmetric smearing procedure at the source and sink, which results in identical overlap coefficients in the three-point functions.

2.4 Computation of matrix elements

2.4.1 Ratio method

Computing the nucleon two- and three-point functions is the first step for determining the nucleon matrix elements, $\langle p', \lambda' | \mathcal{O} | p, \lambda \rangle$, see Eq. (2.17) and Eq. (2.23). For isolating the matrix elements, we need to cancel the overlap factors and the dependence on Euclidean time in those equations. For that, we construct the ratio of the three- and two-point correlation functions. We define the *normalization ratio*, $R_N^{\mathcal{O}}$, and the *asymmetry ratio*, R_S, as

$$R_N^{\mathcal{O}} = \frac{C_3^{\mathcal{O}}(\vec{p}, \vec{p}', \tau, T)}{\sqrt{C_2(\vec{p}, T) C_2(\vec{p}', T)}}, \tag{2.46}$$

$$R_S = \sqrt{\frac{C_2(\vec{p}, T-\tau) C_2(\vec{p}', \tau)}{C_2(\vec{p}', T-\tau) C_2(\vec{p}, \tau)}}, \tag{2.47}$$

and compute their product

$$\begin{aligned} R^{\mathcal{O}}(\vec{p}, \vec{p}', \tau, T) = R_N^{\mathcal{O}} R_S = & M^{\mathcal{O}}(\vec{p}, \vec{p}') + O(e^{-\Delta E_{10}(\vec{p})\tau}) \\ & + O(e^{-\Delta E_{10}(\vec{p}')(T-\tau)}) + O(e^{-\Delta E_{min} T}), \end{aligned} \tag{2.48}$$

as a function of $\tau \in [0, T]$ with fixed T. Above,

$$M^{\mathcal{O}}(\vec{p}, \vec{p}') = \frac{\sum_{\lambda, \lambda'} \bar{u}(\vec{p}, \lambda) \Gamma_{\text{pol}} u(\vec{p}', \lambda') \langle p', \lambda' | \mathcal{O} | p, \lambda \rangle}{4 \sqrt{E(\vec{p}) E(\vec{p}') (E(\vec{p}) + m_N)(E(\vec{p}') + m_N)}}, \tag{2.49}$$

and $\Delta E_{\text{min}} = \min\{\Delta E_{10}(\vec{p}), \Delta E_{10}(\vec{p}')\}$.

The ratio in Eq. (2.48) gives an estimate of the nucleon matrix element $\langle p', \lambda' | \mathcal{O} | p, \lambda \rangle$ and produces at large T a plateau with "tails" at both ends caused by excited states. In practice, for each fixed T, we average over the central two or three points near $\tau = T/2$, which allows for matrix elements to be computed with errors that decay asymptotically as $e^{-\Delta E_{\text{min}} T/2}$.

2.4.2 Summation method

Improved asymptotic behavior of excited-state contributions can be achieved by using the *summation method* [36, 32] which requires performing the calculations with multiple source-sink separations. Taking the sums of ratios for each T yields

$$S^{\mathcal{O}}(\vec{p},\vec{p}',T) \equiv \sum_{\tau=\tau_0}^{T-\tau_0} R^{\mathcal{O}}(\vec{p},\vec{p}',\tau,T) = c + TM^{\mathcal{O}}(\vec{p},\vec{p}') + O(Te^{-\Delta E_{\min}T}), \tag{2.50}$$

where we choose $\tau_0 = 1$ and c is an unknown constant. The matrix element can then be extracted from the slope of a linear fit to $S^{\mathcal{O}}(\vec{p},\vec{p}',T)$ at several values of T. The leading excited-state contaminations decay now as $Te^{-\Delta E_{min}T}$.

2.5 Nucleon form factors and radii

2.5.1 Extraction of nucleon form factors

The matrix elements of a bilinear current $\bar{q}\Gamma q$ that we compute in Sec. 2.4 can be parametrized using a linear combination of form factors

$$\langle \vec{p}',\lambda'|\mathcal{O}^{\mu}|\vec{p},\lambda\rangle = \bar{u}(\vec{p}',\lambda')\mathcal{F}^{\mu}(\vec{p},\vec{p}')u(\vec{p},\lambda). \tag{2.51}$$

For the case of the vector current, $\mathcal{O}^{\mu} = \bar{q}\gamma^{\mu}q$ and $\mathcal{F}^{\mu}(\vec{p},\vec{p}')$ can be written in terms of the Dirac and Pauli form factors, $F_1(Q^2)$ and $F_2(Q^2)$, in Minkowski space as

$$\mathcal{F}^{\mu}(\vec{p},\vec{p}') = \gamma^{\mu}F_1(Q^2) + \frac{i\sigma^{\mu\nu}(p'-p)_{\nu}}{2m_N}F_2(Q^2). \tag{2.52}$$

The form factors depend only on the momentum transfer Q^2 which is defined as

$$Q^2 = -(p'-p)^2. \tag{2.53}$$

At fixed Q^2, we find usually different matrix elements with different operator components, $\mathcal{O}^{\mu}$, and different source and sink momenta, $\vec{p},\vec{p}'$. For demonstrating the

extraction of the form factors, we take as an example the extraction of $F_1(Q^2)$ and $F_2(Q^2)$ which are best suited.

At each fixed Q^2 and for each combination of $\vec{p}$, $\vec{p}'$, and $\mathcal{O}^\mu$, we construct a system of equations parameterizing the corresponding set of matrix elements. For that we need to:

- Construct a matrix, A, containing the coefficients of F_1 and F_2 after transforming Eq. (2.52) to Euclidean space and substitute it into Eq. (2.49).

- Evaluate the matrix elements using Eq. (2.48) with neglecting the contributions from excited states.

After performing the above two steps, we obtain an overdetermined system of linear equations which has the form

$$\sum_j A_{ij} F_j = R_i \quad i = 1, 2, \ldots, \tag{2.54}$$

where i is a composite index specifying the current component and the source and sink momenta of a given matrix element for a fixed Q^2. The solution of this overdetermined system of equations can be obtained from a linear fit, which minimizes

$$\sum_{ij} (A_{ik} F_k - R_i) C_{ij}^{-1} (A_{jl} F_l - R_j), \tag{2.55}$$

where C is the covariance matrix of R

$$C_{ij} = \frac{1}{N-1} \left(\langle\langle R_i R_j \rangle\rangle - \langle\langle R_i \rangle\rangle \langle\langle R_j \rangle\rangle \right), \tag{2.56}$$

where the double brackets denotes the ensemble average. For improving the condition number of the covariance matrix, which may be ill conditioned, we use a blocking procedure following Ref. [116] where equivalent matrix elements under spatial symmetries such as rotation and reflection symmetries are combined into different classes.

2.5.2 Extraction of nucleon radii using z expansion

As mentioned in Sec. 1.2, the charge and axial radii can be extracted from the slopes of the electric and axial form factors at $Q^2 = 0$, respectively. For that we need to fit the Q^2-dependence of each form factor. In order to avoid the model dependence included in the commonly used fit ansatzes, such as a dipole formula

$$G(Q^2) = \frac{G(0)}{(1 + Q^2/M)^2}, \tag{2.57}$$

where G denotes the form factor and M is the dipole mass, we use the model-independent z expansion [21, 22, 77, 51], where each form factor can be described by a convergent Taylor series in z

$$G(Q^2) = \sum_{k}^{k_{\max}} a_k z^k, \qquad z = \frac{\sqrt{t_{\rm cut} + Q^2} - \sqrt{t_{\rm cut}}}{\sqrt{t_{\rm cut} + Q^2} + \sqrt{t_{\rm cut}}}, \tag{2.58}$$

which conformally maps the complex domain of analyticity in Q^2 to $|z| < 1$. In this study, we fix $a_0 = 1$ for fitting $G_E(Q^2)$ since $G_E(0) = 1$. We use the particle production threshold $t_{\rm cut} = (2m_\pi)^2$ for the vector case and $t_{\rm cut} = (3m_\pi)^2$ for the axial case. We apply z-expansion fits following the approach of Ref. [66]. The intercept and slope of the form factor at $Q^2 = 0$ can be obtained from the first two coefficients, a_0 and a_1. For the series to converge, we impose Gaussian priors on the remaining coefficients centered at zero with width equal to $w = 5\max\{|a_0|, |a_1|\}$ as was suggested in Ref. [51]. We truncate the series with $k_{\max} = 5$ after verifying that using a larger $k_{\max}$ produces identical fit results in our probed range of Q^2.

Furthermore, considering the generalized Goldberger-Treiman relation in the limit of vanishing momentum transfer and pion mass, it was found that the isovector G_P form factor has an isolated pole at the pion mass below the particle production threshold [109]

$$G_P(Q^2) = \frac{4m}{Q^2 + m_\pi^2} G_A(Q^2). \tag{2.59}$$

We thus remove this pole before fitting and perform the z-expansion fit to $(Q^2 + m_\pi^2)G_P(Q^2)$.

We perform correlated fits by minimizing

$$\chi^2_{\rm aug} = \sum_{i,j} \left(G(Q_i^2) - \sum_k a_k z(Q_i^2)^k \right) \Xi_{ij} \left(G(Q_j^2) - \sum_{k'} a_{k'} z(Q_j^2)^{k'} \right) + \sum_{k>1} \frac{a_k^2}{w^2}, \quad (2.60)$$

with respect to $\{a_k\}$, where Ξ is an estimator of the inverse covariance matrix and the last term augments the chi-squared with the Gaussian priors.

2.6 Renormalization in lattice QCD

The space-time lattice serves as a regulator for lattice QCD gauge theory with a fixed ultra-violet momentum cut-off determined by the inverse lattice spacing $\Lambda_{\rm lat} = a^{-1}$. The matrix elements we measure on the lattice are bare quantities that need to be renormalized in order to make comparisons to experimental values. The renormalization process includes removing the ultra-violet divergence in lattice observables followed by converting to an appropriate renormalization scheme such as the $\overline{\rm MS}$ scheme at the scale $\mu^2 = (2{\rm GeV})^2$.

Lattice perturbation theory [33] is a straightforward approach for performing the renormalization. When choosing the scale μ on the lattice, the following requirements need to be satisfied:

- $\mu \gg \Lambda_{\rm QCD}$ to make sure we are in the perturbative regime.
- $\mu \ll a^{-1}$ for having small discretization errors.
- $L^{-1} \ll m_\pi$ for the nucleon to fit into the physical volume of the lattice.

Combining the above requirements, we obtain

$$L^{-1} \ll m_\pi, \quad \Lambda_{\rm QCD} \ll \mu \ll a^{-1}. \quad (2.61)$$

The main problem faced when performing the renormalization on the lattice is the

large scale differences in Eq. (2.61). Having not sufficiently large volume for the lattice would result in not large enough value of μ which is one of the reasons why the lattice perturbative approach may not be reliable. Moreover, this procedure is known to be poorly convergent and calculation of more than one loop is difficult to perform. Therefore, nonperturpative methods have been developed and applied. The two commonly used methods are the Rome-Southampton method [96] and the Schrödinger functional [80]. The Rome-Southampton approach, also known as RI-MOM (RI for "Regularization Independent") is a momentum subtraction scheme which mimics the procedure used in continuum perturbation theory. In this approach, the renormalization condition is imposed on the forward vertex function of the operator with external off-shell quark states with equal incoming and outgoing momenta and in some fixed gauge, usually the Landau gauge. The renormalization condition is that the computed Green's functions coincide with their tree-level values. This approach has the problem that finding a window in the scale μ that satisfies Eq. (2.61) is not always possible, this is called the *window problem*. Given that the scale μ is in the perturbative regime, the matching to $\overline{\text{MS}}$ can then be performed using continuum perturbation theory. The Rome-Southampton approach is straightforward to implement on the lattice and has the advantage that it can be performed on the same gauge configurations produced for studying the nucleon physics. The scheme used in the Schrödinger functional approach is a finite volume one where the finite lattice size is used to set the renormalization scale, i.e., $\mu = L^{-1}$. The renormalization problem is then recursively solved using step scaling functions which make going from very high to very low scales possible. This procedure has the advantage of bridging the large scale differences found in Eq. (2.61).

In this work, we perform the nonperturbative renormalization by following the Rome-Southampton approach in the RI-MOM scheme. We use two of its variants, the RI'-MOM and RI-SMOM schemes. We briefly describe those schemes in the rest of this section.

2.6.1 Rome-Southampton method

For calculating the renormalization constants in this study, we follow the Rome-Southampton approach, or RI-MOM. In RI-MOM, one studies expectation values, $\langle p|\mathcal{O}|p\rangle$, at zero momentum transfer of the bilinear quark operators between quark fields at specific momentum value $p^2 = \mu^2$ and matches them to the corresponding tree-level matrix element

$$Z_{\mathcal{O}}\langle p|\mathcal{O}|p\rangle\Big|_{p^2=\mu^2} = \langle p|\mathcal{O}|p\rangle_0\Big|_{p^2=\mu^2}. \tag{2.62}$$

The renormalization constant $Z_{\mathcal{O}}$ is the proportionality factor between the interacting and the free case. Since Eq. (2.62) is gauge variant, we have to work in fixed gauge which in our case is the Landau gauge.

In Landau gauge, we compute quark propagators

$$S(p) = \frac{1}{V}\sum_{x,y} e^{-ip(x-y)}\langle\psi(x)\bar{\psi}(y)\rangle, \tag{2.63}$$

Green's functions,

$$G_{\mathcal{O}}(p,p') = \frac{1}{V}\sum_{x,y,z} e^{-ip'.(x-y)-ip.(y-z)}\langle\psi(x)\mathcal{O}(y)\bar{\psi}(z)\rangle, \tag{2.64}$$

and amputated Green's functions,

$$\Lambda_{\mathcal{O}}(p,p') = S(p')^{-1}G_{\mathcal{O}}(p,p')S(p)^{-1}. \tag{2.65}$$

We use the following conventions for the renormalization factors

$$\mathcal{O}^R = Z_{\mathcal{O}}\mathcal{O}, \quad \psi^R = \sqrt{Z_\psi}\psi. \tag{2.66}$$

The renormalized quantities can then be defined as

$$S_R(p) = Z_\psi S(p), \quad \Lambda^R_{\mathcal{O}}(p,p') = Z_\psi^{-1}Z_{\mathcal{O}}\Lambda_{\mathcal{O}}(p,p'). \tag{2.67}$$

RI-MOM, RI′-MOM, and RI-SMOM

In our study, we are mainly interested in computing the renormalization factors of the scalar, tensor, vector, and axial vector bilinears. We study the renormalization of those observables in two variants of the RI-MOM scheme, namely RI′-MOM, and RI-SMOM schemes. In RI-MOM and RI′-MOM schemes, we have $p' = p$ and the scale is defined as $\mu^2 = p^2$. The RI-SMOM (SMOM stands for *symmetric* momentum subtraction scheme) eases the window problem found in RI-MOM scheme and allows $p' \neq p$ where the scale is defined as $\mu^2 = q^2 = (p'-p)^2 = p^2 = p'^2$. The renormalization conditions of the vector and axial vector bilinears can be derived by demanding that their Ward identities are satisfied as we will see below. In the following, we show how the renormalization conditions are defined for the different observables and in the different schemes.

Vector bilinear: The vector current is defined as $V_\mu = \bar{\psi}\gamma_\mu\psi$. The vector Ward identity can be written as

$$q_\mu \Lambda^R_{V_\mu}(p+q,p) = -i\left[S_R^{-1}(p+q) - S_R^{-1}(p)\right]. \tag{2.68}$$

Demanding the satisfaction of this Ward identity, the renormalization conditions of the quark propagator and the vector current can be then derived by applying $\partial/\partial q_\nu$ at $q = 0$ and tracing with γ_ν, on both sides of Eq. (2.68). At $\mu^2 = p^2$ and after equating both sides to their tree-level values, we obtain the following RI-MOM conditions [96]

$$\lim_{m\to 0} -\frac{i}{48}\,\mathrm{Tr}\left[\gamma_\mu \frac{\partial S_R^{-1}(p)}{\partial p_\mu}\right] = 1, \tag{2.69}$$

$$\lim_{m\to 0} \frac{1}{48}\,\mathrm{Tr}\left[\Lambda^R_{V_\mu}(p,p)\gamma_\mu\right] = 1. \tag{2.70}$$

On a lattice with finite volume, the derivative in Eq. (2.69) can be difficult to evaluate. This motivates the use of an alternative condition for the quark field renormalization [96]

$$\lim_{m\to 0} \frac{-i}{12p^2}\,\mathrm{Tr}\left[S_R^{-1}(p)\not{p}\right] = 1. \tag{2.71}$$

The resulting renormalization factor is called Z'_ψ. In Landau gauge and one loop perturbation theory, $Z'_\psi = Z_\psi$. The combination of Z'_ψ with RI-MOM conditions for $Z_\mathcal{O}$ is called RI′-MOM. With the renormalization condition in Eq. (2.70), the Ward identity is not exact and it holds only up to artifacts. For enforcing the Ward identity, we follow the solution proposed in Ref. [29] where continuum symmetries are used to decompose the inverse quark propagator and amputated vertex function as follows

$$S^{-1}(p) = i\not{p}\Sigma_1(p^2) + \Sigma_2(p^2), \tag{2.72}$$

$$\Lambda_{V_\mu}(p,p) = \gamma_\mu g_1(p^2) + ip_\mu g_2(p^2) + p_\mu \not{p} g_3(p^2) + i[\gamma_\mu, \not{p}] g_4(p^2), \tag{2.73}$$

where both S^{-1} and Λ_{V_μ} are proportional to the identity in colour space. Applying the condition in Eq. (2.71) to Eq. (2.72) leads to $\Sigma_1^R(p^2) = 1$. Next, we take the derivative of Eq. (2.68) with respect to q_ν at $q = 0$ and match the terms to find, among other relations, $g_1^R(p^2) = \Sigma_1^R(p^2) = 1$. This suggests imposing the following renormalization condition on $g_1(p^2)$

$$\lim_{m\to 0} g_1^R(p^2) = \lim_{m\to 0} \frac{1}{36} \mathrm{Tr}\left[\Lambda_{V_\mu}^R(p,p)\left(\gamma_\mu - \frac{p_\mu \not{p}}{p^2}\right)\right] = 1. \tag{2.74}$$

To summarize, we use the following conditions to renormalize the quark field and vector current in RI′-MOM

$$\begin{aligned} \lim_{m\to 0} \frac{-i}{12p^2} \mathrm{Tr}\left[S_R^{-1}(p)\not{p}\right] &= 1, \\ \lim_{m\to 0} \frac{1}{36} \mathrm{Tr}\left[\Lambda_{V_\mu}^R(p,p)\left(\gamma_\mu - \frac{p_\mu \not{p}}{p^2}\right)\right] &= 1. \end{aligned} \tag{2.75}$$

In RI-SMOM scheme, the quark-field renormalization is the same as RI′-MOM, whereas we have a different projector for the vector current

$$\lim_{m\to 0} \frac{1}{12q^2} \mathrm{Tr}\left[q_\mu \Lambda_{V_\mu}^R(p,p')\not{q}\right] = 1. \tag{2.76}$$

Axial bilinear: The operator of the axial current is $A_\mu = \bar{\psi}\gamma_\mu\gamma_5\psi$. We consider the axial Ward identity which implies [30]

$$q_\mu \Lambda^R_{A_m u}(p+q,p) = -i\left[S_R^{-1}(p+q)\gamma_5 - \gamma_5 S_R^{-1}(p)\right] + i2m\Lambda^R_P(p+q,p). \tag{2.77}$$

As for the vector current, we find the following renormalization condition in RI′-MOM scheme

$$\lim_{m\to 0}\frac{1}{36}\,\mathrm{Tr}\left[\Lambda^R_{A_\mu}(p,p)\gamma_5\left(\gamma_\mu - \frac{p_\mu \not{p}}{p^2}\right)\right] = 1. \tag{2.78}$$

In RI-SMOM scheme, the condition is

$$\lim_{m\to 0}\frac{1}{12q^2}\,\mathrm{Tr}\left[q_\mu\Lambda^R_{A_\mu}(p,p')\gamma_5\not{q}\right] = 1. \tag{2.79}$$

Scalar bilinear: The scalar bilinear operator is defined as $S = \bar{\psi}\psi$. In RI′-MOM, the condition is

$$\lim_{m\to 0}\frac{1}{12}\,\mathrm{Tr}\left[\Lambda^R_S(p,p)\right] = 1, \tag{2.80}$$

and for RI-SMOM, it has the same form

$$\lim_{m\to 0}\frac{1}{12}\,\mathrm{Tr}\left[\Lambda^R_S(p',p)\right] = 1. \tag{2.81}$$

Tensor bilinear: We write the tensor operator as $T_{\mu\nu} = \bar{\psi}\frac{1}{2}[\gamma_\mu,\gamma_\nu]\psi$. In RI′-MOM, Gracey [59] starts from the decomposition

$$\Lambda_{T_{\mu\nu}}(p,p) = \Sigma_T^{(1)}(p^2)\tfrac{1}{2}[\gamma_\mu,\gamma_\nu] + \Sigma_T^{(2)}(p^2)\frac{\not{p}}{p^2}\left(\gamma_\mu p_\nu - \gamma_\nu p_\mu\right), \tag{2.82}$$

and then imposes the condition $\Sigma_T^{(1),R}(p^2) = 1$. Note that chiral symmetry breaking allows more terms to appear, but they will not contribute to any relevant trace. As Gracey notes, this term can be isolated via

$$\Sigma_T^{(1)}(p^2) = \frac{-1}{72}\,\mathrm{Tr}\left[\Lambda_{T_{\mu\nu}}(p,p)\left(\tfrac{1}{2}[\gamma_\mu,\gamma_\nu] + \frac{\not{p}}{p^2}\left(\gamma_\mu p_\nu - \gamma_\nu p_\mu\right)\right)\right]. \tag{2.83}$$

This can be rewritten to obtain the renormalization condition in a simple form

$$\lim_{m\to 0} \frac{1}{72} \mathrm{Tr}\left[\Lambda^R_{T_{\mu\nu}}(p,p) \tfrac{1}{2}[\gamma_\beta,\gamma_\alpha] P_{\mu\alpha} P_{\nu\beta}\right] = 1. \tag{2.84}$$

For RI-SMOM, the condition is

$$\lim_{m\to 0} \frac{1}{144} \mathrm{Tr}\left[\Lambda^R_{T_{\mu\nu}}(p',p) \tfrac{1}{2}[\gamma_\nu,\gamma_\mu]\right] = 1. \tag{2.85}$$

In our calculations, we avoid directly determining the quark-field renormalization. Instead, we impose the above renormalization conditions on the vector current, which gives Z_ψ/Z_V, and independently obtain Z_V from three-point functions of pseudoscalar mesons. Our estimate for Z_ψ in RI′-MOM is then obtained using

$$(Z_\psi)_{\text{RI′-MOM}} = \frac{Z_V}{36} \mathrm{Tr}\left[\Lambda_{V_\mu}(p,p)\left(\gamma_\mu - \frac{p_\mu \not{p}}{p^2}\right)\right]. \tag{2.86}$$

In RI-SMOM, we estimate Z_ψ in the same way using Eq. (2.76).

To convert from RI′-MOM and RI-SMOM schemes to $\overline{\text{MS}}$ scheme, the continuum perturbation theory should be used. For the axial charge, the renormalization conditions in RI′-MOM and RI-SMOM are related by chiral rotations to the corresponding conditions on the vector current. This implies that in the chiral limit, the renormalized axial current will satisfy the axial Ward identity, and therefore no matching to $\overline{\text{MS}}$ is needed. For the scalar bilinear operator, the conversion factor between RI′-MOM and $\overline{\text{MS}}$ is known to three loops [43, 59], and between RI-SMOM and $\overline{\text{MS}}$ it is known to two loops [61]. The anomalous dimension is obtained from the quark mass anomalous dimension via $\gamma_S = -\gamma_m$; we use in this work the four-loop $\overline{\text{MS}}$ result [42, 119]. For the tensor bilinear operator, the matching from RI′-MOM to $\overline{\text{MS}}$ is known to three loops [59], and for RI-SMOM it is known to two loops [61]. We use the four-loop $\overline{\text{MS}}$ anomalous dimension [12]. After converting to $\overline{\text{MS}}$ scheme, one needs to evolve the renormalization factors to 2 GeV scale which is done by integrating the renormalization group equations as we will see later in Sec. 5.2.3. After perturbatively matching the RI′-MOM or RI-SMOM data to $\overline{\text{MS}}$ and evolving to the scale 2 GeV, we

perform fits including terms polynomial in μ^2 to remove any residual nonperturbative artifacts. We also make use of the two different schemes to estimate unaccounted-for systematic uncertainties.

Chapter 3

Nucleon axial, scalar, and tensor charges

In this chapter, we present a lattice QCD calculation of the isovector axial, scalar, and tensor charges of the nucleon using two ensembles at the physical pion mass with different lattice spacings. We also investigate the contamination of excited states for the different charges by using multiple source-sink separations and employing multiple analysis methods for extracting the charges.

This chapter is based on our work published in Ref. [75] and is organized as follows. In Sec. 3.1, we describe the parameters of the gauge ensembles analyzed, the lattice methodology, and the fits to the two-point functions used to extract the energy gaps to the first-excited state on each ensemble. We discuss different analysis methods for estimating the three bare charges and eliminating the excited-state contaminations and present a procedure for combining the multiple results in Sec. 3.2. The procedure we follow for determining the renormalization factors for the different observables using both RI′-MOM and RI-SMOM schemes is described in Sec. 3.3. In Sec. 3.4, we give the final estimates of the renormalized charges and discuss the continuum and infinite-volume effects. Finally, we give our conclusions in Sec. 3.5.

3.1 Lattice setup

3.1.1 Correlation functions

For determining the isovector nucleon charges, we need to compute the nucleon two- and three-point correlators at $\vec{p}' = \vec{p} = 0$. For simplicity, we drop the momenta from Eq. (2.17) and Eq. (2.23) and use the isovector operator $\mathcal{O}_X = \bar{q}\Gamma_X \frac{\tau^3}{2} q$, where the Dirac matrix Γ_X is $1, \gamma_\mu\gamma_5$ and $\sigma_{\mu\nu}$ for the scalar (S), the axial (A) and the tensor (T) operators, respectively. Thus, we compute

$$C_2(t) = \sum_{\vec{x}} (\Gamma_{\text{pol}})_{\beta\alpha} \left\langle \chi_\alpha(\vec{x}, t)\bar{\chi}_\beta(0)\right\rangle , \tag{3.1}$$

$$C_3^X(\tau, T) = \sum_{\vec{x},\vec{y}} (\Gamma_{\text{pol}})_{\beta\alpha} \left\langle \chi_\alpha(\vec{x}, T)\mathcal{O}_X(\vec{y}, \tau)\bar{\chi}_\beta(0)\right\rangle , \tag{3.2}$$

where T is the source-sink separation and τ is the current insertion timeslice. q is the quark doublet $q = (u, d)^T$, and we use the positive parity projected interpolating operator defined in Eq. (2.4) with smeared quark fields. We use Wuppertal smearing (see Sec. 2.3) with the parameters defined in Tab. 2.1 for the our two ensembles.

In order to compute C_3^X, we use sequential propagators through the sink, see Sec. 2.2.2. As we explained earlier, the three-point correlators have contributions from both connected- and disconnected-quark contractions, but in this part of our study we need only to compute the connected part since for the isovector flavor combination the disconnected contributions cancel out.

3.1.2 Simulation details

We perform our lattice QCD calculations using a tree-level Symanzik-improved gauge action and $2 + 1$ flavors of tree-level improved Wilson-clover quarks, which couple to the gauge links via two levels of HEX smearing [49]. We use two ensembles at the physical pion mass: one with size 48^4 and lattice spacing $a \approx 0.116$ fm which we call coarse, and another with 64^4 and $a \approx 0.093$ fm which we call fine. Both vol-

umes satisfy $m_\pi L \approx 4$. On the coarse ensemble, we perform measurements on 212 gauge configurations using source-sink separations $T/a \in \{3, 4, 5, 6, 7, 8, 10, 12\}$ ranging roughly from 0.4 to 1.4 fm. In addition, we make use of all-mode-averaging (AMA) [27, 112] to reduce the computational cost through inexpensive approximate quark propagators. For $T/a \in \{3, 4, 5\}$, we use approximate samples from 96 source positions per gauge configurations and high-precision samples from one source position for bias correction, and for $T/a \in \{6, 7, 8, 10, 12\}$ we use double those numbers. On the fine ensemble, we perform the calculations on 442 gauge configurations using source-sink separations $T/a \in \{10, 13, 16\}$ ranging roughly from 0.9 to 1.5 fm. AMA is applied with 64 sources with approximate propagators and one source for bias correction per gauge configuration. Tables. 3.1 and 3.2 summarize the parameters and the number of measurements performed on each of the ensembles.

Ensemble ID	Size	β	am_{ud}	am_s	a [fm]	am_π	m_π [MeV]	$m_\pi L$
coarse	48^4	3.31	-0.09933	-0.04	0.1163(4)	0.0807(12)	137(2)	3.9
fine	64^4	3.5	-0.05294	-0.006	0.0926(6)	0.0626(3)	133(1)	4.0

Table 3.1: Parameters of the ensembles used in this work. The lattice spacing is taken from Ref. [49], where it is set using the mass of the Ω baryon at the physical point.

Ensemble ID	N_{conf}	T/a	$N_{\text{meas}}^{\text{AMA}}$	$N_{\text{meas}}^{\text{HP}}$
coarse	212	$\{3, 4, 5\}$	40704	424
		$\{6, 7, 8, 10, 12\}$	81408	848
fine	442	$\{10, 13, 16\}$	56576	884

Table 3.2: Parameters of the measurements used in this work. N_{conf} refers to the number of gauge configurations analyzed and $N_{\text{meas}}^{\text{AMA}} = 2 \times N_{\text{conf}} \times N_{\text{src}}^{\text{AMA}}$ is the number of measurements performed using AMA method with $N_{\text{src}}^{\text{AMA}}$ being the number of source positions used on each gauge configuration. The factor of 2 in N_{meas} accounts for the use of forward- and backward-propagating states. Finally, $N_{\text{meas}}^{\text{HP}}$ refers to the number of measurements made with high-precision.

Ensemble	aE_0	aE_1	a_1/a_0	χ^2/dof
coarse	0.5550(56)	1.08(11)	0.97(20)	0.45
fine	0.4279(36)	0.737(70)	0.89(12)	0.33

Table 3.3: Estimated parameters of two-state fit to two-point correlation functions.

3.1.3 Fitting two-point functions

On each ensemble, we perform two-state fits to the two-point correlation functions at zero momentum

$$C_2(t) = a_0 e^{-E_0 t} + a_1 e^{-E_1 t}, \tag{3.3}$$

where a_i and E_i denote the amplitudes and the energies of the ground- and first-excited states, respectively. For comparison, we also perform one-state fits with $C_2(t) = a_0 e^{-E_0 t}$ only.

The blue and red points in Fig. 3-1 show the dependence of aE_0 and $a\Delta E_1 = a(E_1 - E_0)$ on the start time slice $t_{\rm min}/a$ for the coarse (left) and fine (right) ensembles. The values for aE_0 were obtained using both the one- and two-state fits. The shaded blue and red bands indicate our preferred estimates of aE_0 and $a\Delta E_1$, respectively. Those correspond to the two-state fits with $t_{\rm min}/a = 4$ for the coarse ensemble and $t_{\rm min}/a = 5$ for the fine ensemble. The quality of the resulting fits are shown in Fig. 3-2 by plotting the two-point function divided by its fitted ground-state contribution

$$\frac{C_2(t)}{a_0 \exp(-E_0 t)}. \tag{3.4}$$

Table 3.3 gives a summary of the estimated fit parameters on both the coarse and fine ensembles.

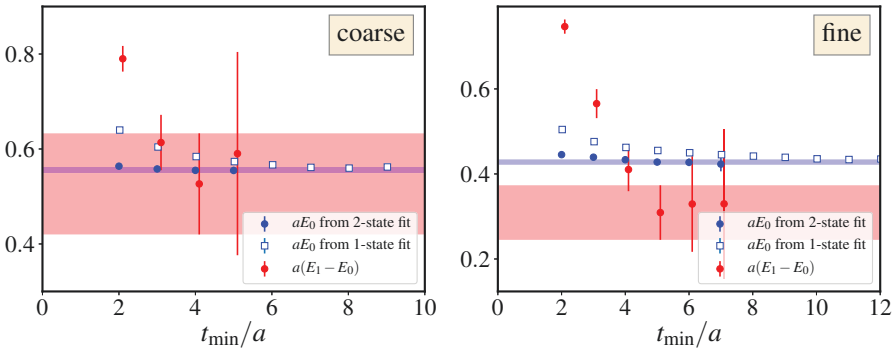

Figure 3-1: The dependence of E_0 and E_1 from one- and two-state fits to two-point functions on t_{min}. The red and blue shaded bands correspond to our preferred estimates of the ground-state mass and energy gap, respectively.

3.2 Estimation of bare charges

Taking the ratio of the three- and two-point correlators in Eq. (3.1) and Eq. (3.2) (see Sec. 2.4.1) yields the bare charges

$$R^X(\tau, T) \equiv \frac{C_3^X(\tau, T)}{C_2(T)} \xrightarrow{\text{large } \tau,(T-\tau)} g_X^{\text{bare}} + \sum_n \left[b_n \left(e^{-\Delta E_n (T-\tau)} + e^{-\Delta E_n \tau} \right) + b'_n e^{-\Delta E_n T} + \ldots \right], \quad (3.5)$$

where $\Delta E_n \equiv E_n - E_0$ is the energy gap between the nth excited state and ground state. Increasing T suppresses excited-state contamination, but it also increases the noise; the signal-to-noise ratio is expected to decay asymptotically as $e^{-(E-\frac{3}{2}m_\pi)T}$ [90].

Excited-state contamination is a source of significant systematic uncertainties in the calculation of nucleon structure observables. In the remainder of this section, we discuss the analysis methods we employ to study and suppress excited-state contributions to the axial, scalar, and tensor charges. We start with estimating the bare charges using the standard 'ratio method' in Sec. 3.2.1. In Sec. 3.2.2, we discuss the use of the summation method in addition to presenting a two-state fit model to the summations, which was inspired by the calculation in Ref. [41] that quotes

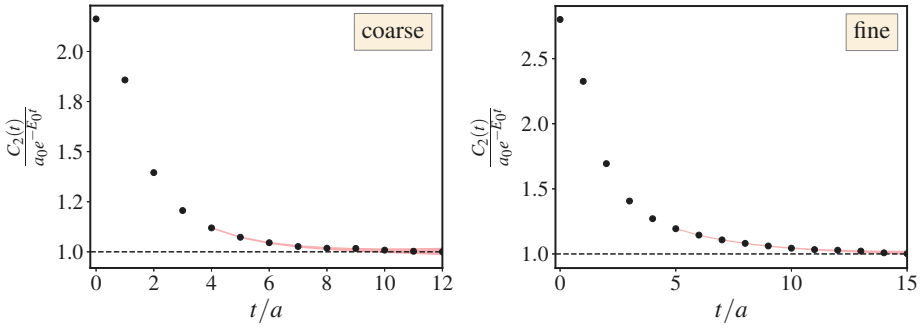

Figure 3-2: Plots of the two-point function divided by the ground-state contribution, for both the coarse (left) and the fine (right) ensembles.

a percent-level uncertainty for g_A. Furthermore, we employ a two-state fit to the ratios $R^X(\tau, T)$, which is presented in Sec. 3.2.3. Finally, in Sec. 3.2.4, we explain the procedure we follow to combine the estimates from the different fit strategies and extract final values for the bare charges.

3.2.1 Ratio method

The ratio method is a simple approach that allows for excited-state effects to be clearly seen. Figures 3-3 to 3-5 show our results for the isovector axial, scalar, and tensor charges on the coarse (top rows) and fine (bottom rows) ensembles. The first columns of those figures show the ratios yielding the different charges as functions of the insertion time τ/a shifted by half the source-sink separation, i.e., $(\tau - T/2)/a$. The different colors correspond to the ratios obtained using different source-sink separations. As explained in Sec. 2.4.1, when the time separations τ and $T - \tau$ are large, the ratios become time-independent. One observes increasing (for g_A^{bare} and g_S^{bare}) or decreasing (for g_T^{bare}) trends for the plateau values as the time separations are increased and clear curvatures indicating the significant contributions from excited states. We estimate the different charges by averaging the central two or three points near $\tau = T/2$. The blue circles in the second columns of Figs. 3-3 to 3-5 are the estimated charges from the plateaus plotted against $T/2$. We know that the

excited-state contributions to $R^X(\tau, T)$ decay as $e^{-\Delta E_1 T/2}$ which results eventually in a plateau when the source-sink separation is large enough. We observe on both the coarse and fine ensembles that the axial and scalar charges plateau as expected with increasing $T/2$, however, this does not happen in the case of the tensor charge, indicating that this method fails to reliably control excited states for g_T.

3.2.2 Summation method

For studying the excited-state contributions, we use in addition to the aforementioned ratio method, the summation method which is reviewed in Sec. 2.4.2. Here, we sum ratios at each source-sink separation T and the summed ratios are asymptotically linear in the source-sink separation

$$S^X(T) \equiv \sum_{\tau=\tau_0}^{T-\tau_0} R^X(\tau, T) = c_0 + T g_X^{\text{bare}} + O(Te^{-\Delta E_1 T}) + O(e^{-\Delta E_1 T}). \tag{3.6}$$

For performing the fits of the summation method on the coarse ensemble, we vary the fit range by fixing the maximum source-sink separation included in the fit to $T_{\text{max}}/a = 12$ and changing the minimal source-sink separation, T_{min}/a. The obtained results for the three charges on the coarse ensemble are displayed as red squares in the upper right panels of Figs. 3-3 to 3-5 which demonstrate the dependences of g_X^{bare} on T_{min}/a. Here, we see that the obtained g_A^{bare} shows a slight increase when increasing from the shortest T_{min} and g_T^{bare} shows a somewhat larger decrease, whereas g_S^{bare} is flat. We eventually reach a plateau in all cases. The fit quality is measured by computing the p-value and the open symbols refer to fits with p-value < 0.02. The red squares in the lower right panels of Figs. 3-3 to 3-5 show the results for the summation method on the fine ensemble including all three available source-sink separations, which leads to one summation point at $T_{\text{min}}/a = 10$.

The numerous source-sink separations used for calculations on the coarse ensemble allow us to perform the fit to the summations in Eq. (3.6) including contributions from the first-excited state. This leads to two additional fit parameters c_1 and c_2 where ΔE_1 is estimated from two-state fit to the two-point correlation function. The

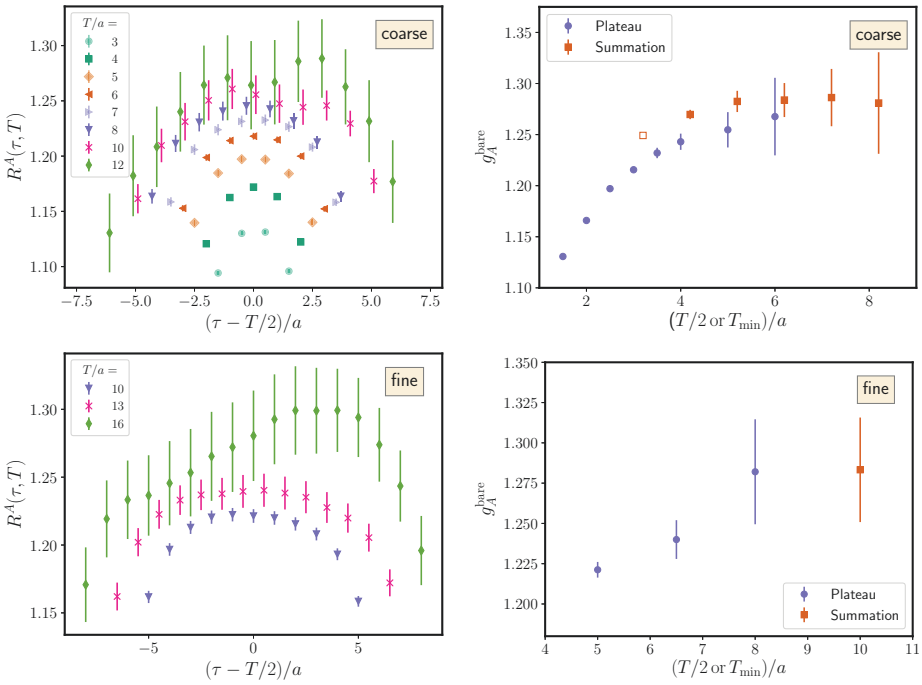

Figure 3-3: Results for the isovector axial charges on the coarse (top row) and fine (bottom row) ensembles using the ratio and summation methods. The first column shows the dependence of the ratios on the operator insertion time τ and the source-sink separation T. Different source-sink separations are displayed in different colors. The blue circles in the second column show the values of the charges estimated by averaging the two or three central points of $R^A(\tau, T)$ near $\tau = T/2$ and their dependences on $T/2$. The red squares in the second column show the resulting bare isovector axial charges using the summation method. Here, we show the dependences of the obtained axial charge on the minimal source-sink separations included in the fit T_{min}. The open symbol indicates a poor fit with p-value less than 0.02.

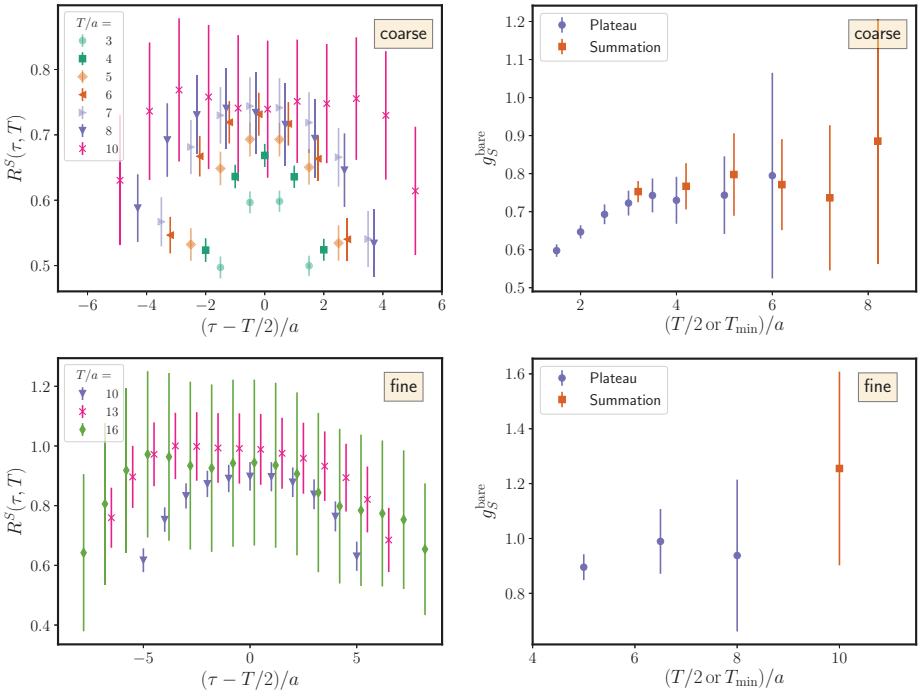

Figure 3-4: Results for the isovector scalar charge using the ratio and summation methods. See the caption of Fig. 3-3 for explanations.

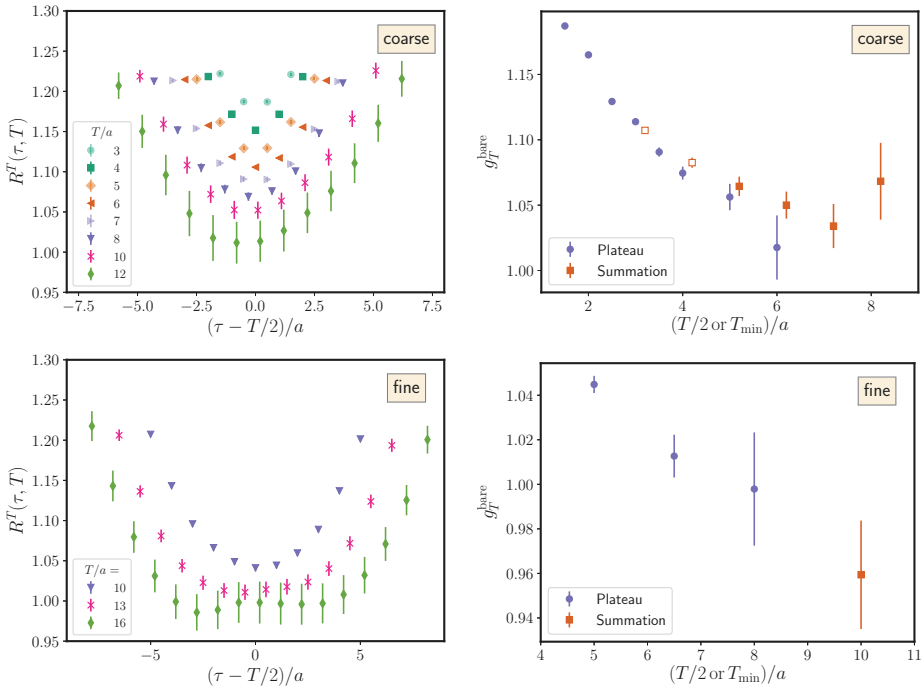

Figure 3-5: Results for the isovector tensor charge using the ratio and summation methods. See the caption of Fig. 3-3 for explanations.

fit function becomes

$$S^X(T) = c_0 + g_X^{\text{bare}} T + c_1 T e^{-\Delta E_1 T} + c_2 e^{-\Delta E_1 T}. \tag{3.7}$$

In Fig. 3-6, we show the results of such a fit for all three charges. As before, we fix $T_{\text{max}}/a = 12$ and vary T_{min}. The results in Fig. 3-6 show that the fits for the different charges are stable although with relatively large statistical errors. The endcaps of the error bars refer to the resulting statistical uncertainties when fixing ΔE_1 in Eq. (3.7) to its central value whereas the vertical lines of the error bars result from taking the uncertainties in ΔE_1 into consideration when evaluating the fit in Eq. (3.7). We see that fixing ΔE_1 to its central value has little to no effect on the final results.

3.2.3 Two-state fit of the ratio

In this section, we study including the contribution from a single excited state when fitting the ratio, $R^X(\tau, T)$. This is performed using the fit function

$$R^X(\tau, T) = g_X^{\text{bare}} + b_X \left(e^{-\Delta E_1 \tau} + e^{-\Delta E_1 (T-\tau)} \right) + b'_X e^{-\Delta E_1 T}. \tag{3.8}$$

Here, ΔE_1 is estimated from two-state fit to the two point function. We perform the stability analysis for this method by fitting to all points with $\tau \in [\tau_0, T - \tau_0]$ and varying τ_0.

The circles with the outer statistical uncertainties in the plots of Fig. 3-7 show the resulting unrenormalized isovector charges as we vary τ_0 for the coarse (left column) and fine (right column) ensembles. The fit range includes source-sink separations satisfying $T \geq 2\tau_0$; this means that for the coarse ensemble, as τ_0 is increased the shorter source-sink separations (which have the most precise data) will be excluded from the fit. We notice that for g_A^{bare}, there is no significant dependence on τ_0. The estimates for g_S^{bare} show a noisier signal on the fine ensemble. The signal for g_T^{bare} on the fine ensemble shows an upward trend in the central value for increased τ_0 while the statistical uncertainties are decreasing; this is normally not expected, whereas the

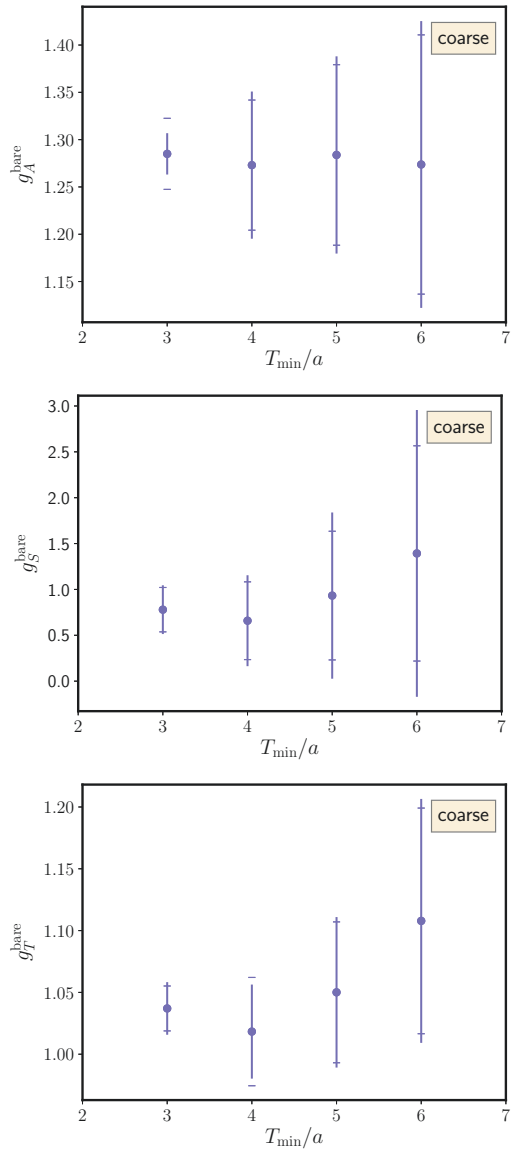

Figure 3-6: The obtained unrenormalized axial, scalar, and tensor charges on the coarse ensemble from fits to the summations $S^X(T)$ including contributions from a single excited state. The endcaps of the error bars refer to the resulting statistical uncertainties when fixing ΔE_1 in Eq. (3.7) to its central value, whereas the vertical lines of the error bars result from taking the uncertainties in ΔE_1 into consideration when evaluating the fit in Eq. (3.7).

signal on the coarse ensemble shows no to little dependence on τ_0. The inner error bars of Fig. 3-7 show the uncertainties when ΔE_1 is fixed to its central value. The difference between the inner and outer statistical uncertainties for the axial charge shows that the uncertainty on the energy gap makes a large contribution to the uncertainties of the final results, particularly when including small time separations in the fit. This may be because the small time separations are more sensitive to the model parameters used to remove excited-state contributions. This observation applies also to the tensor charge but less to the scalar charge.

3.2.4 Combining different analyses

We have so far applied four methods for analyzing the excited-state contributions to the different observables on each ensemble, namely

1. Ratio method
2. Summation method
3. Two-state fit to $R^X(\tau, T)$
4. Two-state fit to $S^X(T)$ (on the coarse ensemble)

For each method, we have plotted the estimated charges as functions of a Euclidean time separation $T/2$, T_{min}, or τ_0, which we will generically call δt. For each bare charge, we want to choose a preferred δt for each method and then combine the results from all methods to obtain a final result. In order to reduce the number of case-by-case decisions, we have devised a procedure that we will follow to accomplish this. Our procedure is designed to fulfill the following requirements ordered in decreasing importance:

- Fit ranges with poor fit quality are excluded, since that indicates the data are not compatible with the fit model and therefore the fit result is not trustworthy.
- Estimations should be taken from the asymptotic plateau regime, where there is no significant dependence on δt.

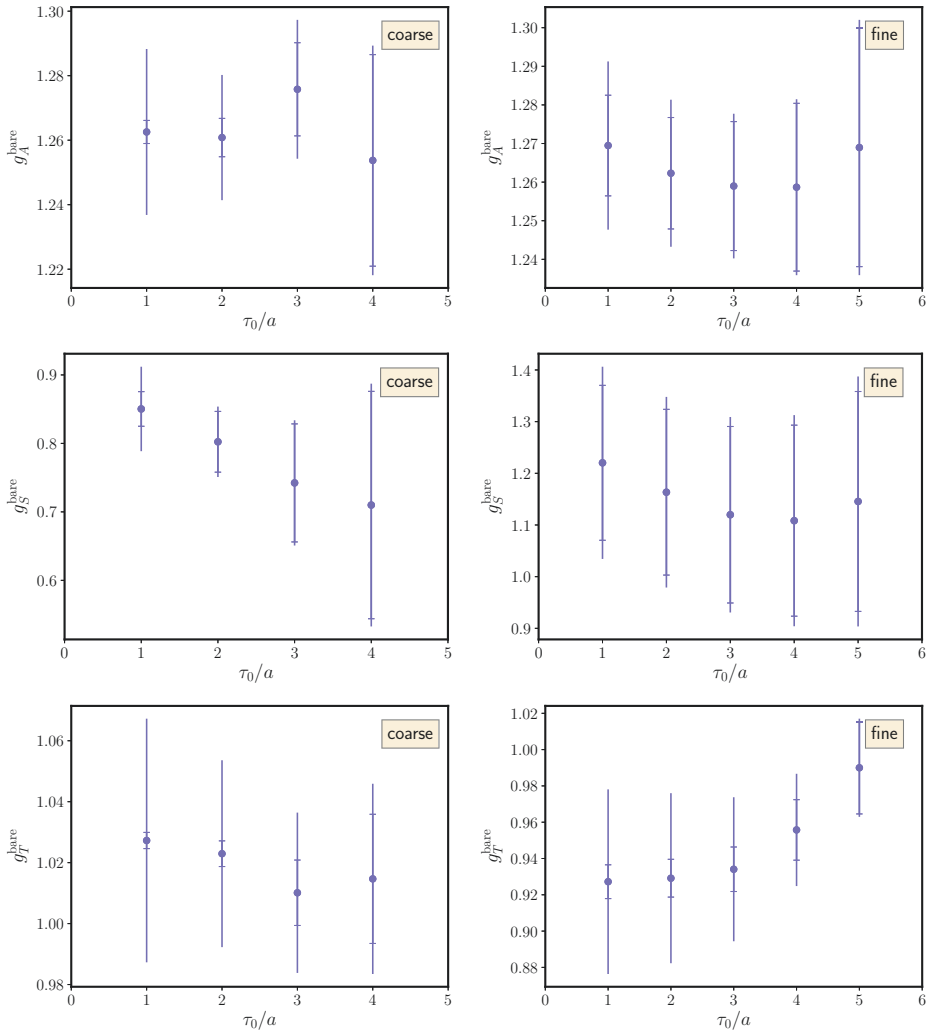

Figure 3-7: Estimates of the unrenormalized isovector axial, scalar, and tensor charges from the two-state fit to $R^X(\tau, T)$ as functions of τ_0 for the coarse and fine ensembles. The inner error bars (endcaps) refer to the resulting statistical uncertainties when fixing ΔE_1 in Eq. (3.8) to its central value whereas the outer error bars (vertical lines) result from taking the uncertainties in ΔE_1 into consideration when evaluating the fit in Eq. (3.8).

- Smaller statistical uncertainties are preferred.
- Larger time separations are preferred so that we reduce the residual excited-state contamination.

In the following, we outline the first part of the procedure which aims to find a preferred δt from each analysis method.

1. If data are obtained from fits (all methods except the ratio method), we start from the smallest δt, δt_{min}, and increase it until the fit quality is good. The criterion is for the fit to have a p-value greater than 0.02. We call the smallest δt that fulfills this criterion δt_0.

2. We fit the data starting from δt_0 with a constant and test if the p-value of that fit is greater than 0.05. We increase δt until this is the case. We name the smallest δt that fulfills this requirement δt_1.

3. In order to make sure that we are well inside a plateau region, we take $\delta t_2 = \delta t_1 + 0.2$ fm. Rounded to the nearest lattice spacing, this corresponds to the addition of $2a$ on each ensemble.

4. We find the data point with $\delta t \geq \delta t_2$ that has the smallest statistical uncertainty. We denote this point as δt_3.

5. Starting from the largest available δt, we decrease δt until we find a data point with uncertainty no more than 20% larger than the uncertainty at δt_3. We consider this data point to be the final estimation for the analysis method under consideration. We name the time separation at this point δt_f. The motivation here is that for points of similar statistical uncertainty, larger δt is preferred because of the reduced residual excited-state contamination.

On the fine ensemble, we do not have small values of δt for the ratio and summation methods. When $\delta t_1 = \delta t_{\text{min}}$, this suggests that the plateau could start earlier than our available data. In this case, we choose to take δt_2 determined on the coarse ensemble

	Coarse					Fine				
Method	δt_{min}	δt_0	δt_1	δt_f	g_A^{bare}	δt_{min}	δt_0	δt_1	δt_f	g_A^{bare}
Ratio	$1.5a$		$3.5a$	$6a$	1.268(38)	$5a$		$5a$	$8a$	1.282(33)
Summation	$3a$	$4a$	$4a$	$6a$	1.284(17)	$10a$	$10a$	$10a$	$10a$	1.283(32)
Two-state fit to $R^X(\tau, T)$	$1a$	$1a$	$1a$	$3a$	1.276(22)	$1a$	$1a$	$1a$	$4a$	1.259(23)
Two-state fit to $S^X(T)$	$3a$	$3a$	$3a$	$5a$	1.28(10)					

Table 3.4: The final estimates of the bare axial charge for each method on the coarse and fine ensembles.

	Coarse					Fine				
Method	δt_{min}	δt_0	δt_1	δt_f	g_S^{bare}	δt_{min}	δt_0	δt_1	δt_f	g_S^{bare}
Ratio	$1.5a$		$2a$	$4a$	0.730(62)	$5a$		$5a$	$5a$	0.895(47)
Summation	$3a$	$3a$	$3a$	$6a$	0.77(12)	$10a$	$10a$	$10a$	$10a$	1.25(35)
Two-state fit to $R^X(\tau, T)$	$1a$	$1a$	$1a$	$3a$	0.742(91)	$1a$	$1a$	$1a$	$4a$	1.11(20)
Two-state fit to $S^X(T)$	$3a$	$3a$	$3a$	$5a$	0.93(91)					

Table 3.5: The final estimates of the bare scalar charge for each method on the coarse and fine ensembles.

	Coarse					Fine				
Method	δt_{min}	δt_0	δt_1	δt_f	g_T^{bare}	δt_{min}	δt_0	δt_1	δt_f	g_T^{bare}
Ratio	$1.5a$		$5a$	-	-	$5a$		$6.5a$	-	-
Summation	$3a$	$5a$	$5a$	$7a$	1.034(17)	$10a$	$10a$	$10a$	$10a$	0.959(24)
Two-state fit to $R^X(\tau, T)$	$1a$	$1a$	$1a$	$4a$	1.015(31)	$1a$	$1a$	$1a$	$5a$	0.990(27)
Two-state fit to $S^X(T)$	$3a$	$3a$	$3a$	$5a$	1.050(61)					

Table 3.6: The final estimates of the bare tensor charge for each method on the coarse and fine ensembles.

for the same method and same charge, and use it (scaled to account for the different lattice spacings) as δt_2 on the fine ensemble.

The above procedure gives multiple estimates for each observable: at most one from each method. The obtained estimates of the axial, scalar, and tensor charges for both ensembles are listed in Tabs. 3.4, 3.5, and 3.6, respectively. In those tables, we also outline for each case the obtained δt_{min} which is the smallest available δt, δt_0 resulting from the first step in the above procedure and δt_1 from the second step. For cases where $\delta t_{\text{min}} = \delta t_1$, this indicates that there is no significant residual excited-state contamination. This is always the case for two-state fits, indicating that the data are compatible with the single-excited-state model. There are cases in the tables where we have no remaining data after the second or the third step of the above procedure to define a δt_f and therefore we leave those fields empty, as no reliable result could be obtained. We notice that we obtain similar δt_1 for the ratio and summation methods which indicates that it is appropriate to compare ratios at separation T with summation points at $T_{\text{min}} = T/2$. In this case (and it can be seen in Fig. 3-3– 3-5), the summation method provides more precise results than the ratios; this is in contrast to the usual comparison of ratio at separation T and summation at $T_{\text{min}} = T$, which finds that the summation method has larger uncertainties. The values for the axial, scalar, and tensor charges in the tables show consistency within error bars between the different methods. The statistical uncertainties differ between the different fit strategies; in particular we obtain relatively large error bars for the scalar charge on both ensembles.

For obtaining a final estimate of the charges, we combine the different analysis methods by performing a weighted average to determine the central value. The statistical uncertainty is determined using bootstrap resampling. We test the compatibility of the central value with the set of analysis methods using a correlated χ^2. If the reduced χ^2 is greater than one, then this indicates the different analysis methods are not in agreement, and the corresponding systematic uncertainty can be accounted for by scaling the statistical uncertainty by $\sqrt{\chi^2/\text{dof}}$. We list our final estimates of the charges on both ensembles in Tab. 3.7. In this table, the given uncertainties are

Ensemble	g_A^{bare}	g_S^{bare}	g_T^{bare}
Coarse	1.282(17)	0.740(74)	1.029(20)
Fine	1.271(24)	0.913(54)	0.972(23)

Table 3.7: Our final estimates of the charges on the coarse and fine ensembles.

obtained from bootstrap resampling and all the χ^2 values are acceptable. We obtain the largest $\chi^2/\text{dof} = 1.04$ for g_S^{bare} from the fine ensemble.

3.3 Nonperturbative renormalization

We follow the nonperturbative Rome-Southampton approach reviewed in Sec. 2.6, in both RI′-MOM and RI-SMOM schemes for determining the renormalization factors for isovector axial, scalar, and tensor bilinears. We then convert and evolve to the $\overline{\text{MS}}$ scheme at scale 2 GeV using perturbation theory.

3.3.1 Vector current

Following, e.g., Refs. [49, 66], we determine Z_V by computing the zero-momentum pion two-point function $C_2(t)$ and three-point function $C_3(t)$, where the latter has source-sink separation $T = L_t/2$ and an operator insertion of the time component of the local vector current at source-operator separation t. The charge of the interpolating operator gives the renormalization condition

$$Z_V \left[R(t_1) - R(t_2)\right] = 1, \tag{3.9}$$

for $0 < t_1 < T < t_2 < L_t$, where $R(t) = C_3(t)/C_2(T)$. We choose $t_2 = t_1 + T$; the difference results in a large cancellation of correlated statistical uncertainties, so that precise results can be obtained with relatively low statistics; see Fig. 3-8. Results on the coarse ensemble are much noisier than on the fine one, although the statistical errors are still below 1%. We take the unweighted average across the plateau, excluding the first and last three points. This yields $Z_V = 0.9094(36)$ on the coarse ensemble and $Z_V = 0.94378(10)$ on the fine one.

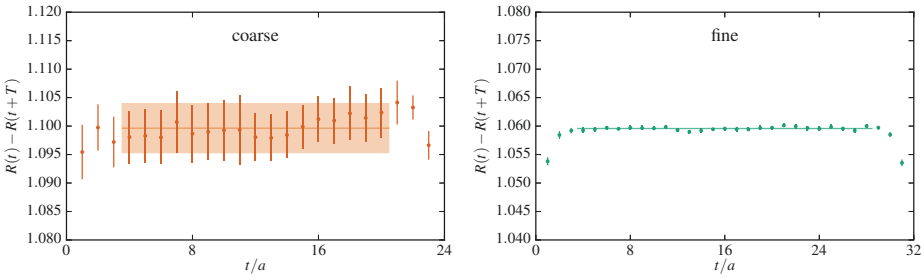

Figure 3-8: Determination of Z_V: coarse ensemble (left) and fine ensemble (right). This difference of ratios provides an estimate of Z_V^{-1}.

3.3.2 Axial, scalar, and tensor bilinears

We use partially twisted boundary conditions, namely periodic in time for the valence quarks rather than the antiperiodic condition used for sea quarks. The plane-wave sources are given momenta $p = \frac{2\pi}{L}(k, k, k, \pm k)$, $k = 2, 3, \ldots, \frac{L}{4a}$. By contracting them in different combinations, we get data for both RI′-MOM kinematics, $p' - p = 0$, and RI-SMOM kinematics, $p' - p = \frac{2\pi}{L}(0, 0, 0, \pm 2k)$. We used 54 gauge configurations from each ensemble. However, the modified boundary condition rendered one configuration on the coarse ensemble exceptional and the multigrid solver was unable to converge; therefore, we omitted this configuration and used only 53 on the coarse ensemble. In addition, on the coarse ensemble we also performed a cross-check using different kinematics, $p, p' \in \{\frac{2\pi}{L}(k, k, 0, 0), \frac{2\pi}{L}(k, 0, k, 0)\}$, which ensure that in the RI-SMOM setup the components of $p' - p$ are not larger than those of p and p'. Since the primary kinematics have p and p' oriented along a four-dimensional diagonal and the alternative kinematics have them oriented along a two-dimensional diagonal, these setups will sometimes be referred to as 4d and 2d, respectively.

After perturbatively matching the RI′-MOM or RI-SMOM data to the $\overline{\text{MS}}$ scheme and evolving to the scale 2 GeV, there will still be residual dependence on the non-perturbative scale μ^2 due to lattice artifacts and truncation of the perturbative series. To control these artifacts, we perform fits including terms polynomial in μ^2 and also, following Ref. [29], a pole term. Our fit function has the form $A + B\mu^2 + C\mu^4 + D/\mu^2$; the constant term A serves as our estimate of the relevant ratio of renormalization

factors $Z_{\mathcal{O}}/Z_V$. We also consider fits without the pole term, i.e., with $D = 0$. We use two different fit ranges: 4 to 20 GeV^2 and 10 to 30 GeV^2.

The main results on the two ensembles are shown in Fig. 3-9. The RI-SMOM data are generally very precise (more so than the RI′-MOM data), which makes the fit quality very poor in many cases. If the covariance matrix from the RI′-MOM data is used when fitting to the RI-SMOM data, then the fit qualities are good except for some of the fits without a pole term for the axial and tensor bilinears. For the RI′-MOM data, the fit quality is good when using a pole term and also good for the scalar bilinear when omitting the pole term. Therefore, we elect to always include the pole term in our fits for Z_A/Z_V and Z_T/Z_V. For Z_S/Z_V we use fits both with and without the pole term, however the fit with a pole term to the RI′-MOM data is very noisy and therefore we exclude it.

To account for the poor fit quality for some of the RI-SMOM fits, we scale the statistical uncertainty of the estimated ratio of renormalization factors by $\sqrt{\chi^2/\text{dof}}$ whenever this is greater than one. For each intermediate scheme, we take the unweighted average of all fit results as the central value, the maximum of the statistical uncertainties, and the root-mean-square deviation of the fit results as the systematic uncertainty. We combine results from both schemes in the same way to produce our final estimates, with the constraint that both schemes are given equal weight. These estimates are also shown in Fig. 3-9. For Z_S/Z_V there is a large discrepancy between the two intermediate schemes, which leads to a large systematic uncertainty. This discrepancy is smaller on the fine ensemble, suggesting that it is caused by lattice artifacts.

Figure 3-10 shows the second set of kinematics on the coarse ensemble. These data do not reach as high in μ^2; therefore, we choose to fit to a single range of 4 to 15 GeV^2. We use the same fit types as for the first set of kinematics, and the results (which can seen from the values of the curves at $\mu^2 = 0$) are consistent with the final estimates from the first set of kinematics.

Our final estimates of the renormalization factors, after adding errors in quadrature, are given in Tab. 3.8. The uncertainty on Z_S is more than 10% and we obtain

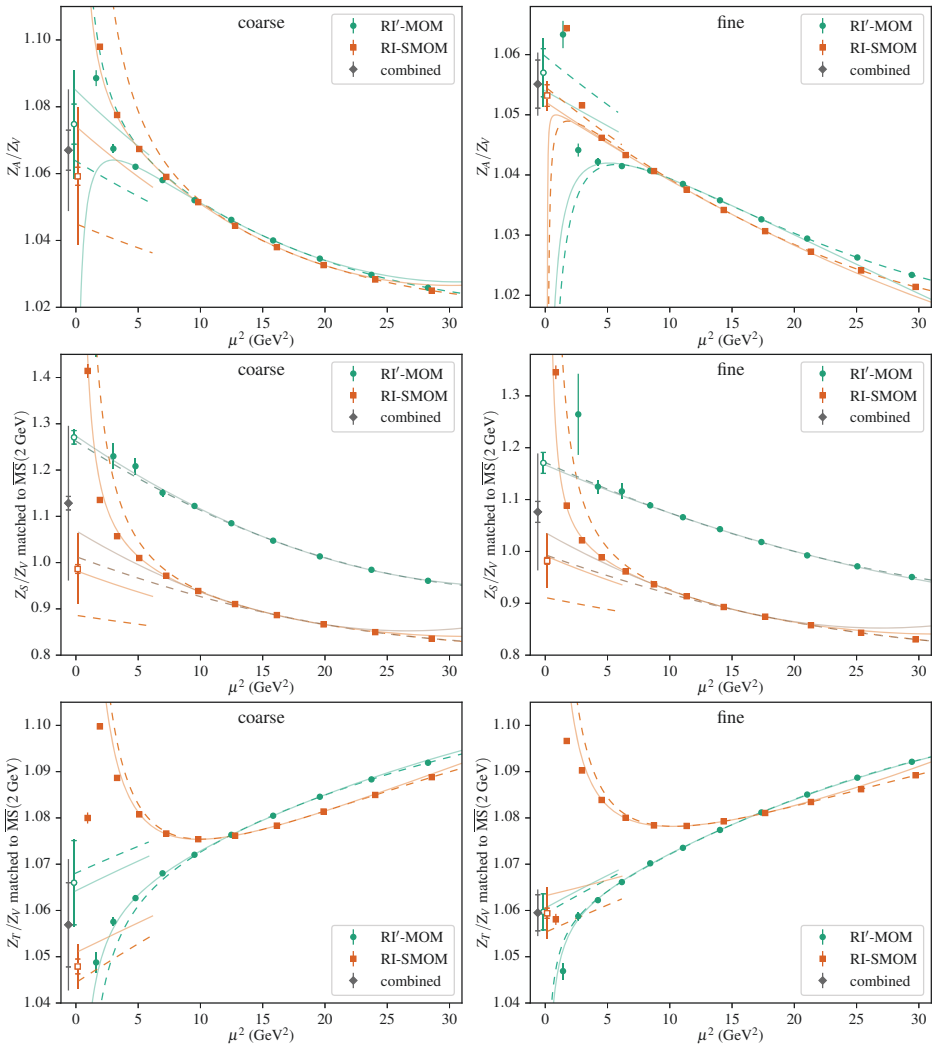

Figure 3-9: Ratios of renormalization factors Z_A/Z_V, Z_S/Z_V, and Z_T/Z_V on the coarse (left) and fine (right) ensembles, determined using the RI′-MOM (green circles) and RI-SMOM (orange squares) intermediate schemes and then matched to $\overline{\text{MS}}$ at scale 2 GeV. For most points, the statistical uncertainty is smaller than the plotted symbol. The solid curves are fits to the μ^2-range from 4 to 20 GeV^2, and the dashed curves are fits to the range 10 to 30 GeV^2. To reduce clutter, uncertainties on the fit curves are not shown. For the fits that include a pole term, the fit curve without the pole term is also plotted, in the range $0 < \mu^2 < 6$ GeV^2. The fits for Z_S/Z_V without a pole term are shown using desaturated colors. The open symbols near $\mu^2 = 0$ provide the final estimate for each intermediate scheme; their outer (without endcap) and inner (with endcap) error bars show the total and statistical uncertainties. The filled dark gray diamonds are the final estimates that combine both schemes.

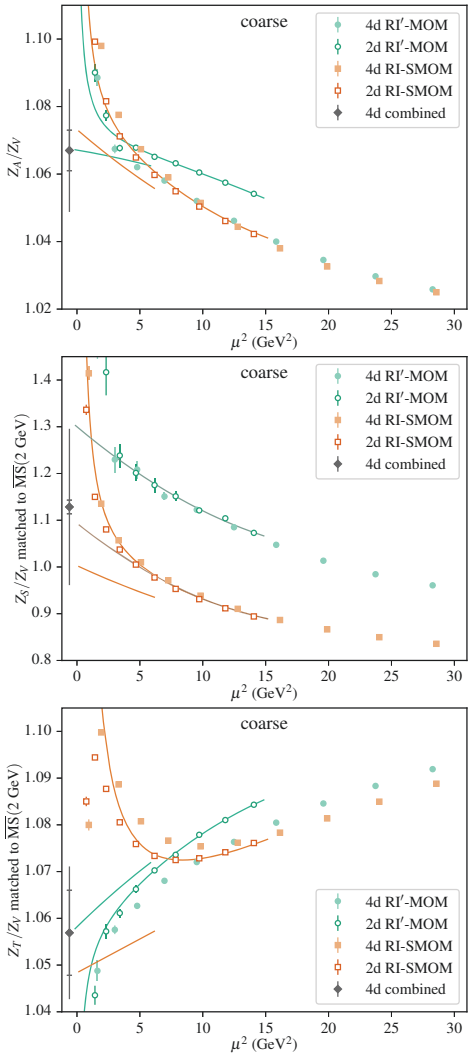

Figure 3-10: Check of alternative kinematics for ratios of renormalization factors on the coarse ensemble. The data with momenta along four-dimensional diagonals and the final combined estimates are repeated from Fig. 3-9. The points with open symbols have momenta along two-dimensional diagonals and the curves are fits to those points in the μ^2-range from 4 to 15 GeV^2. For the fits that include a pole term, the fit curve without the pole term is also plotted, in the range $0 < \mu^2 < 6$ GeV^2. The fits for Z_S/Z_V without a pole term are shown using desaturated colors.

	Z_V	Z_A	Z_S	Z_T
coarse	0.9094(36)	0.9703(170)	1.0262(1521)	0.9611(134)
fine	0.9438(1)	0.9958(50)	1.0157(1065)	0.9999(48)

Table 3.8: Final estimates of renormalization factors on the two ensembles.

	Z_A	Z_S	Z_T
coarse	0.9086(21)(111)	1.115(17)(30)	0.9624(62)
fine	0.9468(6)(56)	1.107(16)(22)	1.011(5)
reference	[48]	[49]	[62]

Table 3.9: Previously used renormalization factors for this lattice action and these two lattice spacings.

percent-level uncertainties on Z_A and Z_T. In previous publications of our group using this lattice action [62, 63, 74], different values for these renormalization factors were used, which are listed in Tab. 3.9. These previous values were all obtained using an RI$^{(\prime)}$-MOM type scheme. Because of our large uncertainty, Z_S is in agreement with the previous value. The latter is also in agreement with our result from only the RI$'$-MOM scheme. Our result for Z_T is also consistent with the previous value. However, we find that Z_A is 5–7% higher than the values previously used, a discrepancy of three standard deviations on the coarse lattice spacing and more than six on the fine one. The previous values would imply that Z_A/Z_V is within about one percent of unity for both lattice spacings, which is very difficult to reconcile with Fig. 3-9.

3.4 Renormalized charges

Multiplying the bare charges in Tab. 3.7 by the renormalization factors in Tab. 3.8 and adding the uncertainties in quadrature, we obtain the renormalized charges on the two ensembles, shown in Tab. 3.10. The final values should be obtained at the

Ensemble	g_A	g_S	g_T
coarse	1.244(28)	0.759(136)	0.989(23)
fine	1.265(24)	0.927(112)	0.972(24)

Table 3.10: Renormalized charges on the two ensembles.

physical pion mass, in the continuum and in infinite volume. Since both ensembles have pion masses very close to the physical pion mass and have large volumes, we neglect these effects as their contribution to the overall uncertainty is relatively small. With two lattice spacings, we are unable to fully control the continuum limit; instead, we choose to account for discretization effects by taking the central value from the fine ensemble and quoting an uncertainty that covers the spread of uncertainties on both ensembles, i.e., $\delta g_X = \max(\delta g_X^f, |g_X^c - g_X^f| + \delta g_X^c)$, where g_X^c and g_X^f denote the charge computed on the coarse and fine ensembles, respectively. We obtain

$$g_A = 1.265(49), \tag{3.10}$$

$$g_S = 0.927(303), \tag{3.11}$$

$$g_T = 0.972(41). \tag{3.12}$$

The overall uncertainties for the axial and tensor charges are roughly 4%. The scalar charge has a much larger uncertainty, due to the large uncertainty in the renormalization factor and the large difference in central values between the two ensembles.

Results on these two ensembles can be compared with earlier calculations of our group using the same lattice action and heavier pion masses [62, 63], reevaluating those earlier works based on the more extensive study of excited-state effects in Section 3.2 and using the renormalization factors from Section 3.3. For g_A, the summation method with $T_{\text{min}} \approx 0.7$ fm was found to be acceptable; therefore, we reuse the summation-method results from Ref. [63], which had $T_{\text{min}} \approx 0.9$ fm. For g_T, we found that the ratio method with the middle separation ($T \approx 1.2$ fm), as used in Ref. [62] was inadequate; instead we will use the summation method. Finally, for g_S the large statistical uncertainty means that the source-sink separation used in Ref. [62] with the ratio method was larger than necessary, and here we will take the shortest separation ($T \approx 0.9$ fm) rather than the middle one.

The comparison with the earlier results is shown in Fig. 3-11. In these plots, the ensembles used for a study of short time-extent effects are excluded and for two ensembles at $m_\pi \approx 250$ MeV of size $32^3 \times 48$ and $24^3 \times 48$, we have increased statistics.

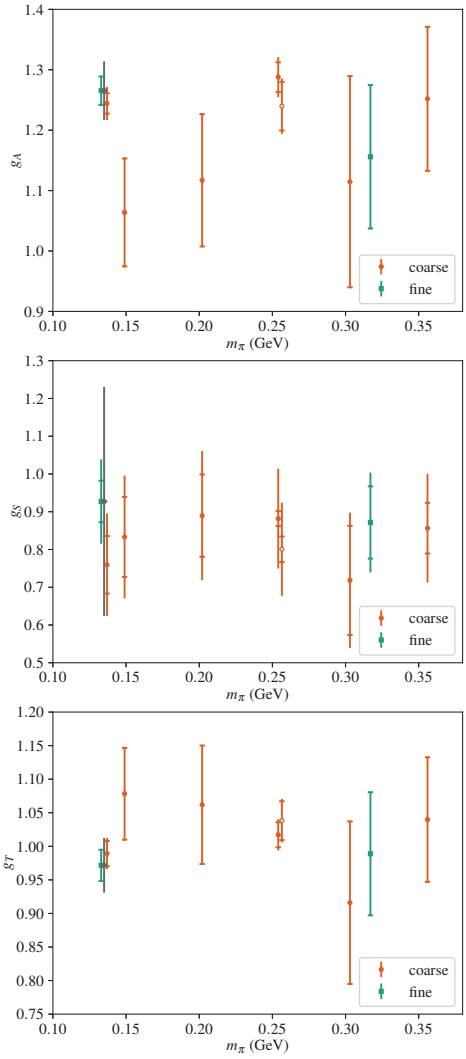

Figure 3-11: Isovector charges g_A, g_S, and g_T versus pion mass. The inner error bars exclude the uncertainty on the renormalization factor, which is fully correlated across all ensembles with the same lattice spacing. The smaller of the two volumes at $m_\pi \approx 0.25$ GeV is displaced horizontally and indicated with an open symbol. The final estimates based on the two physical-point ensembles are indicated by the dark gray diamonds.

The data show no significant dependence on the pion mass, which justifies our neglect of this effect in the final values of the charges. If we assume that finite-volume effects scale as $m_\pi^2 e^{-m_\pi L}/\sqrt{m_\pi L}$ as for the axial charge in chiral perturbation theory at large $m_\pi L$ [18], then the finite-volume correction can be obtained by multiplying the difference between the two volumes at $m_\pi \approx 250$ MeV by 0.28 and 0.23 for the coarse and fine physical-pion-mass ensembles, respectively. One can see that this effect is also small compared with the final uncertainties.

This comparison provides the opportunity to revisit the result for g_A obtained earlier by our group in Ref. [63], which was unusually low. This was partly caused by the lower value of Z_A, but the value obtained for $m_\pi = 149$ MeV is still two standard deviations below the physical-point coarse ensemble. It appears that this is a statistical fluctuation, since the methodology has not been significantly changed.

3.5 Summary and outlook

We have computed the nucleon isovector axial, scalar, and tensor charges using two 2+1-flavor ensembles with a 2-HEX-smeared Wilson-clover action. Both ensembles are at the physical pion mass and have lattice spacings of 0.116 and 0.093 fm. We have demonstrated control over excited-state contamination by using eight source-sink separations in the range from roughly 0.4 to 1.4 fm on the coarse ensemble and three source-sink separations in the range from 0.9 to 1.5 fm on the fine ensemble. The shorter source-sink separations are useful for the summation method but larger ones are needed for the ratio method. In addition, the choice of T is observable-dependent: if excited-state effects are drowned out by noise, then shorter separations are more useful. We have studied a range of different fitting strategies to extract the different charges of the nucleon from ratios of correlation functions, namely the ratio, two-state fit to the ratios, summation method, two-state fit to the summations (only on the coarse ensemble). We have studied the stability of the different analysis methods and designed a procedure for combining the multiple estimates obtained for each observable and giving an estimate of its final value. We have observed consistency between

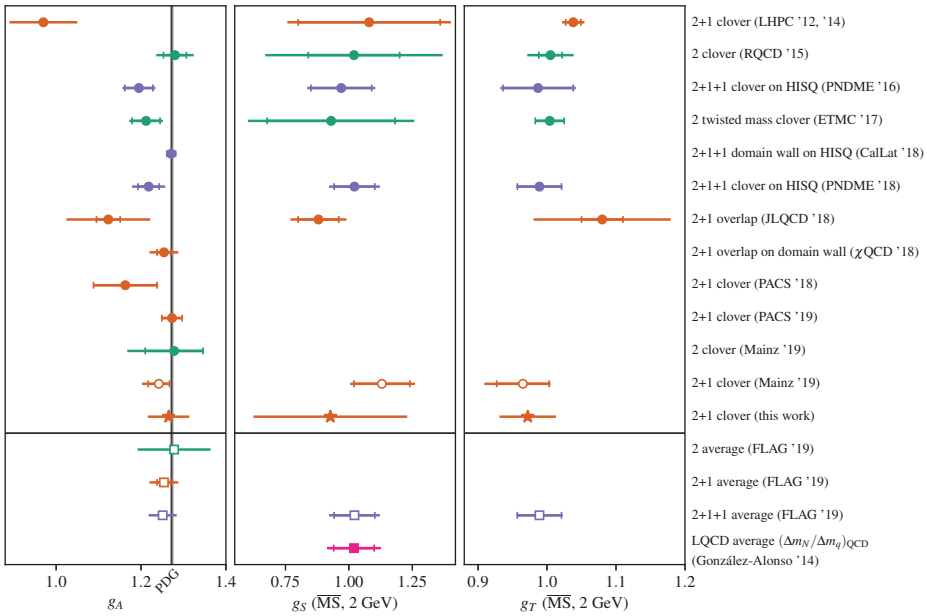

Figure 3-12: Recent lattice calculations of g_A, g_S, and g_T [62, 63, 15, 26, 3, 5, 37, 121, 41, 91, 68, 79, 113, 71]. When separate statistical and systematic errors are quoted, the inner error bar (with endcap) indicates the statistical uncertainty and the outer one (without endcap) gives the quadrature sum. Open and filled symbols denote unpublished and published work. Green, orange, and blue denote calculations done with 2, $2+1$, and $2+1+1$ dynamical quark flavors, which is also indicated in the legend. Circles are used for individual calculations and this work is indicated with stars. Squares are used for the averages from FLAG [8] and for the determination of g_S using the conserved vector current relation and lattice QCD input [58]. The vertical line with gray error band indicates the PDG value for g_A [117].

the different analysis methods, although within larger error bars for the scalar charge. We have determined the renormalization factors for the different observables using the nonperturbative Rome-Southampton approach and compared between the RI′-MOM and RI-SMOM intermediate schemes to estimate the systematic uncertainties.

Our final results are given in Eqs. ((3.10)–(3.12)). The axial and tensor charges show overall uncertainties of roughly 4%. The obtained scalar charge, however, shows a much larger uncertainty, due to the large uncertainty in the renormalization factor and the large difference in the central values we observe between the the coarse and fine ensembles. In this study, since both ensembles have pion masses very close to the physical pion mass and have large volumes, we neglect the pion-mass dependence and finite volume effects. We have shown that this is justified when comparing our results to earlier calculations using the same lattice action and heavier pion masses. This calculation supersedes the earlier ones since it improves on them by working directly at the physical pion mass, using much higher statistics, and performing a more extensive study of excited-state effects.

Recent lattice calculations of the isovector charges are summarized in Fig. 3-12, although we caution that many of them leave some sources of systematic uncertainty uncontrolled or unestimated; see the FLAG review [8] for details. Our results are consistent with most of these previous calculations and also with the PDG value of g_A. In our calculation, we have found a large discrepancy for Z_S between the two intermediate renormalization schemes; it would be therefore useful to verify whether this goes away at finer lattice spacings, and to compare against other approaches such as the Schrödinger functional [35] or position-space [56] methods.

Chapter 4

Computing the nucleon charge and axial radii directly at $Q^2 = 0$

The conventional approach for determining quantities like the charge radius on the lattice involves the computation of form factors at several different discrete values of the initial and final momenta, $\vec{p}$ and $\vec{p}'$, that are allowed by the periodic boundary conditions, followed by a large extrapolation to zero momentum transfer $Q^2 = 0$. This introduces a source of systematic uncertainty, analogous to the systematic uncertainty associated with the choices of the fit ansatz and range of Q^2 in extracting the proton charge radius from electron-proton scattering data. Systematic errors of this kind have in fact been proposed as a possible explanation of the radius puzzle [94, 67, 76]. Given that the smallest nonzero value of Q^2 accessible on the largest available lattices is still an order of magnitude higher than in scattering experiments [20], a lattice method for computing r_E^p and similar observables directly at $Q^2 = 0$ without the need of a shape fit is highly desirable.

We compute the nucleon radii using the *derivative method* that enables the computation of the radii directly at zero momentum transfer and provides a way to avoid the model-dependence included in the conventional approach. The momentum derivative method relies on the Rome method [46] for computing the momentum derivatives of the quark propagators. We compute the nucleon radii using two variations of the momentum derivative approach. The first, which we presented in Refs. [72, 74],

involves computing the first- and second-order momentum derivatives of the quark propagators with respect to the initial-state momenta. We found that this variation results in large statistical errors for the isovector charge radius. This motivated our second variation which was presented at the Lattice 2017 conference [73] and involves the computation of the mixed-momentum derivatives of three-point functions that are first-order momentum derivatives with respect to both initial- and final-state momenta.

In this chapter, we present our results for the proton isovector charge radius $(r_E^2)^v$ and the isovector magnetic moment $\mu^v = G_M^v(0)$, from matrix elements of the vector current, in addition to the proton axial radius r_A^2 and the induced pseudoscalar form factor at zero momentum, $G_P(0)$, using nucleon matrix elements of the axial current. We perform those calculations using both variations of the derivative method and compare the estimated values of the different observables to their estimations from the conventional approach.

The outline of this chapter is as follows. Section 4.1 explains in detail both variations of the derivative method for computing the momentum derivatives of matrix elements at $Q^2 = 0$ using the Rome method, which we use to determine the charge and axial radii in addition to the magnetic and induced pseudoscalar form factors directly at $Q^2 = 0$. In Sec. 4.2, we present our numerical results. In this section, we include earlier results from Ref. [74] obtained on the fine ensemble where we have compared only between the first variation of the derivative method and the conventional method. We then present our results from the coarse ensemble where we test both variations of the derivative method and compare to the conventional approach. We give our conclusions in Sec. 4.3.

4.1 The derivative method

In this section, we explain the details of our approach for extracting the nucleon charge radius directly at $Q^2 = 0$. We begin with reviewing the Rome method for computing the momentum derivatives of quark propagators in Sec. 4.1.1. The flavor structure of the correlators constructed from the momentum derivatives of the quark propagators is investigated in Sec. 4.1.2. In Sec. 4.1.3, we show how to use the momentum derivatives of the quark propagator for obtaining the momentum derivatives of the nucleon two- and three-point functions with respect to both the initial- and final-state momenta $\vec{p}, \vec{p}'$, from which we compute the momentum derivatives of matrix elements in Sec. 4.1.4. From the latter, one can then extract the charge radius r_E^2, the magnetic moment $\mu = G_M(0)$, for the case of the electromagnetic vector current, and the axial radius, r_A^2, and induced pseudoscalar form factor at zero momentum, $G_P(0)$, for the case of the axial current.

4.1.1 Momentum derivatives of quark propagator

On a lattice with finite size and quark fields satisfying periodic boundary conditions, consider a generic correlation function $C(\vec{p}, t)$ depending on the three-momentum $\vec{p}$ and Euclidean time t, which after fermionic integration and Wick contractions can be written in terms of quark propagators and operator insertions as

$$C(\vec{p}, t) = \int dU P[U] \sum_{\vec{x},\ldots} e^{-i\vec{p}(\vec{x}-\vec{y})} \operatorname{Tr}\{S[x, y; U]\Gamma \ldots\}, \tag{4.1}$$

where U are gauge links and $P[U]$ is the corresponding probabilistic weight in the functional integral. The plane-wave phase factor $e^{-i\vec{p}(\vec{x}-\vec{y})}$ can then be absorbed into one of the quark propagators, which results in a momentum dependent quark propagator $S[x, y; U, \vec{p}] = e^{-i\vec{p}(\vec{x}-\vec{y})} S[x, y; U]$. $S[x, y; U, \vec{p}]$ can be obtained by solving the lattice Dirac equation with link variables rescaled by a phase factor

$$U_k(x) \to e^{iap_k} U_k(x), \tag{4.2}$$

$$\sum_y D[x,y;U,\vec{p}]S[y,z;U,\vec{p}] = \delta_{x,z}. \tag{4.3}$$

Carrying momentum in a propagator with a uniform $U(1)$ background field is the same approach as used in a standard transformation of twisted boundary conditions [19, 45]. With $\vec{p}$ restricted to be a Fourier momentum in the finite volume, the above redefinition is exact. However, to obtain a momentum derivative, we must implicitly make use of twisted boundary conditions and allow $\vec{p}$ to be continuous. We use the expansion of the lattice Dirac operator

$$D[U,\vec{p}] = D[U] + p_k \frac{\partial D}{\partial p_k}\Big|_{\vec{p}=\vec{0}} + \frac{p_k^2}{2}\frac{\partial^2 D}{\partial p_k^2}\Big|_{\vec{p}=\vec{0}} + \ldots, \tag{4.4}$$

and $D[U,\vec{p}]S[U,\vec{p}] = 1$ to compute the first-order momentum derivative of the propagator as

$$\frac{\partial D}{\partial p_k} S + D \frac{\partial S}{\partial p_k} = 0, \tag{4.5}$$

where we use the compact notation

$$\frac{\partial D}{\partial p_k} \equiv \frac{\partial D[\ldots;U,\vec{p}]}{\partial p_k}\Big|_{\vec{p}=0}, \tag{4.6}$$

and similar notation for $S(\ldots;U,\vec{p})$. Multiplying Eq. (4.5) from the left by $S \equiv D^{-1}$ leads to

$$\frac{\partial S}{\partial p_k} = -S\frac{\partial D}{\partial p_k}S. \tag{4.7}$$

Similarly, we can derive the second-order momentum derivative of the propagator

$$\frac{1}{2}\frac{\partial^2 S}{\partial p_k^2} = +S\frac{\partial D}{\partial p_k}S\frac{\partial D}{\partial p_k}S - S\frac{1}{2}\frac{\partial^2 D}{\partial p_k^2}S. \tag{4.8}$$

Using the lattice Dirac operator for the clover-improved Wilson action, the momentum derivatives of the propagators at a fixed gauge background become [46]

$$\frac{\partial}{\partial p_k} S(x,y;\vec{p})\Big|_{\vec{p}=\vec{0}} = -i\sum_z S(x,y)\Gamma_V^k S(x,y), \tag{4.9}$$

$$\frac{\partial^2}{\partial p_k^2} S(x,y;\vec{p})\Big|_{\vec{p}=\vec{0}} = -2\sum_{z,z'} S(x,z)\Gamma_V^k S(z,z')\Gamma_V^k S(z',y) - \sum_z S(x,z)\Gamma_T^k S(z,y). \tag{4.10}$$

We drop U from the propagators for brevity. Γ_V^k and Γ_T^k are the point split vector and tadpole currents, respectively. Those are defined using Euclidean gamma matrices, γ_E^k, as

$$\Gamma_V^k S(z,y;U) \equiv U_j^\dagger(z-\hat{k})\frac{1+\gamma_E^k}{2}S(z-\hat{k},y) - U_k(z)\frac{1-\gamma_E^k}{2}S(z+\hat{k},y), \tag{4.11}$$

$$\Gamma_T^k S(z,y;U) \equiv U_j^\dagger(z-\hat{k})\frac{1+\gamma_E^k}{2}S(z-\hat{k},y) + U_k(z)\frac{1-\gamma_E^k}{2}S(z+\hat{k},y). \tag{4.12}$$

In the case of a smeared-source smeared-sink propagator (needed in the two-point function), the phase factor can be absorbed into the propagator in the following way

$$\begin{aligned}\tilde{\tilde{S}}(x,y;\vec{p}) &= e^{-i\vec{p}(\vec{x}-\vec{y})}\sum_{x',y'} K(x,x')S(x',y')K(y',y) \\ &= \sum_{x',y'} \underbrace{e^{-i\vec{p}(\vec{x}-\vec{x}')}K(x,x')}_{K(x,x';\vec{p})}\underbrace{e^{-i\vec{p}(\vec{x}'-\vec{y}')}S(x',y')}_{S(x',y';\vec{p})}\underbrace{e^{-i\vec{p}(\vec{y}'-\vec{y})}K(y',y)}_{K(y',y;\vec{p})},\end{aligned} \tag{4.13}$$

where K is the smearing kernel. The momentum derivatives can then be calculated using the product rule along with Eq. (4.9) and Eq. (4.10). Denoting the momentum derivative with $'$ for shorter notation, we obtain

$$(KSK)' = K'SK + K(SK)', \tag{4.14}$$

$$(KSK)'' = K''SK + 2K'(SK)' + K(SK)''. \tag{4.15}$$

For the smeared-source point-sink propagator, which is needed for the three-point function and for evaluating Eq. (4.14) and Eq. (4.15), we obtain

$$(SK)' = S[-i\Gamma_V SK + K'], \tag{4.16}$$

$$(SK)'' = S[-2i\Gamma_V(SK)' - \Gamma_T SK + K'']. \tag{4.17}$$

Organized in this way, we have one additional propagator right-hand-side per derivative. Gaussian Wuppertal smearing [69] is given by

$$K(x,y;\vec{p}) = \sum_{x',x'',\ldots} \underbrace{K_0(x,x';\vec{p})K_0(x',x'';\vec{p})\ldots K_0(x^{'\cdots'},y;\vec{p})}_{N_W}, \tag{4.18}$$

with

$$\begin{aligned} K_0(x,y;\vec{p}) &= e^{-i\vec{p}(\vec{x}-\vec{y})}\frac{1}{1+6\alpha}\left(\delta_{x,y} + \alpha\sum_{j=1}^{3}\Big[\ \tilde{U}_j(x)\delta_{x+\hat{\jmath},y} + \tilde{U}_j^\dagger(x-\hat{\jmath})\delta_{x-\hat{\jmath},y}\Big]\right) \\ &= \frac{1}{1+6\alpha}\left(\delta_{x,y} + \alpha\sum_{j=1}^{3}\Big[e^{ip^j}\tilde{U}_j(x)\delta_{x+\hat{\jmath},y} + e^{-ip^j}\tilde{U}_j^\dagger(x-\hat{\jmath})\delta_{x-\hat{\jmath},y}\Big]\right). \end{aligned} \tag{4.19}$$

We use APE-smeared gauge links $\tilde{U}$ [2]. The mth derivative of K_0 at zero momentum is equal to

$$K_0^{(m)}(x,y) \equiv \Big(\frac{\partial}{\partial p^j}\Big)^m K_0(x,y;\vec{p})\bigg|_{\vec{p}=0} = \frac{\alpha}{1+6\alpha}\Big[i^m\tilde{U}_j(x)\delta_{x+\hat{\jmath},y} + (-i)^m\tilde{U}_j^\dagger(x-\hat{\jmath})\delta_{x-\hat{\jmath},y}\Big]. \tag{4.20}$$

Thus, the first- and second-order momentum derivatives of smearing with N_W iterations, $K = K_0^{N_W}$, can be computed iteratively using

$$(K_0^N)' = K_0'K_0^{N-1} + K_0(K_0^{N-1})', \tag{4.21}$$

$$(K_0^N)'' = K_0''K_0^{N-1} + 2K_0'(K_0^{N-1})' + K_0(K_0^{N-1})''. \tag{4.22}$$

4.1.2 Flavor structure of correlators constructed from propagator derivatives

In cases where derivatives of nucleon two-point functions need to be evaluated, there is an ambiguity in applying the above procedure: there are three quark propagators, and the momentum could be absorbed into any of them. To resolve this issue, we make explicit use of twisted boundary conditions, with the understanding that before computing any correlation functions we will take the derivative with respect to the

twist angle, at vanishing twist angle.

We introduce a third light quark, r, with the same mass as u and d but with twisted boundary conditions, and a corresponding ghost quark that cancels its fermion determinant. The three light quarks $\{u, d, r\}$ contain an approximate SU(3) flavor symmetry that becomes exact when the twist angle is zero, or in the infinite-volume limit. Under this symmetry group there is a baryon octet that contains the ordinary (untwisted) nucleons, as well as states with one or two r quarks. We are interested in the states with one r quark, and we find that there are two kinds: an isospin singlet and a triplet, the Λ_r and Σ_r, respectively. This was previously discussed in Ref. [83].

For the states with quark content udr we use interpolating operators

$$\begin{aligned} \chi_{\Sigma_r} &= \frac{1}{\sqrt{2}} \left([rud] + [rdu] \right), \\ \chi_{\Lambda_r} &= \frac{1}{\sqrt{6}} \left(2[udr] - [rud] - [dru] \right), \end{aligned} \tag{4.23}$$

where $[pqr] \equiv \epsilon^{abc} (\tilde{p}_a^T C \gamma_5 \frac{1+\gamma_0}{2} \tilde{q}_b) \tilde{r}_c$. When contracted with the projector $\frac{1+\gamma_0}{2}$, the flavor-singlet operator, $1/\sqrt{3}([udr] + [rud] + [dru])$, vanishes and the Λ_r operator can be simplified to $\chi_{\Lambda_r} = \sqrt{\frac{3}{2}}[udr]$. We consider three-point functions for the transition from a state with one r quark to an ordinary nucleon

$$C_3^{X \to N}(\vec{p}, \vec{p}', \tau, T) = \sum_{\vec{x}, \vec{y}} e^{-i\vec{p}'(\vec{x}-\vec{y})} \operatorname{Tr} \left[\Gamma_{\text{pol}} \langle \chi(\vec{x}, T) \mathcal{O}(\vec{y}, \tau) \bar{\chi}_X(0) \rangle \right], \tag{4.24}$$

where $\mathcal{O} = \bar{u} \Gamma r$ is a quark bilinear and X is Σ_r or Λ_r. The initial momentum $\vec{p}$ is implied in the initial state due to the twisted boundary conditions for the r quark. The ground-state contribution is proportional to the matrix element $\langle N(\vec{p}') | \mathcal{O} | X(\vec{p}) \rangle$ for which we will evaluate $\frac{\partial}{\partial \vec{p}}$ at $\vec{p}' = \vec{p} = 0$. In practice, we simply use our already coded expressions for the connected diagrams in the nucleon three-point functions C_3^q with $\mathcal{O}_q = \bar{q} \Gamma q$, $q \in \{u, d\}$, and replace the propagator connecting the nucleon source and $\mathcal{O}_q$ with a first- or second-derivative propagator.

By comparing the contractions, we find the relations

$$\begin{aligned} C_3^{\Sigma_r \to N} &= \frac{1}{\sqrt{2}} C_3^d, \\ C_3^{\Lambda_r \to N} &= \frac{1}{\sqrt{6}} \left(2C_3^u - C_3^d\right), \end{aligned} \tag{4.25}$$

where the r propagator is substituted into the evaluation of the right-hand-side expressions as described above. A similar consideration was made in Ref. [83]; these relations could also be derived from SU(3) symmetry.

When forming ratios, we must use the appropriate two-point functions: taking Eq. (2.48) with the three-point function $C_3^{X \to N}$, all nucleon two-point functions that take the initial-state momentum $\vec{p}$ must be replaced by the two-point function for state X. Once we have formed the ratios for the $X \to N$ matrix elements, we can invert the relations in Eq. (4.25) to obtain the nucleon matrix elements of $\mathcal{O}_u$ and $\mathcal{O}_d$.

4.1.3 Momentum derivatives of correlation functions

Derivation with respect to $\vec{p}$

Let us consider the two-point function of the isospin singlet operator, $\chi_{\Lambda_r} = \sqrt{\frac{3}{2}}[udr]$. This can be written in terms of smeared-source smeared-sink quark propagators, $\tilde{\tilde{S}}$, as

$$\begin{aligned} C_2^{\Lambda_r}(\vec{p}, t) &= \frac{3}{2} \sum_{\vec{x}} e^{-i\vec{p}\vec{x}} \epsilon^{abc} \epsilon^{def} \sum_{\alpha\beta} (\Gamma_{\text{pol}})_{\alpha\beta} f_{\beta\gamma\delta\epsilon} \bar{f}_{\alpha\zeta\eta\theta} \left\langle \tilde{\tilde{S}}^{af}_{\gamma\theta}(x,0) \tilde{\tilde{S}}^{be}_{\delta\eta}(x,0) \tilde{\tilde{S}}^{cd}_{\epsilon\zeta}(x,0) \right\rangle_U \\ &= \frac{3}{2} \sum_{\vec{x}} \epsilon^{abc} \epsilon^{def} \sum_{\alpha\beta} (\Gamma_{\text{pol}})_{\alpha\beta} f_{\beta\gamma\delta\epsilon} \bar{f}_{\alpha\zeta\eta\theta} \left\langle \tilde{\tilde{S}}^{af}_{\gamma\theta}(x,0) \tilde{\tilde{S}}^{be}_{\delta\eta}(x,0) \tilde{\tilde{S}}^{cd}_{\epsilon\zeta}(x,0;\vec{p}) \right\rangle_U, \end{aligned} \tag{4.26}$$

where $f_{\beta\gamma\delta\epsilon}$ is the spin tensor determining the quantum numbers of the Λ_r and $\tilde{\tilde{S}}(x,0;\vec{p}) = e^{-i\vec{p}\vec{x}} \tilde{\tilde{S}}(x,0)$. By using the first- and second-order momentum derivatives of a quark propagator at zero momentum given in Eq. (4.9) and Eq. (4.10), one can straightforwardly calculate the momentum derivatives of the two-point correlators.

For connected diagrams, the three-point function with current $O_\Gamma = \bar{q}\Gamma q$ and zero

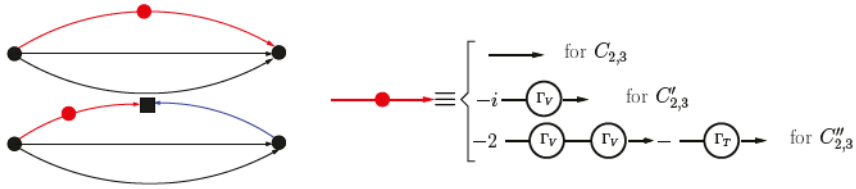

Figure 4-1: Left: Nucleon two-point (top) and three-point (bottom) functions . The solid black circles represent the nucleon source and sink, the black square in the three-point function represents the current insertion. The red line refers to the propagator which we use for computing the momentum derivatives of the correlators with respect to the initial-state momentum, this carries therefore the derivative vertex (solid red circle). The right panel shows the representation of the derivative vertex for the simplified case of unsmeared propagators.

sink momentum $\vec{p}' = 0$ can be written as

$$C_3(\vec{p},\tau,T) = \sum_{\vec{x},\vec{y}} e^{-i\vec{p}\vec{y}} \sum_{\alpha\beta} (\Gamma_{\text{pol}})_{\alpha\beta} \left\langle \chi_\beta(\vec{x},T) O_\Gamma(\vec{y},\tau) \bar{\chi}_\alpha(0) \right\rangle \sim \sum_{\vec{y}} \left\langle G_S(y) \Gamma \tilde{S}(y,0;\vec{p}) \right\rangle_U , \tag{4.27}$$

where $\tilde{S}$ refers to a propagator with smeared source and point sink and $G_S(y)$ is the sequential backward propagator, which is independent of $\vec{p}$. Only the forward propagator $\tilde{S}(y,0;\vec{p})$ needs to be expanded using Eq. (4.9) and Eq. (4.10). Hence, no additional backward propagators are needed. Figure 4-1 shows graphically the way we compute the momentum derivatives of the correlation functions with respect to $\vec{p}$ on the quark level. The derivative method cannot be applied to disconnected diagrams because those involve a quark propagating from a point to the same point and therefore the momentum transfer can not be absorbed into the propagator.

Mixed derivation with respect to $\vec{p}$ and $\vec{p}'$

The three-point function with current $O_\Gamma = \bar{q}\Gamma q$ can be written in terms of the sequential propagators as follows,

$$\begin{aligned}\mathrm{Tr}\left[C_3(\vec{p},\vec{p}',\tau,T)\Gamma_{\mathrm{pol}}\right] &= \sum_{\vec{x},\vec{y}} e^{-i\vec{p}'(\vec{x}-\vec{y})} e^{-i\vec{p}\vec{y}} \left\langle \mathrm{Tr}\left[S_{\Gamma_{\mathrm{pol}}}(0;x)S(x,y)\Gamma S(y,0)\right]\right\rangle_U \\ &= \sum_{\vec{x},\vec{y}} \left\langle \mathrm{Tr}\left[\left(\gamma_5 S(y,x;\vec{p}')\gamma_5 S^\dagger_{\Gamma_{\mathrm{pol}}}(0;x)\right)^\dagger \Gamma S(y,0;\vec{p})\right]\right\rangle_U ,\end{aligned} \tag{4.28}$$

where $S_{\Gamma_{\mathrm{pol}}}(0;x)$ is the sequential source. The mixed derivative of the three-point function with respect to the initial- and final-state momenta is

$$\begin{aligned}&\frac{\partial}{\partial p'^j}\frac{\partial}{\partial p^k} C_3(\vec{p},\vec{p}',\tau,T)\bigg|_{\vec{p}'=\vec{p}=0} = \\ &\qquad \sum_{\vec{x},\vec{y}} \left\langle \mathrm{Tr}\left[\left(\gamma_5 \frac{\partial S(y,x;\vec{p}')}{\partial p'^j}\bigg|_{\vec{p}'=0} \gamma_5 S^\dagger_{\Gamma_{\mathrm{pol}}}(0;x)\right)^\dagger \Gamma \frac{\partial S(y,0;\vec{p})}{\partial p^k}\bigg|_{\vec{p}=0}\right]\right\rangle_U .\end{aligned} \tag{4.29}$$

This mixed-momentum derivative of the three-point function is required when using our second variation of the derivative approach.

4.1.4 Momentum derivatives of matrix elements

Derivation with respect to $\vec{p}$

This variation of the derivative method enables one to extract the charge radius and other observables at $Q^2 = 0$ by computing the first- and second-order momentum derivatives of the correlation functions.

Because we do not know how $Z(\vec{p})$ depends on the momentum, we need to compute the momentum derivatives of the ratio of three-point and two-point functions given in Eq. (2.48). Here and in the following, we use Minkowski-space gamma matrices. We set $\vec{p}' = 0$ and $\vec{p} = k\vec{e}_j$, where $\vec{e}_j$ is the unit vector in j-direction. For computing

the first- and second-order momentum derivatives of the ratio in Eq. (2.48), we start by computing the momentum derivatives of the normalization ratio part, R_N^X, defined in Eq. (2.46)

$$\left(R_N^X(k)\right)' = \frac{-C_2'(k)C_3(k) + 2C_2(k)C_3'(k)}{2\sqrt{C_2(0)C_2(k)^3}}, \tag{4.30}$$

$$\left(R_N^X(k)\right)'' = \frac{(3[C_2'(k)]^2 - 2C_2(k)C_2''(k))C_3(k) + 4C_2(k)(-C_2'(k)C_3'(k) + C_2(k)C_3''(k))}{4\sqrt{C_2(0)C_2(k)^5}}, \tag{4.31}$$

where, for more readability we suppress the τ, T parameters as well as $\mathcal{O}_X^\mu$ from the correlation functions and the ratio. We denote the derivatives with a prime, e.g., $C_2'(k) \equiv \frac{dC_2(k)}{dk}$. We know that $C_2'(0) = 0$ in the infinite-statistics limit because of parity symmetry. Hence, we can eliminate this from the ratios. Similarly, we can calculate $R_S'(k)$ and $R_S''(k)$ which can be used together with Eq. (4.30) and Eq. (4.31) to calculate the first- and second-order derivatives of the ratio R_X. These derivatives are computed on the lattice directly at $k = 0$. From the ground-state contributions to the correlation functions given in Eq. (2.17) and Eq. (2.23), we find the following ground-state contribution to their ratio

$$R_X(k) = \frac{\mathrm{Tr}\left[\Gamma_{\mathrm{pol}}\mathcal{F}_X(k)(m_N + E\gamma^0 - k\gamma^j)\right]}{2\sqrt{2E(E+m_N)}}. \tag{4.32}$$

We take the derivative with respect to k and obtain

$$\begin{aligned}(R_X)'(k) = &\frac{\mathrm{Tr}\left[\Gamma_{\mathrm{pol}}\left(\mathcal{F}_X'(k)(m_N + E\gamma^0 - k\gamma^j) + \mathcal{F}_X(k)(E'\gamma^0 - \gamma^j)\right)\right]}{2\sqrt{2E(E+m_N)}} \\ &- \frac{\mathrm{Tr}\left[\Gamma_{\mathrm{pol}}\mathcal{F}_X(k)(m_N + E\gamma^0 - k\gamma^j)\right](2E + m_N)E'}{4\sqrt{2}[E(E+m_N)]^{3/2}}.\end{aligned} \tag{4.33}$$

$(R_X)''(k)$ can be calculated in a similar way. We use the continuum dispersion relation $E(k) = \sqrt{m_N^2 + k^2}$, which implies $Q^2 = 2m_N\sqrt{m_N^2 + k^2} - 2m_N^2$, and find that at

$k = 0$, the second derivative is needed to obtain the slope of F_1

$$\frac{dF_1}{dk}\Big|_{k=0} = \frac{dQ^2}{dk}\Big|_{k=0}\frac{dF_1}{dQ^2}\Big|_{Q^2=0} = 0, \qquad \frac{d^2F_1}{dk^2}\Big|_{k=0} = 2\frac{dF_1}{dQ^2}\Big|_{Q^2=0}. \tag{4.34}$$

The same applies for F_2, G_A, and G_P. Furthermore, we have at $k = 0$

$$E(0) = m_N, \qquad E'(0) = 0, \qquad E''(0) = 1/m_N, \tag{4.35}$$

$$\mathcal{F}_V(0) = F_1(0)\gamma^\mu, \quad \mathcal{F}'_V(0) = F_2(0)\frac{i\sigma^{\mu j}}{2m_N}, \quad \mathcal{F}''_V(0) = 2\frac{dF_1}{dQ^2}\Big|_{Q^2=0}\gamma^\mu - F_2(0)\frac{i\sigma^{\mu 0}}{2m_N^2}, \tag{4.36}$$

$$\mathcal{F}_A(0) = G_A(0)\gamma^\mu\gamma_5, \quad \mathcal{F}'_A(0) = \begin{cases} -\frac{1}{2m_N}G_P(0)\gamma_5, & \mu = j \\ 0, & \mu \neq j \end{cases}, \tag{4.37}$$

$$\mathcal{F}''_A(0) = 2\frac{d}{dQ^2}G_A(0)\gamma^\mu\gamma_5 + \begin{cases} -\frac{1}{2m_N^2}G_P(0)\gamma_5, & \mu = 0 \\ 0, & \mu \neq 0 \end{cases}. \tag{4.38}$$

For the renormalized vector current, we use $G_E(0) = 1$ and find nonzero results for the following combinations of j and μ

$$R_V^0 = 1, \qquad \partial_1 R_V^2 = -\frac{i}{2m_N}G_M(0), \tag{4.39}$$

$$\partial_2 R_V^1 = \frac{i}{2m_N}G_M(0), \qquad \partial_{1,2,3}^2 R_V^0 = -\frac{1}{4m_N^2} - \frac{1}{3}r_E^2, \tag{4.40}$$

and for the axial current

$$R_A^3 = G_A(0), \qquad \partial_3 R_A^0 = \frac{1}{2m_N}G_A(0), \tag{4.41}$$

$$\partial_{1,2}^2 R_A^3 = -\frac{1}{4m_N^2}G_A(0) - \frac{1}{3}G_A(0)r_A^2, \quad \partial_3^2 R_A^3 = -\frac{1}{4m_N^2}\left(G_A(0) + 2G_P(0)\right) - \frac{1}{3}G_A(0)r_A^2, \tag{4.42}$$

with $\partial_j = \frac{\partial}{\partial p^j}$ and

$$r_E^2 = -\frac{6}{G_E(0)} \left. \frac{dG_E}{dQ^2} \right|_{Q^2=0}, \tag{4.43}$$

$$r_A^2 = -\frac{6}{G_A(0)} \left. \frac{dG_A}{dQ^2} \right|_{Q^2=0}. \tag{4.44}$$

From Eq. (4.39) and Eq. (4.40), we find the following relations for the nucleon magnetic moment $\mu = G_M(0)$ and squared charge radius r_E^2

$$\mu = 2i\, m_N\, (R_V^2)', \tag{4.45}$$

$$r_E^2 = -\frac{3}{4m_N^2} - 3\, \frac{(R_V^0)''}{R_V^0}, \tag{4.46}$$

where we average over equivalent vector components and directions

$$\begin{aligned} (R_V^2)' &= \frac{1}{2}(\partial_1 R_V^2 - \partial_2 R_V^1), \\ (R_V^0)'' &= \frac{1}{3}(\partial_1^2 R_V^0 + \partial_2^2 R_V^0 \ + \partial_3^2 R_V^0). \end{aligned} \tag{4.47}$$

The squared axial radius r_A^2 and $G_P(0)$ can be evaluated using Eq. (4.41) and Eq. (4.42) as follows

$$r_A^2 = -\frac{3}{4m_N^2} - \frac{3}{2}\frac{\partial_1^2 R_A^3 + \partial_2^2 R_A^3}{R_A^3}, \tag{4.48}$$

$$G_P(0) = m_N^2 \left(\partial_1^2 R_A^3 + \partial_2^2 R_A^3 - 2\partial_3^2 R_A^3\right). \tag{4.49}$$

To estimate the excited-state effects contributing to the momentum derivatives of the ratio, we take the momentum derivatives of the leading contributions in Eq. (2.48), which lead to

$$\left. \frac{\partial R}{\partial p_i} \right|_{\vec{p}=0} \sim e^{-\Delta E_{10} T/2}, \qquad \left. \frac{\partial^2 R}{\partial p_i^2} \right|_{\vec{p}=0} \sim T e^{-\Delta E_{10} T/2}. \tag{4.50}$$

Likewise, the expected excited-state effects in applying the summation method to the

momentum derivatives of ratios are given by

$$\frac{\partial S}{\partial p_i}\Big|_{\vec{p}=0} \sim T e^{-\Delta E_{10} T}, \qquad \frac{\partial^2 S}{\partial p_i^2}\Big|_{\vec{p}=0} \sim T^2 e^{-\Delta E_{10} T}. \tag{4.51}$$

Mixed derivation with respect to $\vec{p}$ and $\vec{p}'$

The mixed-derivative approach involves the computation of the mixed-momentum derivatives of three point functions, that are first-order momentum derivatives with respect to both initial- and final-state momenta, for the extraction of the nucleon radii. In this section, we demonstrate this variation of the derivative method in detail and show the way to compute the different observables we are interested in. In this approach, there is no need to compute the momentum derivatives of the two-point function and only the first-order momentum derivatives of the three-point functions are required.

In the case of having $\vec{p}' \neq 0$, the ground-state contributions to the three-point function become

$$C_3^X(\vec{p},\vec{p}',\tau,T) = \frac{Z(\vec{p})Z(\vec{p}')}{4E(\vec{p})E(\vec{p}')} e^{-E(\vec{p})\tau} e^{-E(\vec{p}')(T-\tau)} \operatorname{Tr}\left[\Gamma_{\rm pol}(m_N + \not{p}')\mathcal{F}_X[\vec{p}',\vec{p}](m_N + \not{p})\right]. \tag{4.52}$$

As mentioned earlier in Sec. 4.1.4, the first-order momentum-derivatives of Z and E vanish at zero momentum as a consequence of the parity symmetry. Therefore, we have for the case of vector current with $\Gamma = \gamma^\mu$

$$\frac{\partial}{\partial p'^j}\frac{\partial}{\partial p^k} C_3^{V,\mu}(\vec{p},\vec{p}',\tau,T)\Big|_{\vec{p}'=\vec{p}=0} = \frac{Z^2}{2m_N^2} e^{-m_N T} \frac{\partial}{\partial p'^j}\frac{\partial}{\partial p^k} \operatorname{Tr}\left[\Gamma_{\rm pol}(m_N + \not{p}')\left(F_1\gamma_\mu + F_2\frac{i\sigma^{\mu\nu}(p'_\nu - p_\nu)}{2m_N}\right)(m_N + \not{p})\right]\Big|_{\vec{p}'=\vec{p}=0}. \tag{4.53}$$

The form factors depend only on

$$Q^2 = -q^2 = -(p'-p)^2 = -(m_N^2 - 2p'.p + m_N^2). \tag{4.54}$$

The first-order derivatives of F_1 and F_2 vanish at zero momentum and using the fact that the first-order derivatives of the energies $p_0 = E(\vec{p})$ and $p_0' = E(\vec{p}')$ vanish at zero momentum, we get

$$\begin{aligned}\frac{\partial}{\partial p'^j}\frac{\partial}{\partial p^k}C_3^{V,\mu}(\vec{p},\vec{p}',\tau,T)\bigg|_{\vec{p}'=\vec{p}=0} =& \frac{Z^2}{2m_N^2}e^{-m_N T}\times\Bigg\{F_1\,\mathrm{Tr}\left[\Gamma_{\mathrm{pol}}\gamma_j\gamma^\mu\gamma^k\right] \\ &+\left(\frac{\partial}{\partial p'^j}\frac{\partial}{\partial p^k}F_1\bigg|_{\vec{p}'=\vec{p}=0}\right)\mathrm{Tr}\left[\Gamma_{\mathrm{pol}}4m_N^2\gamma^\mu\right] \\ &+F_2\,\mathrm{Tr}\left[\Gamma_{\mathrm{pol}}(i\sigma_j^\mu\gamma^k-\gamma^j i\sigma_k^\mu)\right]\Bigg\}. \end{aligned} \tag{4.55}$$

We note that

$$\begin{aligned}\frac{\partial}{\partial p'^j}\frac{\partial}{\partial p^k}F_1\bigg|_{\vec{p}'=\vec{p}=0} &= \frac{\partial^2 Q^2}{\partial p'^j\partial p^k}\bigg|_{\vec{p}'=\vec{p}=0}\frac{dF_1}{dQ^2}\bigg|_{Q^2=0} \\ &= \left(\frac{\partial}{\partial p'^j}\frac{\partial}{\partial p^k}2g_{\mu\nu}p'^\mu p^\nu\right)\bigg|_{\vec{p}'=\vec{p}=0}\frac{dF_1}{dQ^2}\bigg|_{Q^2=0} \\ &= 2g_{jk}\frac{dF_1}{dQ^2}\bigg|_{Q^2=0} \\ &= -\frac{1}{3}g_{jk}F_1\left[r_1\right]^2. \end{aligned} \tag{4.56}$$

In summary, we have

$$\begin{aligned}\frac{\partial}{\partial p'^j}\frac{\partial}{\partial p^k}C_3^{V,\mu}(\vec{p},\vec{p}',\tau,T)\bigg|_{\vec{p}'=\vec{p}=0} = \frac{Z^2}{4m_N^2}e^{-m_N.T}\times\Bigg\{&F_1\,\mathrm{Tr}[\Gamma_{\mathrm{pol}}\gamma^j\gamma_\mu\gamma^k] \\ &-\frac{4}{3}F_1m_N^2[r_1]^2g_{jk}\,\mathrm{Tr}[\Gamma_{\mathrm{pol}}\gamma^\mu] \\ &F_2\,\mathrm{Tr}\left[\Gamma_{\mathrm{pol}}(i\sigma_j^\mu\gamma^k-\gamma^j i\sigma_k^\mu)\right]\Bigg\}. \end{aligned} \tag{4.57}$$

By building the ratios of the two- and three-point functions, the exponential and

overlap factors can be canceled. We define

$$R_V(\mu, j, k) = \frac{\frac{\partial}{\partial p'^j}\frac{\partial}{\partial p^k} C_3^{V,\mu}(\vec{p}, \vec{p}', \tau, T)\Big|_{\vec{p}'=\vec{p}=0}}{C_2(\vec{0}, T)}. \tag{4.58}$$

We find nonzero results for the following combination of μ, j and k

$$R_V(0, 1, 2) = \frac{i}{4m_N^2}\left[2\mu - 1\right], \tag{4.59}$$

$$R_V(0, j, j) = \frac{1}{4m_N^2} + \frac{1}{3}r_E^2, \tag{4.60}$$

from which we can compute

$$\mu = -2im_N^2 R_V(0, 1, 2) + \frac{1}{2}, \tag{4.61}$$

$$r_E^2 = 3\left(R_V(0, j, j) - \frac{1}{4m_N^2}\right). \tag{4.62}$$

Similarly, we can apply this method to the axial current where $\Gamma = \gamma^\mu\gamma_5$ and extract the axial radius. We start by looking at the mixed-momentum derivatives of the three-point function in this case which we find to be

$$\begin{aligned}\frac{\partial}{\partial p'^j}\frac{\partial}{\partial p^k} C_3^{A,\mu}(\vec{p}, \vec{p}', \tau, T)\Big|_{\vec{p}'=\vec{p}=0} = \frac{Z^2}{4m_N^2} e^{-m_N.T} \times \Bigg\{ & G_A \,\mathrm{Tr}[\Gamma_{\mathrm{pol}}\gamma^j\gamma_\mu\gamma_5\gamma^k] \\ & - \frac{4}{3}G_A m_N^2 r_A^2 g_{jk}\,\mathrm{Tr}[\Gamma_{\mathrm{pol}}\gamma^\mu\gamma_5] \\ & G_P\,\mathrm{Tr}\left[\Gamma_{\mathrm{pol}}\gamma_5(\delta_k^\mu\gamma^j - \delta_j^\mu\gamma^k)\right] \Bigg\}.\end{aligned} \tag{4.63}$$

Building the ratios in the same way as we did for the vector current, we obtain for

the axial current

$$R_A(1,1,3) = R_A(1,3,1) = R_A(2,2,3) = R_A(2,3,2) = \frac{1}{4m_N^2}\left[G_A(0) - G_P(0)\right], \tag{4.64}$$

$$R_A(1,3,2) = R_A(2,1,3) = R_A(3,2,1) = \frac{i}{4m_N^2}G_A(0), \tag{4.65}$$

$$R_A(1,2,3) = R_A(2,3,1) = R_A(3,1,2) = -\frac{i}{4m_N^2}G_A(0), \tag{4.66}$$

$$R_A(3,1,1) = R_A(3,2,2) = G_A(0)\left(-\frac{1}{4m_N^2} + \frac{1}{3}r_A^2\right), \tag{4.67}$$

$$R_A(3,3,3) = \frac{1}{12m_N^2}\left[3G_A(0) - 6G_P(0) + 4m_N^2 G_A(0) r_A^2\right]. \tag{4.68}$$

From those relations, we can derive the following

$$G_A(0) = 4m_N^2 R_{\text{av}}^{(1)}, \tag{4.69}$$

$$G_P(0) = G_A(0) - 4m_N^2 R_{\text{av}}^{(2)}, \tag{4.70}$$

$$r_A^2 = \frac{R_{\text{av}}^{(3)}}{G_A(0)} + \frac{1}{4m_N^2} + \frac{G_P(0)}{2m_N^2 G_A(0)}, \tag{4.71}$$

where we define

$$R_{\text{av}}^{(1)} = \frac{1}{6}\left[R_A(1,3,2) + R_A(2,1,3) + R_A(3,2,1) - R_A(1,2,3) - R_A(2,3,1) - R_A(3,1,2)\right], \tag{4.72}$$

$$R_{\text{av}}^{(2)} = \frac{1}{4}\left[R_A(1,1,3) + R_A(1,3,1) + R_A(2,2,3) + R_A(2,3,2)\right], \tag{4.73}$$

$$R_{\text{av}}^{(3)} = R_A(3,1,1) + R_A(3,2,2) + R_A(3,3,3). \tag{4.74}$$

4.2 Results

We perform our lattice calculations using the two physical point ensembles described in Sec. 3.1.2. In Sec. 4.2.1, we show our earlier results for the form factors evaluated at $Q^2 = 0$ and the charge and axial radii which were obtained from the fine ensemble. In these calculations, we used the first variation of the derivative approach — momentum derivation with respect to the initial-state momenta — and compared the obtained results to their estimations from the traditional approach. In addition, in

Sec. 4.2.2, we present calculations of the nucleon form factors and radii performed on the coarse ensemble using both variations of the derivative method together with the conventional approach. In all calculations, we measure the isovector combination $u - d$ of the three-point functions, where the disconnected contributions cancel out. The axial current is renormalized using Z_A from Tab. 3.8 and the vector current by imposing $G_E^v(0) = 1$. For removing contributions from excited states, we use the summation method.

4.2.1 Results from the fine ensemble

Derivatives of the two-point functions

We begin by testing our method applied to the simpler case of two-point functions. From Eq. (2.17), the ground-state contribution is

$$C_2(\vec{p}, t) = \frac{Z(\vec{p})^2 \left(E(\vec{p}) + m_N\right)}{E(\vec{p})} e^{-E(\vec{p})t}. \tag{4.75}$$

The momentum derivatives of $C_2(\vec{p}, t)$ can then be evaluated at $\vec{p} = 0$ and we obtain

$$C_2(0, t) = 2Z^2 e^{-m_N t}, \tag{4.76}$$

$$C_2'(0, t) = 4ZZ' e^{-m_N t}, \tag{4.77}$$

$$C_2''(0, t) = \frac{1}{m_N^2}\left[-(1 + 2m_N t)Z^2 + 4m_N^2 (Z')^2 + 4m_N^2 ZZ''\right] e^{-m_N t}, \tag{4.78}$$

where $Z \equiv Z(0)$. We expect $C_2'(0, t)$ to vanish due to parity symmetry and our numerical results shown in the left part of Fig. 4-2 confirm that, which allows us to set $Z'(0) = 0$ in Eq. (4.78). We apply a combined 1-state fit for $C_2(0, t)$ and $C_2''(0, t)^{\Lambda,\Sigma}$ using Eq. (4.76) and Eq. (4.78) with Z, Z'' and m being the fit parameters. The results of these fits are shown in Fig. 4-2, where the slight differences between the momentum derivatives of Σ_r and Λ_r two-point functions give an indication of the systematic errors associated with the derivative method and motivate the approach described in Sec. 4.1.2 for isolating $\Sigma_r \to N$ from $\Lambda_r \to N$ three point functions when

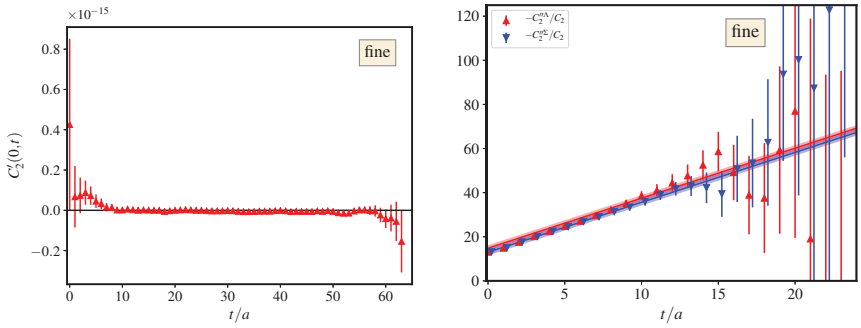

Figure 4-2: $C_2'(0,t)$ (left) and $-C_2''(0,t)^{\Lambda,\Sigma}/C_2(0,t)$ (right) from fine ensemble. The red and blue bands correspond to the combined fits of $C_2''(0,t)^{\Lambda,\Sigma}$ and $C_2(0,t)$.

Method	$Z(0) \times 10^7$	$Z''(0) \times 10^7$
Fit $C_2(0,t)$ and $C_2''(0,t)^{\Lambda}$	1.633(14)	−9.9(1.1)
Fit $C_2(0,t)$ and $C_2''(0,t)^{\Sigma}$	1.635(15)	−8.9(1.2)
Fit $Z(\vec{p}^2)$	1.521(70)	−9.6(1.8)

Table 4.1: Resulting values for $Z(0)$ and $Z''(0)$ on the fine ensemble using either the combined fit of $C_2(0,t)$ and $C_2''(0,t)^{\Lambda,\Sigma}$ or the fit to $Z(\vec{p}^2)$.

extracting the momentum derivatives of the matrix elements.

We also try another approach for extracting $Z(0)$ and $Z''(0)$ where we apply two-state fits to $C_2(\vec{p},t)$ for different discrete values of $\vec{p}^2$ which allows us to extract $Z(\vec{p}^2)$. The extracted values for $Z(\vec{p}^2)$ are consistent with a linear dependence on $(a\vec{p})^2$. By applying a linear fit to $Z(\vec{p}^2)$ against $\vec{p}^2$, $Z(0)$ can be obtained from the intercept and $Z''(0)$ from the slope as $Z''(0) = 2\frac{\partial Z(\vec{p}^2)}{\partial \vec{p}^2}$. This is shown in Fig. 4-3.

Table 4.1 reports a comparison between the extracted values for $Z(0)$ and $Z''(0)$ using the two different approaches and when using $[C_2''(0,t)]^{\Sigma}$ and $[C_2''(0,t)]^{\Lambda}$ in the combined fit. All fit methods lead to consistent values for both $Z(0)$ and $Z''(0)$.

Electromagnetic form factors

The "plateau plots" in Fig. 4-4 show $G_M^v(0)$ estimated on the fine ensemble using the first-order momentum derivative with respect to $\vec{p}$ in Eq. (4.45) (left) and $(r_E^2)^v/a^2$

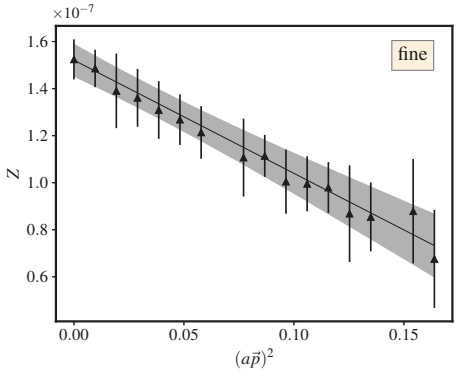

Figure 4-3: The derived values for $Z(\vec{p}^2)$ on the fine ensemble from two-state fits of $C_2(\vec{p}, t)$ (black points) followed by a linear fit (grey band) for extracting $Z(0)$ and $Z''(0)$.

obtained from the second-order momentum derivative with respect to $\vec{p}$ in Eq. (4.46) (right). In each case, we show results from both the ratio method and the summation method. $G_M^v(0)$ increases for increased source-sink separations, indicating that the excited-state contributions are significant in this case. The relative statistical uncertainty is much larger for $(r_E^2)^v/a^2$, and therefore we are unable to resolve any significant excited-state effects.

Figure 4-5 shows a comparison between our results using the first variation of the derivative method and the traditional approach for both the isovector magnetic moment $\mu^v = G_M^v(0)$ (bottom row) and the isovector charge radius $(r_E^2)^v$ (top row). In Fig 4-5, we present the results extracted using both the ratio method with the smallest source-sink separation $T/a = 10$ and the summation method. When going to the summation method, $G_E^v(Q^2)$ decreases significantly whereas $G_M^v(Q^2)$ increases (especially for small Q^2) towards the corresponding phenomenological curve from Kelly [84]. This shows the non-trivial contribution from excited states associated with the ratio method using $T/a = 10$. The summation points for $G_E^v(Q^2)$ lie slightly above the corresponding Kelly curve while those for $G_M^v(Q^2)$ show a good agreement with the Kelly curve. The derivative method's results for both $G_M^v(0)$ and $(r_E^2)^v$ using the summation method are consistent with both the traditional method's results and

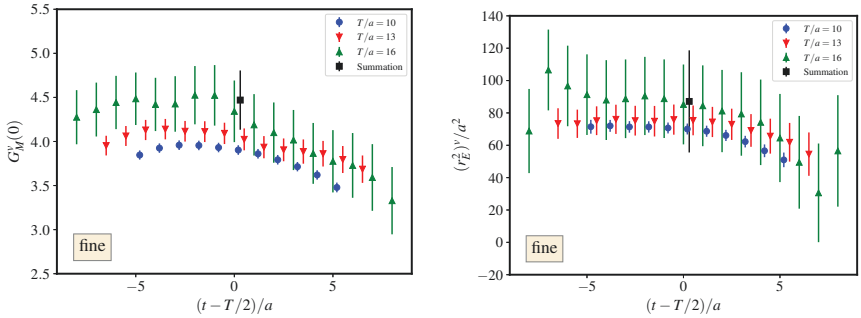

Figure 4-4: Isovector magnetic moment (left) and isovector charge radius (right) evaluated on the fine ensemble using the momentum derivatives with respect to the initial-momentum state. For both μ^v and $(r_E^2)^v/a^2$, results from the ratio method are shown using source-sink separations $T/a \in \{10, 13, 16\}$, as well as the summation method.

the experiment but with statistical errors roughly twice as large as the traditional approach for the isovector magnetic moment and three times as large for the isovector charge radius.

Axial form factors

The left-hand side of Fig. 4-6 shows the isovector induced pseudoscalar form factor $G_P^v(0)$ extracted from the fine ensemble using the second derivative with respect to $\vec{p}$ in Eq. (4.49). The right-hand side of the same figure shows the extracted r_A^2 using Eq. (4.48). Figure 4-6 shows the plateau plots for both quantities corresponding to the three available source-sink separations in addition to the summation points. For $G_P^v(0)$, we see a large increase with the source-sink separation, indicating substantial excited-state effects, and that leads us to conclude that the summation point may not be free from excited-state effects. For r_A^2, the statistical errors are too large to detect any excited-state effects.

A comparison between our results using the second derivatives with respect to the initial-state momenta and the traditional method for both r_A^2 and $G_P^v(0)$ is shown in Fig. 4-7, top and bottom row, respectively. Shown are results from both the ratio method with $T/a = 10$ and the summation method. Both $G_A^v(Q^2)$ and $G_P^v(Q^2)$

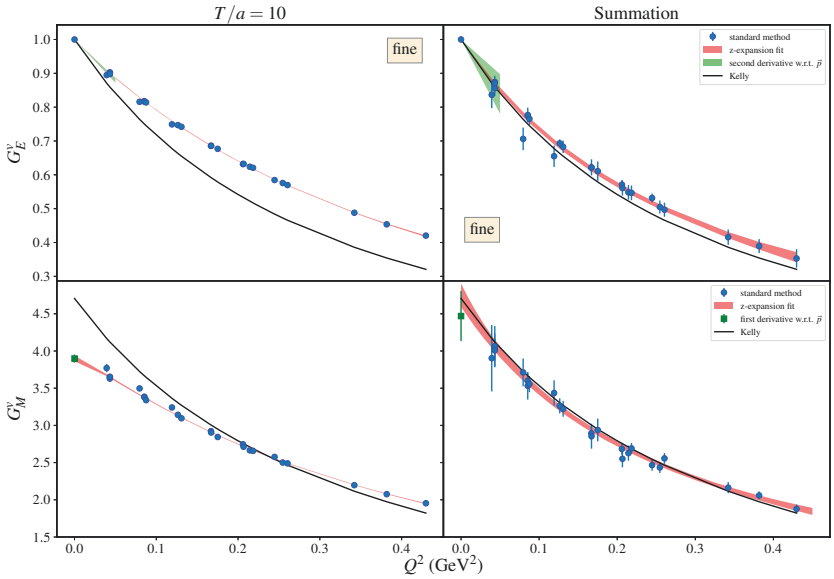

Figure 4-5: Isovector electric (top row) and magnetic (bottom row) form factors from the fine ensemble using both the ratio method with $T = 10\ a$ (left column) and the summation method (right column). The blue points show results from the standard method and the red bands show a z-expansion fit to those points. The green band (top) and point (bottom) show the slope and value of the respective form factor at $Q^2 = 0$, computed using the second- and first-momentum derivatives with respect to $\vec{p}$, respectively. The black curves result from a phenomenological fit to experimental data by Kelly [84].

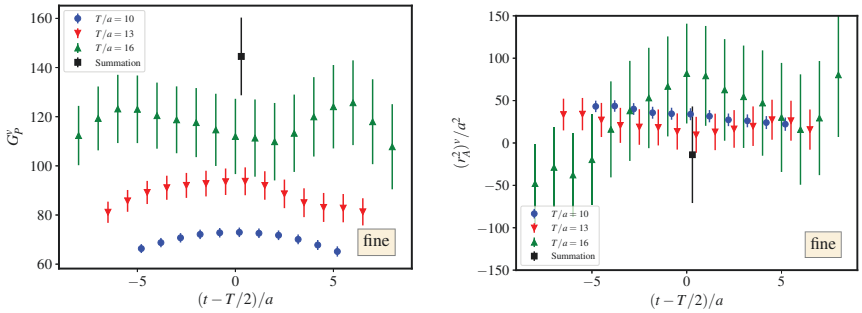

Figure 4-6: The induced pseudoscalar form factor at $Q^2 = 0$ (left) and nucleon axial radius (right) using the second momentum derivatives with respect to $\vec{p}$. For both $G_P(0)$ and r_A^2/a^2, results from ratio method are shown using source-sink separations $T/a \in \{10, 13, 16\}$, as well as the summation method.

increase when going to the summation method indicating the significant excited-state contributions for the ratio method with $T/a = 10$. The extracted value for the axial radius using the derivative method has a much larger statistical error compared to its value from the traditional approach. For G_P^v in Fig. 4-7, before fitting we remove the pion pole that is present in the form factor, and then restore it in the final fit curve as was discussed in Sec. 2.5.2. At $T/a = 10$, there is a significant disagreement between $G_P(0)$ from the traditional and the derivative approaches which is likely due to excited-state effects. The value for $G_P^v(0)$ using the summation method and the derivative approach seems to be in good agreement with its value from the traditional approach despite the large extrapolation caused by the inclusion of the pion pole in the fit. However, $G_P^v(0)$ obtained from momentum derivative with respect to the initial momenta has statistical uncertainties roughly twice as large as the traditional approach.

4.2.2 Results from the coarse ensemble

Electromagnetic form factors

Figure 4-8 shows a comparison between the obtained plateaus for $G_M^v(0)$ using the first derivative with respect to $\vec{p}$ using Eq. (4.45) (left) and the mixed-derivative with

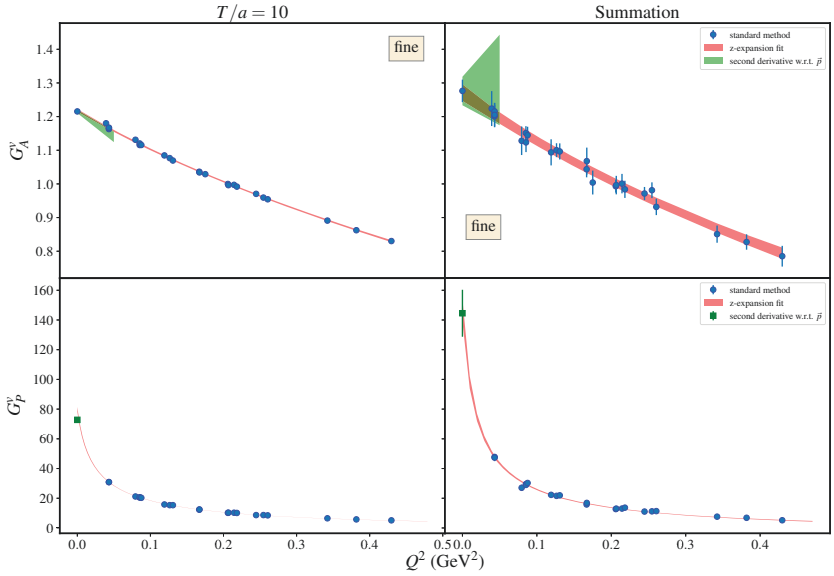

Figure 4-7: Nucleon axial (top row) and induced pseudoscalar (bottom row) form factors on the fine ensemble using both the ratio method for $T = 10\ a$ (left column) and the summation method (right column). The blue points show results from the standard method and the red bands show a z-expansion fit to those points. The green band (top) and point (bottom) show the slope and value of the respective form factor at $Q^2 = 0$, computed using the second momentum derivatives with respect to the initial-state momenta.

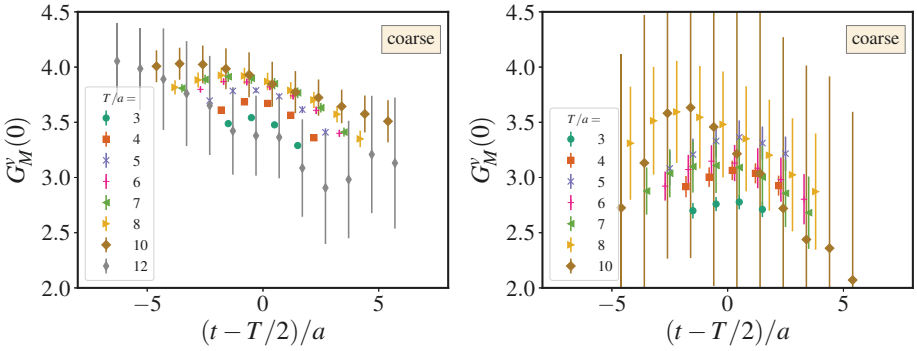

Figure 4-8: A comparison between the obtained plateaus for $G_M^v(0)$ using the first-derivative approach (left) and the mixed-derivative one (right) on the coarse ensemble. The different source-sink separations are displayed in different colors.

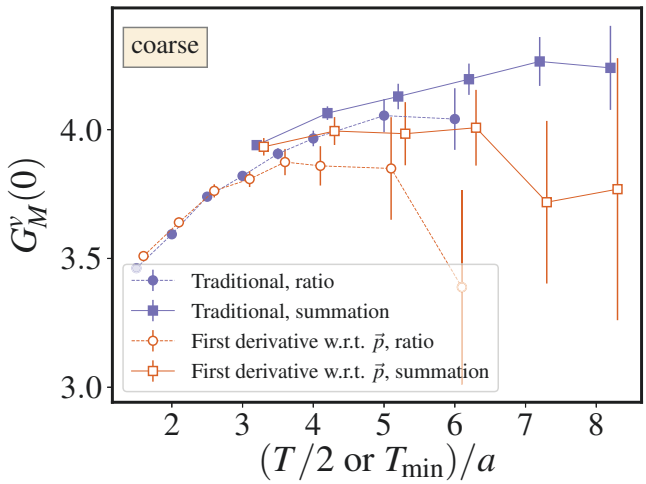

Figure 4-9: A summary of the obtained values of $G_M^v(0)$ on the coarse ensemble using the ratio method (circles) and its values from the summation method (squares). Here, we compare between the conventional method (solid green symbols) and the second-derivative method (empty red symbols).

respect to $\vec{p}$ and $\vec{p}'$ (right) using Eq. (4.61). We find that the derived values for $G_M^v(0)$ using the mixed-derivative approach are much noisier. Because of this effect, we prefer to concentrate on $G_M^v(0)$ obtained using Eq. (4.45) in the following summary plot. In Fig. 4-9, we compare the derived values for $G_M^v(0)$ from first derivative with respect to $\vec{p}$ to the obtained values from the conventional method. We give a summary plot containing the resulting $G_M^v(0)$ values using both approaches from both the ratio (all T values) and the summation methods where we fix the maximum T included in the fit to the largest available value $T_{\text{max}}/a = 12$ and change the minimal T included in that fit, T_{min}. $G_M^v(0)$ values from the conventional approach reach a plateau as expected for both the ratio and summation points. This we also observe in the case of the first momentum derivative approach but with 2 to 3 times larger error bars.

In Fig. 4-10, we compare between the resulting plateaus for $(r_E^v/a)^2$ using the second-derivative approach in Eq. (4.46) (left) and the mixed-derivative approach using Eq. (4.62) (right). We observe a significant reduction in the noise and smoother

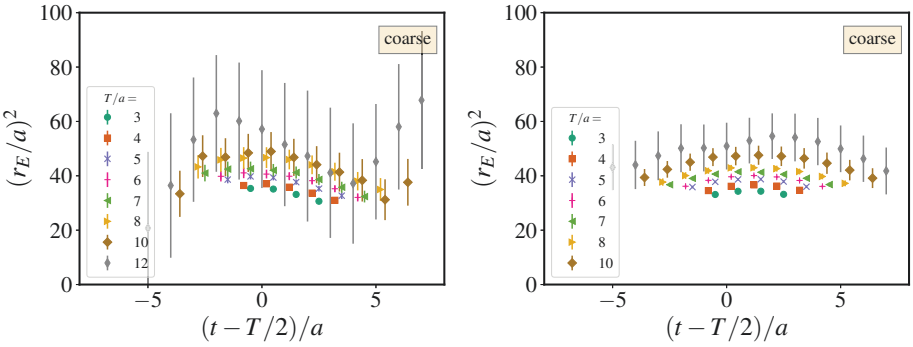

Figure 4-10: A comparison between the obtained plateaus on the coarse ensemble for $(r_E^v/a)^2$ using the second-derivative approach (left) and the mixed-derivative approach (right).

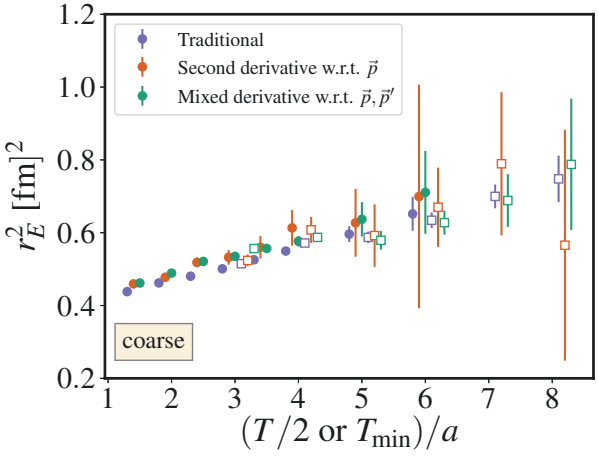

Figure 4-11: A summary of the obtained values of $(r_E^v)^2$ on the coarse ensemble using the ratio method (solid circles) and its values from the summation method (empty squares). Here, we compare between the conventional method (blue symbols), the second-derivative method (red symbols) and the mixed-derivative method (green symbols).

plateaus in the case of the mixed-derivative method. Figure 4-11 shows a summary of our results for $(r_E^v)^2$ using all three approaches (conventional and both derivative methods). In this plot, we include results using the ratio and summation methods. The charge radius is consistent among all three approaches and also among the ratio and summations points. This summary plot shows the efficiency of the mixed-derivative approach in reducing the noise where we are able to reduce the statistical uncertainties to less than half when compared to the second-derivative approach. However, the charge radius obtained from the mixed-derivative approach is still 2-3 times larger than its value from the conventional approach. In addition, we notice significant excited-state contamination for both derivative approaches.

In Fig. 4-12, we show a comparison between the resulting $G_E^v(Q^2)$ (top row) and $G_M^v(0)$ (bottom row) from the traditional method and both derivative methods. The left and right columns of Fig. 4-12 show how those observables vary when going from $T/a = 8$, which is closest to what we had for the fine ensemble, to the summation point which here corresponds to $T_{\min}/a = 8$. Going from $T/a = 8$ to the summation shows that the excited-state contaminations are significant in both cases of $G_E(Q^2)$ and $G_M(Q^2)$. When approaching summation method, $G_E(Q^2)$ decreases significantly towards the phenomenological Kelly curve which shows the non-trivial contamination to the ratio method for $T/a = 8$. The resulting $G_E(Q^2)$ from the summation method still lies slightly above the Kelly curve. We observe a better agreement between the Kelly curve and the summation points for the case of $G_M(Q^2)$ where the resulting points increase from $T/a = 8$ to the summation points toward their phenomenologically estimated values showing again the significance of the excited-state contamination for this observable.

Axial form factors

Figure 4-13 shows the resulting $G_P^v(0)$ plateaus on the coarse ensemble using the second-derivative approach, Eq. (4.49), (left) and mixed-derivative one, Eq. (4.70), (right). We notice a significant reduction in the noise when using the latter approach. Furthermore, the mid-points of the plateaus increase with increasing the source-sink

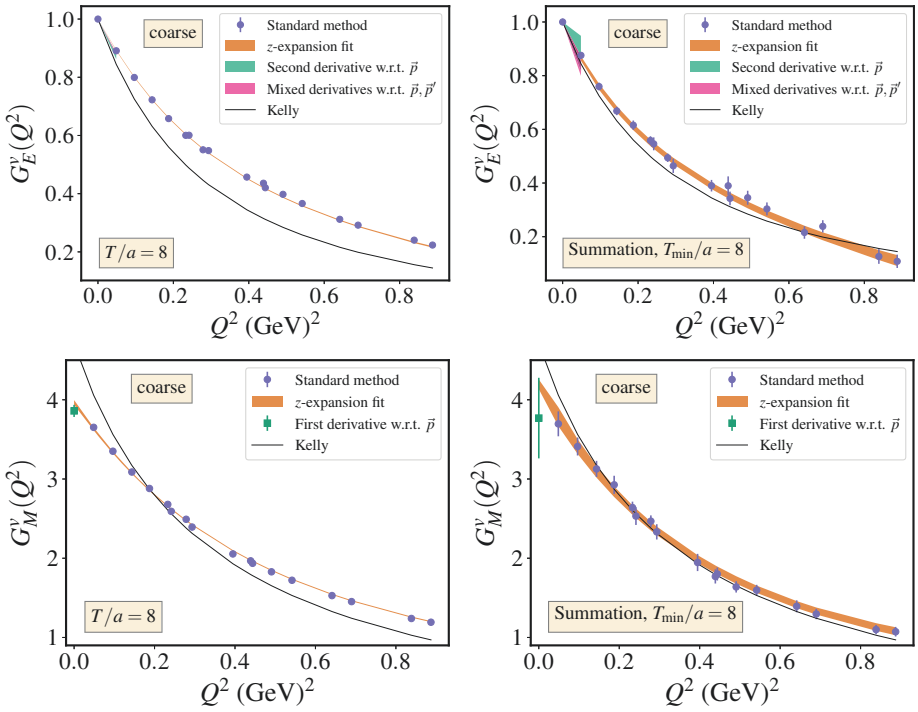

Figure 4-12: Isovector electric (top row) and magnetic (bottom row) form factors using both the ratio method with the source-sink separation $T/a = 8$ (left column) and the summation method with $T_{\text{min}}/a = 8$ (right column). The blue points show results from the conventional method and the red bands show a z-expansion fit to those points. The green band (top) and point (bottom) show the slope and value of the respective form factors at $Q^2 = 0$ computed using the second- and first-derivative with respect to $\vec{p}$, respectively. The magenta band (top) refers to the resulting electric form factor when evaluated using the mixed-derivative method. The black curves result from a phenomenological fit to experimental data by Kelly [84].

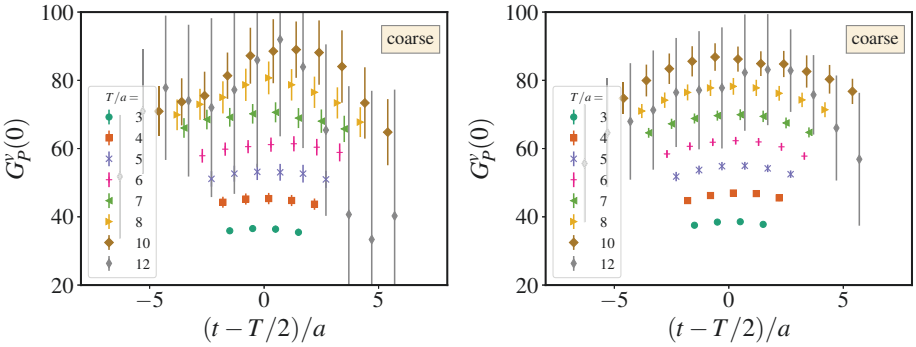

Figure 4-13: A comparison between the obtained plateaus for $G_P^v(0)$ on the coarse ensemble using the second-derivative approach (left) and the mixed-derivative approach (right).

separation in both approaches indicating the considerable excited-state contamination for this observable.

Figure 4-14 contains the resulting $G_P^v(0)$ from both derivative methods plotted against $T/2$ (ratio points) and T_{min}/a (summation points). This plot shows a significant discrepancy between the obtained $G_P^v(0)$ from the traditional method and from the momentum derivative approaches. This discrepancy could be caused by the different excited-state contributions for those methods. We notice a continuous increase of $G_P^v(0)$ with T or T_{min} for all three approaches (unless for $T_{\text{min}}/a = 8$ points from the derivative approaches) which indicates the significant excited-state contaminations for that observable which may not be in control using the ratio and summation analysis methods. The two derivative approaches are consistent within error bars and the mixed-derivative approach leads to uncertainties almost half the size of the uncertainties resulting from the second-derivative approach.

Figure 4-15 shows a comparison between the obtained plateaus for $(r_A^v)^2$ using the second-derivative approach (left) and the mixed-derivative approach (right). It shows how the mixed-derivative method effectively reduces the noise in the signal for $(r_A^v)^2$. Figure 4-16 shows a summary of the estimated squared axial radius on the coarse ensemble using the ratio and summation methods. In this plot we compare between

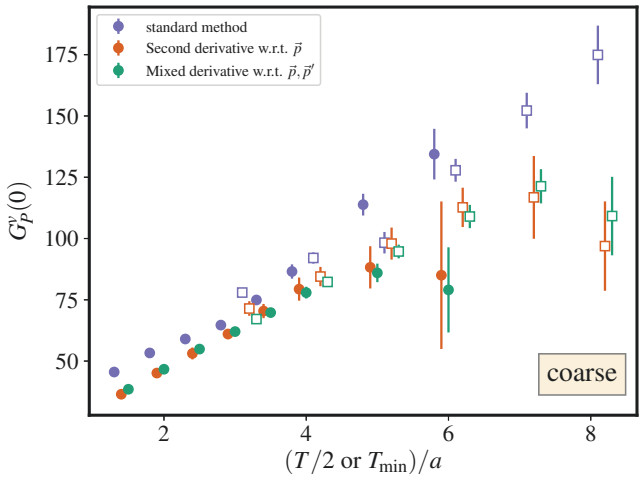

Figure 4-14: A summary of the obtained values of $G_P^v(0)$ on the coarse ensemble. The rest is the same as in Fig. 4-11

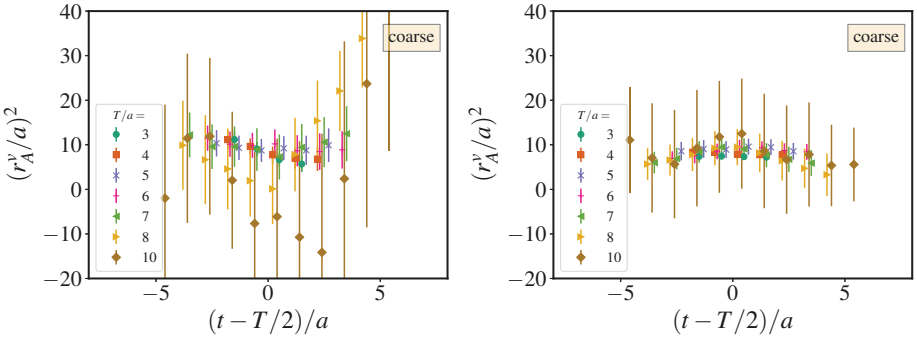

Figure 4-15: A comparison between the resulting plateaus for $(r_A^v)^2$ on the coarse ensemble using the second-derivative approach (left) and the mixed-derivative approach (right).

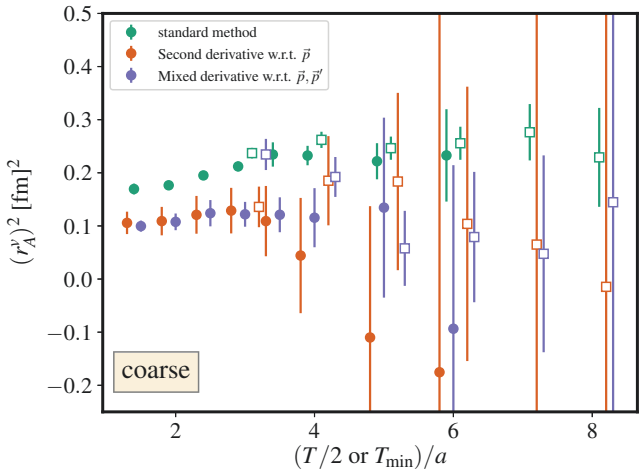

Figure 4-16: A summary of the obtained values of $(r_A^v)^2$ on the coarse ensemble. The rest is the same as in Fig. 4-11

the conventional approach and the two derivative approaches. We notice a discrepancy between the traditional approach and both derivative approaches for small T and T_{min}. For large T and T_{min}, this discrepancy tends to decrease and the statistical noise from the derivative approaches grows. We obtain the smallest statistical uncertainties using the conventional method. The mixed-derivative approach succeeds in reducing the statistical uncertainties when compared to the second-derivative method; the obtained errors using that approach are still 2-3 times larger than the ones obtained using the conventional approach. Figure 4-17 shows $G_A^v(Q^2)$ and $G_P^v(Q^2)$ from the traditional method and their values at $Q^2 = 0$ extracted with the z expansion in addition to a comparison to the derived values from both derivative methods. The left column shows our evaluations for the source-sink separation, $T = 8a$ and we show the estimated values from the summation method with $T_{\mathrm{min}} = 8a$ and $T_{\mathrm{max}} = 12a$ in the right column. Both $G_A^v(Q^2)$ and $G_P^v(Q^2)$ increase when going from $T = 8a$ to the summation results indicating the effects of the excited-state contaminations at $T = 8a$.

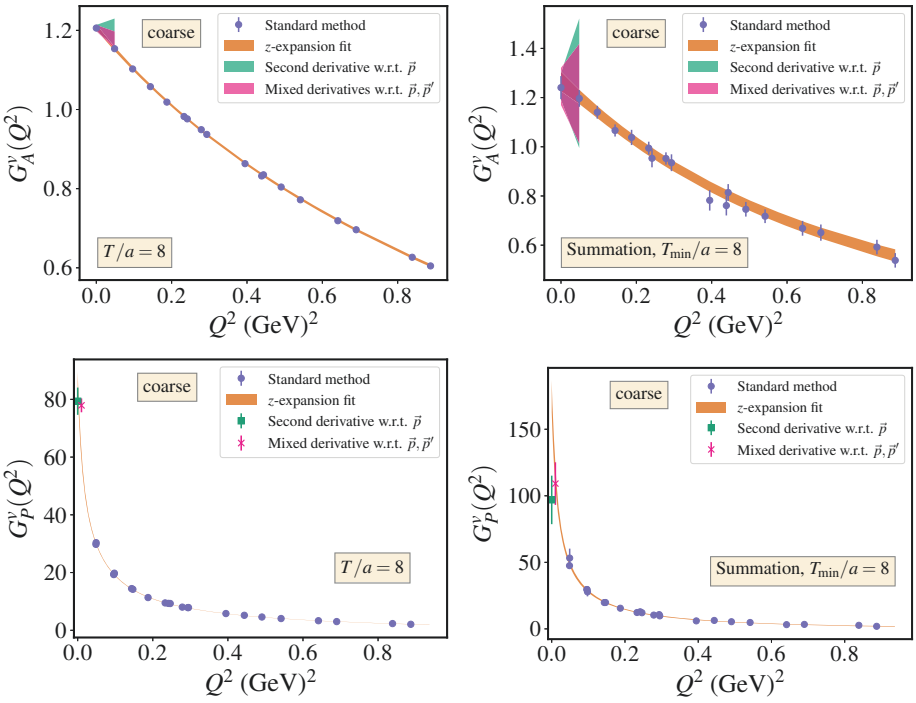

Figure 4-17: Nucleon axial (top row) and induced pseudoscalar (bottom row) form factors on the coarse ensemble using both the ratio method for $T = 8\ a$ (left column) and the summation method (right column). The blue points show results from the standard method and the red bands show a z-expansion fit to those points. The green and magenta bands (top) and points (bottom) show the slope and value of the respective form factor at $Q^2 = 0$, computed using the second-derivative and the mixed-derivative methods,respectively.

4.2.3 Numerical results

In this section, we report our numerical results for the form factors at $Q^2 = 0$ and the nucleon radii obtained on both the fine and coarse ensembles using the traditional method and the two variations of the derivative method. We choose to present the estimations of our observables obtained using the summation method at $T_{\text{min}} \sim 0.9$ fm. This corresponds to $T_{\text{min}}/a = 10$ on the fine ensemble and $T_{\text{min}}/a = 8$ on the coarse one. Tables. 4.2 to 4.5 present our results for the nucleon isovector magnetic moment, charge radius, induced preudoscalar form factor at $Q^2 = 0$, and the axial radius, respectively. We observe a large inconsistency between the different methods and the two ensembles for μ^v and $G_P(0)$. Our results for μ^v on the fine ensemble are consistent with the PDG experimental value, $(\mu^v)_{\text{exp}} = 4.706$ [117], although with large statistical uncertainties especially for the derivative method result. On the coarse ensemble, our μ^v estimates are lower than the experimental value.

For the nucleon charge and axial radii, our results have more consistency although within large statistical uncertainties for those resulting from the derivative method. Compared with the CODATA world average from ep scattering, $(r_E^2)^v = 0.882(11)$ $[\text{fm}]^2$ or from muon spectroscopy $(r_E^2)^v = 0.8232(23)$ $[\text{fm}]^2$ [117], our estimated value from the traditional method on the fine ensemble is more consistent with the latter whereas the value from the coarse ensemble lies below both experimental measurements. The overlap with the experimental values enhances with the derivative methods although within larger statistical uncertainties. Compared with phenomenological estimate of the axial radius obtained using the neutrino scattering data, $(r_A^2)^v_{\text{exp}} = 0.46(22)$ $[\text{fm}]^2$ [97], our estimate using the traditional method on the fine ensemble is consistent with phenomenology. However, the estimate of the axial radius on the coarse ensemble lies well below the phenomenological one and the derivative methods's results have overlap but with much larger statistical uncertainties. For $G_P(0)$, we are not aware of any phenomenological estimates.

	μ^v	
	Traditional method	First derivative w.r.t. $\vec{p}$
Fine	4.75(15)	4.46(33)
Coarse	4.24(16)	3.77(51)

Table 4.2: Numerical results of the nucleon isovector magnetic moment evaluated on both ensembles using the traditional and momentum derivative approaches. Those results correspond to the summation points at comparable $T_{\min}/a = 10$ and $T_{\min}/a = 8$ for the fine and coarse ensemble, respectively.

	$(r_E^2)^v$ [fm]^2		
	Traditional method	Second derivative w.r.t. $\vec{p}$	Mixed derivative w.r.t. $\vec{p}, \vec{p}'$
Fine	0.787(87)	0.753(273)	-
Coarse	0.748(64)	0.57(32)	0.79(18)

Table 4.3: Numerical results of the nucleon isovector charge radius evaluated on both ensembles using the traditional and both variations of the derivative approaches. The rest is the same as in Tab. 4.2.

	$G_P(0)$		
	Traditional method	Second derivative w.r.t. $\vec{p}$	Mixed derivative w.r.t. $\vec{p}, \vec{p}'$
Fine	146(8)	145(16)	-
Coarse	174(12)	97(18)	109(16)

Table 4.4: Numerical results of the nucleon isovector induced pseudoscalar form factor at $Q^2 = 0$. The rest is the same as in Tab. 4.3

	$(r_A^2)^v$ [fm]^2		
	Traditional method	Second derivative w.r.t. $\vec{p}$	Mixed derivative w.r.t. $\vec{p}, \vec{p}'$
Fine	0.295(68)	$-0.120(492)$	-
Coarse	0.229(93)	$-0.01(80)$	0.14(50)

Table 4.5: Numerical results of the nucleon axial charge radius. The rest is the same as in Tab. 4.3

4.3 Summary and outlook

In this chapter, we presented a derivative method for computing nucleon observables at zero momentum transfer. Using this method helps to avoid the model dependence and the large extrapolation needed in the traditional approach for computing such quantities. We presented two variations of the derivative method: one which involves the computation of the first- and second-order derivatives of the correlation functions with respect to the initial-state momentum and another where for extracting the nucleon radii we need to simultaneously compute the first-order momentum derivatives of the three-point function with respect to both the initial- and final-state momenta. We applied all three methods (the conventional and the two derivative methods) to the nucleon isovector magnetic moment and electric charge radius as well as the isovector induced pseudoscalar form factor at $Q^2 = 0$ and the axial radius.

We presented calculations performed on two 2+1-flavor ensembles with a 2-HEX-smeared Wilson-clover action. Both ensembles are at the physical pion mass and have lattice spacings of 0.116 and 0.093 fm. We have demonstrated control over excited-state contamination by using eight source-sink separations in the range from roughly 0.4 to 1.4 fm on the coarse ensemble and three source-sink separations in the range from 0.9 to 1.5 fm on the fine ensemble. The shorter source-sink separations are useful for the summation method but larger ones are needed for the ratio method. Furthermore and on the fine ensemble, we perform our calculations using only the traditional approach and the first variation of the derivative method. On the coarse ensemble, however, we applied all three approaches.

For $G_M(0)$ and $G_P(0)$, there is a good agreement between the traditional and derivative approaches on the fine ensemble. This is particularly remarkable in the latter case, since the pion pole produces a very large effect in the extrapolation of $G_P(Q^2)$ to $Q^2 = 0$. On the coarse ensemble, however, both derivative approaches lead to lower values for $G_M(0)$ and $G_P(0)$ when compared to the traditional approach which indicates that the finite-volume and discretization effects are significant for those two observables. We found that using the mixed-derivative approach reduces

the statistical uncertainties on the nucleon radii and $G_P(0)$ when compared to the second-derivative approach. However, both derivative approaches suffer from large statistical uncertainties when compared to the traditional approach. The inability to control the excited states in this case makes any firm conclusion difficult.

The difference between the CODATA value of $(r_E^2)^v$ and its muonic hydrogen measurement is ~ 0.06 fm^2, so it will be a challenge to calculate the charge radius with a total uncertainty significantly less than that. Our quoted errors are statistical and in order to have reliable calculations, we need to estimate and improve the control over systematic uncertainties. These include a more careful study of the excited-state contaminations and effects of discretization.

Chapter 5

Up, down, and strange nucleon axial form factors

In addition to the valence up and down quarks, quantum fluctuations cause other quarks to play a role in the structure of nucleons; the strange quark is the next lightest, and is expected to be the next most important. In this chapter, we report a calculation of the nucleon axial form factors using a single lattice QCD ensemble. This calculation includes both quark-connected and disconnected diagrams, which allows us to determine the up, down, and strange form factors. Using the same dataset, a high-precision calculation of the strange nucleon electromagnetic form factors was previously reported by our group [65]. This chapter is based on our published work in Ref. [66] and is organized as follows. Section 5.1 describes our methodology: the approaches used to isolate the nucleon ground state and determine the form factors and the numerically-challenging disconnected diagrams, the details of the lattice ensemble, and the fits to the Q^2-dependence of the form factors using the z expansion. The unwanted contributions from excited states to the different observables are examined in detail, and the estimation of systematic uncertainty is described. Our nonperturbative calculation of the renormalization factors, including a nonperturbative treatment of the flavor singlet case, is presented in Sec. 5.2. The main results are in Sec. 5.3: the axial and induced pseudoscalar form factors for light and strange quarks, as well as the quark contributions to the nucleon spin. Finally, we present

our conclusions in Sec. 5.4.

5.1 Lattice methodology

5.1.1 Lattice ensemble and calculation setup

We use a single lattice ensemble with a tree-level Symanzik improved gauge action ($\beta = 6.1$) and 2+1 flavors of clover-improved Wilson fermions that couple to the gauge links after stout smearing (one step with $\rho = 0.125$). The improvement parameters are set to their tadpole-improved tree-level values. The lattice size is $32^3 \times 96$ and the bare quark masses are $am_s = -0.245$ and $am_{ud} = -0.285$.

Based on the $\Upsilon(2S) - \Upsilon(1S)$ energy splitting computed using lattice NRQCD, the lattice spacing is $a = 0.11403(77)$ fm. The strange quark mass is close to its physical value: the mass of the unphysical η_s meson is $672(3)(5)$ MeV, which is within 5% of its value determined for physical quark masses [47]. The light quark mass is heavier than physical, producing a pion mass[1] of $317(2)(2)$ MeV. The volume is quite large, such that $m_\pi L_s \approx 5.9$, and we thus expect finite-volume effects to be highly suppressed.

We performed calculations using 1028 gauge configurations, on each of which we chose six equally-spaced source timeslices. For each source timeslice t_0, we used two positions $(\vec{x}_1, t_0)$ and $(\vec{x}_2, t_0)$ as sources for three-point functions. We placed nucleon sinks in both the forward and backward directions on timeslices $t_0 \pm T$ to double statistics and obtain a total of 24672 samples, and used five source-sink separations $T/a \in \{6, 8, 10, 12, 14\}$.

We computed the disconnected loops

$$T_\mu^q(\vec{k}, t) \equiv -\sum_{\vec{x}} e^{i\vec{k}\cdot\vec{x}} \operatorname{Tr}\left[\gamma_\mu\gamma_5 D_q^{-1}(x, x)\right], \tag{5.1}$$

by following the procedure described in Sec. 2.2.2 and on timeslices $t_0 + \tau$ displaced only in the forward direction from each source timeslice, yielding 6168 timeslice samples; the source-operator separations τ and number of Hadamard vectors for each

[1] For the pion and η_s mass, the second error is from uncertainty in the lattice spacing.

$\tau/a =$	3	4	5	6	7
light	16	128	128	128	16
strange		16	128	16	

Table 5.1: Number of Hadamard vectors used for disconnected loops of each flavor and source-operator separation τ. Five separations were used for light quarks and three for strange. As shown in Sec. 5.1.2, sixteen Hadamard vectors is generally sufficient for the noise to saturate when using the axial current. Having 128 Hadamard vectors was particularly useful for Ref. [65], which used the vector current.

flavor are listed in Tab. 5.1. For each source timeslice, we computed sixteen two-point functions from source positions $(\vec{x}_i, t_0)$, $i = 1, \ldots, 16$, yielding 98688 samples for correlating with the disconnected loops. We imposed two constraints on our choice of momenta: $(\vec{p}\,' - \vec{p})^2 \leq 10(\frac{2\pi}{L_s})^2$ and $(\vec{p})^2, (\vec{p}\,')^2 \leq 6(\frac{2\pi}{L_s})^2$. For the connected diagrams we used two sink momenta, $\vec{p}\,' = \vec{0}$ and $\vec{p}\,' = \frac{2\pi}{L_s}(-1, 0, 0)$, and all source momenta compatible with the constraints. For the disconnected diagrams we used all combinations of $\vec{p}$ and $\vec{p}\,'$ compatible with the constraints, with the restriction that each Q^2 must match a value available from the connected diagrams.

On each set of four adjacent gauge configurations, we averaged over all spatially displaced samples of each correlator. This produced 257 blocked samples. Statistical error analysis was done using jackknife resampling.

The general form for $O(a)$ improvement of quark bilinear operators with nondegenerate quarks was given in Ref. [23]. If we simplify the expressions by keeping only their form at one-loop order in perturbation theory, the renormalized improved operators take the form

$$\begin{aligned} (A_\mu^q - A_\mu^{q'})^{R,I} &= Z_A \left[A_\mu^q - A_\mu^{q'} + a c_A \partial_\mu (P^q - P^{q'}) + a b_A (m_q A_\mu^q - m_{q'} A_\mu^{q'}) \right], \\ \left(\sum_q A_\mu^q \right)^{R,I} &= \bar{Z}_A \left[\sum_q A_\mu^q + a c_A \partial_\mu \sum_q P^q + a b_A \sum_q m_q A_\mu^q \right], \end{aligned} \tag{5.2}$$

for the flavor nonsinglet and singlet cases, respectively, where P is the pseudoscalar density. Matching with the improvement of the action, we take the tree-level value $c_A = 0$. Note that in nucleon matrix elements, the term proportional to c_A only contributes to the G_P form factors and therefore this term is not necessary for $O(a)$

improvement of $G_A(Q^2)$. The mass-dependent terms can effectively cause a mixing between singlet and nonsinglet axial currents; rather than determine b_A explicitly, we absorb the mass-dependent terms into the renormalization factors, which now become a matrix. The renormalization matrix is determined nonperturbatively using the Rome-Southampton method, which we discuss in detail in Section 5.2.

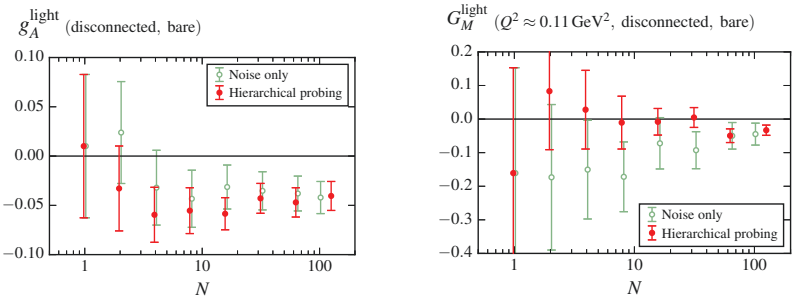

Figure 5-1: Comparison of hierarchical probing to the "Noise only" method at equal computational cost, using a reduced set of 366 configurations where we have data from both methods. The plots show results for the disconnected light-quark g_A (left) and disconnected light-quark magnetic form factor $G_M(Q^2 \approx 0.11\ \text{GeV}^2)$ (right) from the ratio method at $T/a = 10$, $\tau/a = 5$. The results are plotted as a function of N, which denotes the number of noise samples or the number of Hadamard vectors used to estimate each quark loop. Data points (slightly offset horizontally for clarity) are shown for $N = 1, 2, 4, 8, 16, 32, 64$ (both methods), $N = 100$ (noise only), and $N = 128$ (hierarchical probing).

5.1.2 Effectiveness of hierarchical probing

On a reduced set of 366 configurations, we have data for the disconnected light-quark loops from two different methods: hierarchical probing, as used for the main calculations of this work, and "Noise only", where the sum over n in Eq. (2.38) is over N random noise samples rather than N_{hvec} Hadamard vectors multiplying a single noise sample. Note that this means color and spin dilution is used in both cases. Thus, at $N = N_{\text{hvec}}$ the computational cost for both methods is the same. Figure 5-1 shows results from both methods as a function of $N = N_{\text{hvec}}$. Hierarchical probing is always guaranteed to perform at least as well as the traditional noise method. For

our setup we find that the uncertainty in the disconnected light-quark g_A saturates at $N_{\text{hvec}} = 16$, where it becomes dominated by gauge noise. For g_A with $N = N_{\text{hvec}} = 16$, the reduction in the (combined gauge+stochastic) uncertainty is only by a modest factor of 1.4. The improvement from hierarchical probing is more significant for the disconnected electromagnetic form factors [65], as illustrated in Fig. 5-1 (right) for the disconnected light-quark contribution to G_M at $Q^2 \approx 0.11\ \text{GeV}^2$. In this case, the stochastic noise dominates over the gauge noise up to a larger value of N (saturation is not yet reached in the range considered), and at large N the improvement from hierarchical probing is more pronounced, as expected because of the greater "coloring distance" [115].

5.1.3 Excited-state effects

It turns out that the different form factors suffer from quite different amounts of excited-state contamination. In addition, the available (T, τ) combinations are quite different between our connected-diagrams data and our disconnected-diagrams data. In particular, the former are much better suited for applying the summation method than the latter. Therefore we choose the best method for isolating the ground state separately for each form factor. We do this by examining "plateau" plots where, for each (T, τ) we determine "effective" form factors[2] from the ratios assuming the absence of excited states. In a region where excited-state effects are negligible, these effective form factors will form a stable plateau. In addition to these plateaus from the ratio method, we also show results from the summation method, taking the sums with three adjacent points $\{T, T + 2a, T + 4a\}$ and fitting with a line to determine the slope.

Figure 5-2 (top row) shows plateau plots for the isovector axial form factor $G_A^{u-d}(Q^2)$. For the axial charge $g_A \equiv G_A^{u-d}(0)$ (top left), the centers of the plateaus appear stable by $T/a = 10$ and 12, which agree within uncertainty. The center of the plateau for the largest source-sink separation, $T = 14a$, is shifted significantly higher, however, its statistical uncertainty is quite large and the magnitude of the shift goes against ex-

[2] In this subsection we show bare form factors, i.e., before renormalization.

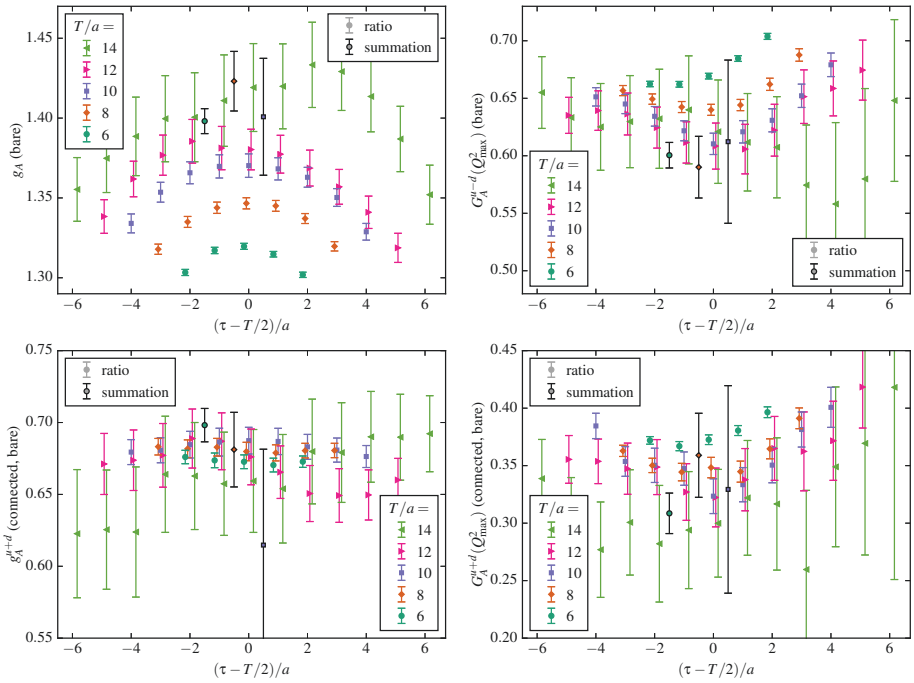

Figure 5-2: Plateau plots for the bare isovector (top row) and connected isoscalar (bottom row) axial form factors at zero (left column) and the highest (right column) momentum transfer Q^2. Solid symbols indicate data computed using the ratio method. Symbols with black outlines and black error bars indicate data from the summation method and are plotted in open spaces between ratio data near the origin for clarity.

pectations: in the asymptotic regime, as T is increased the shift between neighboring values of T is expected to decrease. Therefore we conclude that the shift at $T = 14a$ is likely a statistical fluctuation[3] and take the results from $T = 12a$ as the best option using the ratio method. For the summation method, all three points are consistent within the uncertainty and we conclude that the summation method has reached a plateau already at the shortest source-sink separation, $T = 6a$ (i.e., from fitting to the sums with $T/a \in \{6, 8, 10\}$). We take this as our primary analysis method for the isovector axial form factor $G_A^{u-d}(Q^2)$. For this form factor and for any observable derived from it, we estimate systematic uncertainty due to excited-state effects as the root-mean-square (RMS) deviation between the primary result (summation with $T = 6a$) and two alternatives: the ratio method with $T = 12a$ and the summation method with $T = 8a$. Looking at the corresponding plateau plot (top right) for the isovector axial form factor at our largest momentum transfer (about 1.1 GeV^2) indicates that this approach is also reasonable at nonzero Q^2. The bottom row of the same figure shows the equivalent plots for the contribution from quark-connected diagrams to the isoscalar axial form factor $G_A^{u+d}(Q^2)$. The excited-state effects appear to be slightly milder than for the isovector case, and we thus choose to apply the same analysis strategy.

Plateau plots for the contributions from quark-disconnected diagrams to axial form factors are shown in Fig. 5-3. Note that since these form factors were computed for several fixed source-operator separations τ, we choose to use the operator-sink separation $T - \tau$ as the horizontal axis. The top row shows the light-quark case, where we computed disconnected loops for five source-operator separations, and the bottom row shows the strange-quark case where we only computed three source-operator separations. The left and right columns show $Q^2 = 0$ (i.e., the contributions to the nucleon spin) and our largest momentum transfer, respectively. In general, we do not see any significant dependence on $T-\tau$ for $T-\tau \gtrsim 5a$. Since the disconnected data were averaged over the exchange of source and sink momenta, the effective form

[3] Similar behavior was previously seen in the isovector Pauli form factor computed using the same dataset [64].

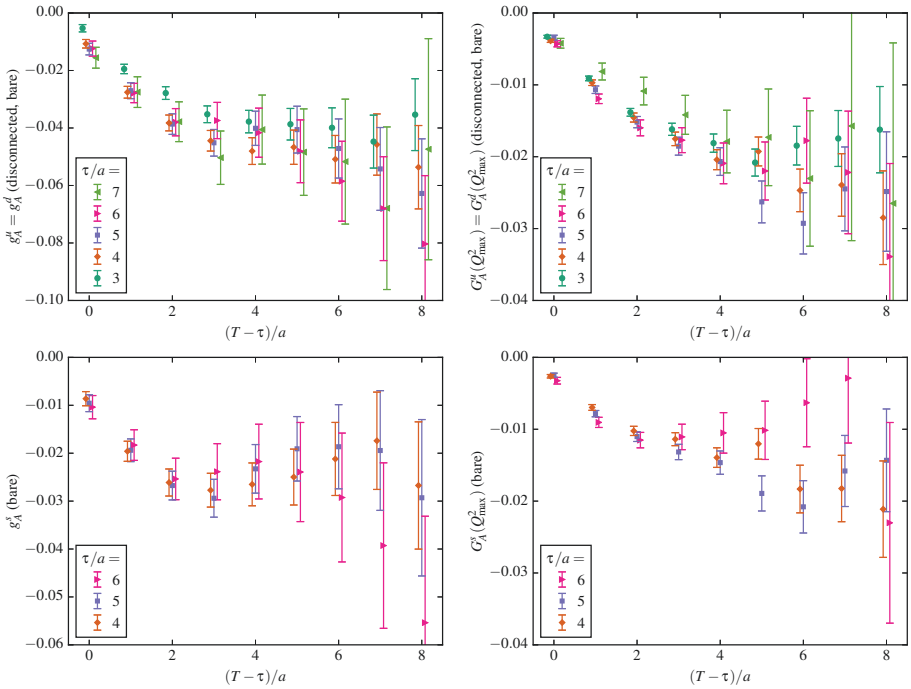

Figure 5-3: Plateau plots for the bare disconnected light (top row) and strange (bottom row) axial form factors at zero (left column) and the highest (right column) momentum transfer Q^2.

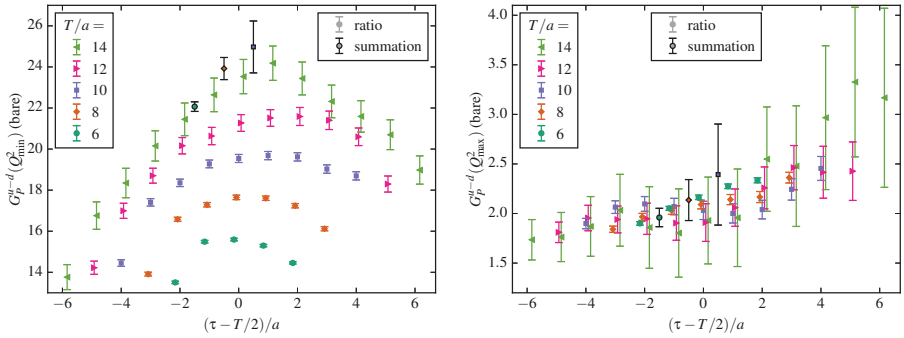

Figure 5-4: Plateau plots for the bare isovector induced pseudoscalar form factor $G_P^{u-d}(Q^2)$ at the lowest (left) and highest (right) momentum transfer Q^2. Solid symbols indicate data computed using the ratio method, and symbols with black outlines and black error bars indicate data from the summation method.

factors are expected to be symmetric, and therefore this corresponds to a source-sink separation of $T = 10a$. We use this for our primary result (averaged over the three points near $\tau = T/2$, which reduces statistical uncertainty), and use the RMS deviation with results from $T = 8a$ and $T = 12a$ as our estimate of systematic uncertainty due to excited states.

The isovector induced pseudoscalar form factor $G_P^{u-d}(Q^2)$ at the lowest available momentum transfer (about 0.1 GeV^2) is shown in Fig. 5-4 (left). This has very large excited-state effects (there is nearly a factor of two between the smallest and largest value on the plot), and there is no sign that a plateau has been reached using the ratio method. For the summation method, the points with $T/a = 8$ and 10 are consistent, suggesting that a plateau might possibly have been reached. We take the summation method with $T = 8a$ as our primary analysis method for this form factor and estimate the systematic uncertainty as the RMS deviation between the primary result and those from the ratio method with $T/a = 14$ and 12. Although the latter is clearly not in the plateau regime, we nevertheless include it in order to reflect the poor control over excited-state effects that is available in our data. At larger Q^2 (right), the excited-state effects are much milder and our error estimate should be conservative.

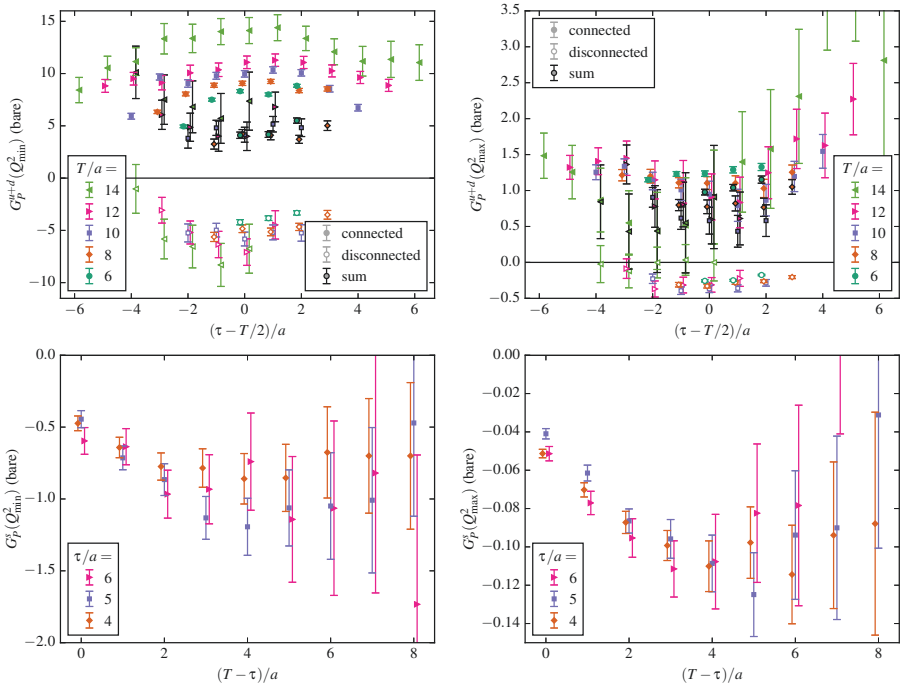

Figure 5-5: Plateau plots for the bare isoscalar light (top row) and strange (bottom row) induced pseudoscalar form factors at the lowest (left) and highest (right) momentum transfer Q^2. In the top row: solid and open symbols indicate the contributions from connected and disconnected diagrams, respectively, and symbols with black outlines and black error bars indicate their sum.

Plateau plots for the light and strange isoscalar induced pseudoscalar form factors are shown in Fig. 5-5. For $G_P^{u+d}(Q^2)$ at the lowest available momentum transfer (top left), we again find that the connected contributions have significant excited-state effects. On the same plot, we show the partial plateaus (limited to the available values of τ) for the contributions from disconnected diagrams. Although they are a bit noisier, they also appear to contain excited-state effects, with the opposite sign. In fact, the opposite signs cause the sum of connected and disconnected diagrams to have smaller excited-state contamination. For the sum, using the ratio method with $T = 10a$ appears to be a safe choice, also at the maximum momentum transfer (top right). When we examine the individual connected and disconnected contributions, we will make the same choice, with the understanding that the results include some contamination from excited states, and can only be studied qualitatively. This choice also appears safe for $G_P^s(Q^2)$ (bottom left and right). As for the disconnected G_A form factors, we use the RMS difference with $T/a = 8$ and 12 as our estimate of systematic uncertainty due to excited states.

5.1.4 Form factor fits using the z expansion

Having computed nucleon form factors at several discrete values of Q^2, we fit them with curves to characterize their overall shape and determine observables such as the axial radius from their slope at $Q^2 = 0$. It has been common to perform these fits using simple ansatzes, such as a dipole, which is often used to describe experimental data for the isovector $G_A(Q^2)$, however, these tend to be highly constrained and introduce a model dependence into the results. Instead, we use the model-independent z expansion, explained in Sec. 2.5.2. This was used in Refs. [21, 22, 97] to study axial form factors determined from quasielastic (anti)neutrino-nucleon scattering; it was found that fitting with the z expansion produced a significantly larger axial radius with a larger uncertainty, compared with dipole fits.

The G_P form factors have an isolated pole below the particle production threshold at the pseudoscalar meson mass, which we remove before fitting. We thus perform

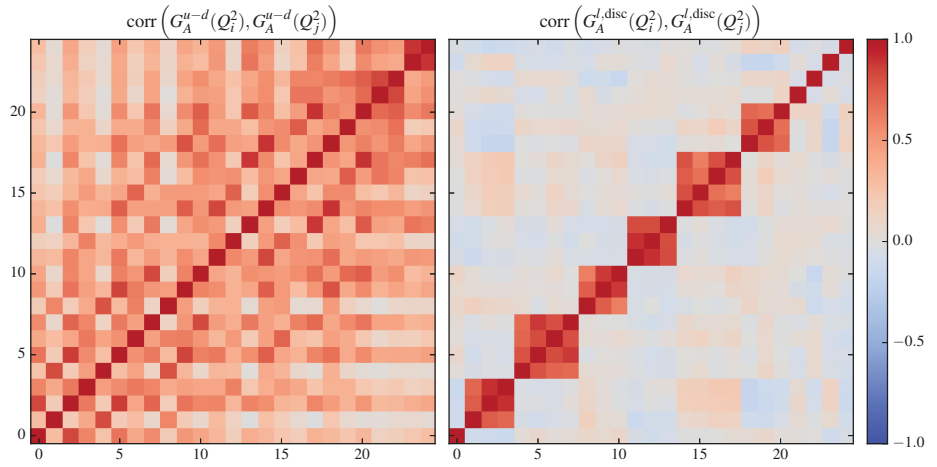

Figure 5-6: Correlations between data at different Q^2. Left: the isovector axial form factor $G_A^{u-d}(Q^2)$. Right: the quark-disconnected contribution to the light-quark axial form factor $G_A^{l,\mathrm{disc}}(Q^2)$. The axes index the different momentum transfers, which are sorted in order of increasing Q^2.

fits to

$$G(Q^2) = \begin{cases} G_A(Q^2) & \\ (Q^2 + m_\pi^2) G_P(Q^2) & \text{isovector} \\ (Q^2 + m_\eta^2) G_P(Q^2) & \text{isoscalar} \end{cases} . \tag{5.3}$$

We perform correlated fits by minimizing Eq. (2.60). With limited statistics it can be difficult to obtain a reliable estimator, and therefore we choose to reduce statistical fluctuations by interpolating between the jackknife estimate of the covariance matrix and a simplified (less noisy but biased) estimate, and then inverting the resulting matrix. This is in the spirit of shrinkage estimators [88, 111], however, we do not perform an optimization step with respect to the interpolation parameter.

In order to choose the form of the target (simplified) covariance matrix, we examine the correlation matrix

$$R_{ij} \equiv \frac{C_{ij}}{\sqrt{C_{ii} C_{jj}}}, \tag{5.4}$$

where C is the jackknife estimate of the covariance matrix. We find that this has

a quite different form between connected diagrams and disconnected diagrams. Figure 5-6 shows two example correlation matrices. For connected diagrams, illustrated with $G_A^{u-d}(Q^2)$ (left), we find modest correlations between different values of Q^2 but no strong pattern. For disconnected diagrams, illustrated with the quark-disconnected contribution to the light-quark G_A form factor (right), the correlation matrix is nearly block-diagonal. Each block corresponds to values of Q^2 that share the same spatial momentum transfer $(\vec{p}' - \vec{p})^2$ and thus the same Fourier modes of the disconnected loops. There are strong correlations within each block but weak correlations between different blocks.

For connected diagrams, we set $\Xi = ((1-\lambda)C + \lambda C_{\text{diag}})^{-1}$, where C_{diag} is the diagonal part of the covariance matrix. This is equivalent to multiplying the off-diagonal elements of C by $1-\lambda$. We use the mild value of $\lambda = 0.1$ as our main choice. For disconnected diagrams, we compute the average r over all elements of R_{ij} where i and j $(i \neq j)$ correspond to the same spatial momentum transfer. We then use for Ξ the inverse of the matrix $R^\star_{ij}\sqrt{C_{ii}C_{jj}}$, where

$$R^\star_{ij} = \begin{cases} 1 & i = j \\ (1-\lambda_1)R_{ij} & i \text{ and } j \text{ have different } (\vec{p}' - \vec{p})^2 \\ (1-\lambda_2)R_{ij} + \lambda_2 r & i \text{ and } j \text{ have the same } (\vec{p}' - \vec{p})^2 \end{cases} . \tag{5.5}$$

As our main choice, we use $(\lambda_1, \lambda_2) = (1, \frac{1}{2})$.

To estimate systematic uncertainty from fitting, we perform several alternative fits. We halve the value of w. For connected diagrams, we perform fits with $\lambda = 0$ and 1. For disconnected diagrams, we perform fits with $(\lambda_1, \lambda_2) = (0,0)$, $(1,0)$, and $(1,1)$. Finally, we take the RMS difference between results from all of the alternative fits as our estimate.

5.2 Renormalization

To compare our results with phenomenology, the lattice axial current needs to be renormalized. We determine the necessary renormalization factors nonperturbatively using the Rome-Southampton approach [96]. Going beyond the usual computation of the flavor nonsinglet renormalization factor, we also renormalize the flavor singlet axial current nonperturbatively. This requires disconnected quark loops but we are able to reuse the same loops that were computed for nucleon three-point functions. Since we perform these calculations on just one ensemble without taking the chiral limit, we effectively absorb the mass-dependent operator improvement terms into the renormalization (see Sec. 5.1.1), which requires us to determine a matrix of renormalization factors.

The singlet-nonsinglet difference in axial renormalization factors has been previously studied nonperturbatively by QCDSF [39] at the $SU(3)$ flavor symmetric point, using additional lattice ensembles and the Feynman-Hellmann relation to determine the contributions from disconnected quark loops. For the case of two degenerate quark flavors, nonperturbative results were presented by RQCD at the Lattice 2016 conference [14], using stochastic estimation for the disconnected loops similarly to this work. The singlet-nonsinglet difference has also been studied at leading (two-loop) order in lattice perturbation theory for a variety of improved Wilson-type actions [114, 44].

For calculating the axial renormalization constants, we follow the Rome- Southampton approach explained in Sec. 2.6 in both RI′-MOM and RI-SMOM schemes. The rest of this section is organized as follows: We determine the light and strange vector current renormalization factors in Sec. 5.2.1, study discretization effects and breaking of rotational symmetry in Sec. 5.2.2, and discuss issues of matching to the $\overline{\text{MS}}$ scheme and running of the flavor singlet axial current in Sec. 5.2.3. Subsections 5.2.4 and 5.2.5 explain our procedure for calculating the Z_A renormalization matrix, and finally we give the details of the calculation and its results in Sec. 5.2.6.

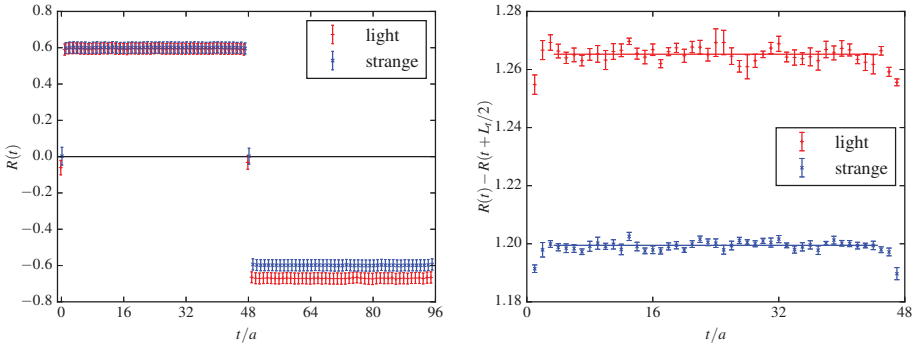

Figure 5-7: Determination of the vector current renormalization factors. Left: ratio of pseudoscalar three-point to two-point functions. Right: difference of the ratio on opposite sides of the interpolating operator. The horizontal lines indicate the plateau averages.

5.2.1 Vector current renormalization

We obtain the mass-dependent light and strange vector current renormalization factors from matrix elements of pseudoscalar mesons following, e.g., Ref. [49]. For π and η_s states, we compute zero-momentum two-point functions $C_2(t)$ as well as three-point functions $C_3(t)$ with source-sink separation $T = L_t/2$ and an operator insertion of the time component of the local (light or strange) vector current at source-operator separation t. We form the ratio $R(t) = C_3(t)/C_2(T)$, so that the charge of the interpolating operator gives the renormalization condition

$$Z_V \left(R(t_1) - R(t_2) \right) = 1, \tag{5.6}$$

for $0 < t_1 < T < t_2 < L_t$. Taking the difference $R(t) - R(t+T)$ results in a large cancellation of correlated statistical uncertainties. Results are shown in Fig. 5-7. We average over the long plateau, excluding three points at each end, and obtain $Z_V^l = 0.7903(2)$ and $Z_V^s = 0.8337(2)$.

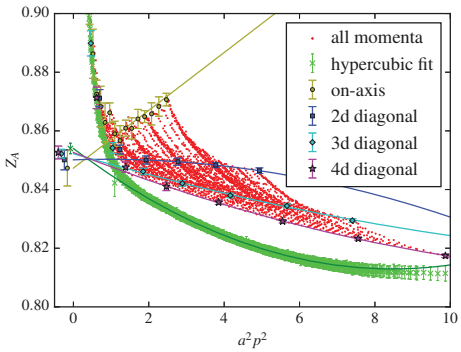

Figure 5-8: Isovector axial renormalization factor in the RI′-MOM scheme, computed for all lattice momenta with $|p_\mu| \leq \frac{\pi}{2a}$. The raw data for all momenta are shown without error bars to reduce clutter. The points that correspond to momenta that are on-axis or along one of the diagonals are highlighted and shown with error bars, as are the points that result from the hypercubic fit. The curves show the fits that extrapolate a^2p^2 to zero to remove rotationally invariant lattice artifacts, and the points at $a^2p^2 \lesssim 0$ show the results of the extrapolations.

5.2.2 Study of discretization effects

We perform a dedicated study of discretization effects and breaking of rotational symmetry, for the isovector case in the RI′-MOM scheme. Using translation invariance to remove the sum over y in Eqs. (2.63) and (2.64), we compute point-source quark propagators from a fixed point y, which allows us to efficiently obtain the gauge-averaged quark propagator and Green's functions for a large set of momenta. Specifically, we save data for all momenta in the inner 1/16 of the lattice Brillouin zone, i.e., with $|p_\mu| \leq \frac{\pi}{2a}$. After checking that the breaking of hypercubic symmetry due to the different lattice temporal and spatial extents is negligible, we averaged the estimates for the isovector Z_A over all hypercubic equivalent momenta.

Since the lattice breaks rotational symmetry, estimates of Z_A will depend not only on p^2, but also on the hypercubic invariants $p^{[2n]} \equiv \sum_\mu (p_\mu)^{2n}$. We make use of the hypercubic fit from Refs. [28, 29] to remove the leading terms that break rotational

symmetry and collapse the data to a single function of p^2:

$$Z_A(p^2, p^{[4]}, p^{[6]}, \dots) = Z_A^0(p^2) + c_1 \frac{a^2 p^{[4]}}{p^2} + c_2 \left(\frac{a^2 p^{[4]}}{p^2} \right)^2 + c_3 \frac{a^4 p^{[6]}}{p^2} + c_4 a^4 p^{[4]}. \quad (5.7)$$

The fit parameters are the four c_i that control breaking of hypercubic symmetry and a separate $Z_A^0(p^2)$ for each p^2. The data $Z_A(p^2, p^{[4]}, \dots)$ and the fit result $Z_A^0(p^2)$ are shown in Fig. 5-8. This is effective at producing a smooth curve that depends only on p^2 and not the other hypercubic invariants. The resulting curve still contains $O(a^2p^2)$ rotationally invariant lattice artifacts, so we perform a second fit in the range $a^2p^2 \in [2, 6]$ assuming a quadratic dependence on a^2p^2, and extrapolate to $a^2p^2 = 0$; this is also shown in Fig. 5-8.

An alternative approach is to pick an initial direction p_* and restrict our analysis to points $p = \lambda p_*$. Then the hypercubic invariants have the form $p^{[2n]} = c_{2n} p^{2n}$ for some fixed c_{2n} that depend on p_*. Thus, for this set of points along a fixed direction, the dependence on hypercubic invariants reduces to dependence only on p^2. We choose four sets of points: on-axis momenta, and momenta along 2, 3, or 4-dimensional diagonals, i.e., $p_* = (0, 0, 0, 1)$, $(0, 0, 1, 1)$, $(0, 1, 1, 1)$, and $(1, 1, 1, 1)$. For each set of points, we again do a fit to extrapolate a^2p^2 to zero. Because in this case there are fewer points available, we expand the fit range to be $a^2p^2 \in [1.5, 10]$. For on-axis points we use a linear fit because a^2p^2 does not reach very high, and for the n-dimensional diagonals we use a quadratic fit. The points from each set and the fit curves are shown in Fig. 5-8.

We find that the Z_A determined from the hypercubic fit and from the fits along different diagonals are all consistent with one another. This indicates that we can reliably control these lattice artifacts by choosing only points along a fixed direction, which is the approach that we will use for our main results for the axial renormalization matrix.

5.2.3 Matching to $\overline{\text{MS}}$ and running of the singlet axial current

We consider the singlet and nonsinglet axial currents

$$A^0_\mu = \frac{1}{\sqrt{N_f}}\bar{\psi}\gamma_\mu\gamma_5\psi, \qquad A^a_\mu = \bar{\psi}\gamma_\mu\gamma_5\lambda^a\psi, \tag{5.8}$$

where ψ is the fermionic field and λ^a is an $SU(N_f)$ generator acting in flavor space. The nonsinglet current should be renormalized such that it satisfies the axial Ward identity associated with chiral symmetry, and the renormalized singlet current should satisfy the one-loop form of the axial anomaly. The nonsinglet axial current has no anomalous dimension and is appropriately renormalized to all orders in perturbation theory in $\overline{\text{MS}}$ (using dimensional regularization with a naive anticommuting version of γ_5), RI′-MOM and RI-SMOM schemes. Thus the matching factor between these schemes is 1, and $Z_A = 1$ when using a chiral regulator.

For the singlet current, dimensional regularization with a naive γ_5 is inappropriate since the anomaly is not reproduced, and thus the 't Hooft-Veltman prescription for γ_5 is necessary. Using it in $\overline{\text{MS}}$, an additional finite matching factor Z_5^s is needed for the renormalized current to satisfy the one-loop form of the axial anomaly [87]. Thus renormalized, the singlet current has an anomalous dimension, $\gamma = (\frac{\alpha}{4\pi})^2(-6C_F N_f) + O(\alpha^3)$ [85], where the $O(\alpha^3)$ term is given in Ref. [87]. Using the same dimensional regularization, it was shown in Ref. [25] that the conversion factor between $\overline{\text{MS}}$ (including the finite factor Z_5^s) and RI-SMOM is $1 + O(\alpha^2)$.

For computing the matching between RI′-MOM and RI-SMOM, at one-loop order there should be no distinction between singlet and nonsinglet currents. Since the matching factor is 1 for nonsinglet currents, we conclude that the conversion factor for the singlet axial current in RI′-MOM is $1 + O(\alpha^2)$.

We remove the running of the singlet Z_A by evolving to a fixed scale. The evolution is given by

$$\mu^2 \frac{d}{d\mu^2} \log\left(Z_5^s Z_A^{\overline{\text{MS}},\text{HV}}\right) = \gamma(\alpha) = -\sum_i \gamma_i \alpha^{i+1}, \tag{5.9}$$

$$\mu^2 \frac{d}{d\mu^2} \alpha = \beta(\alpha) = -\sum_i \beta_i \alpha^{i+2}, \tag{5.10}$$

where the relevant coefficients are

$$\begin{aligned}
\beta_0 &= \frac{1}{4\pi}\left(\frac{11}{3}C_A - \frac{4}{3}T_F N_f\right) = \frac{1}{4\pi}\left(11 - \frac{2}{3}N_f\right), \\
\beta_1 &= \frac{1}{(4\pi)^2}\left(\frac{34}{3}C_A^2 - \frac{20}{3}C_A T_F N_f - 4 C_F T_F N_f\right) = \frac{1}{(4\pi)^2}\left(102 - \frac{38}{3}N_f\right), \\
\gamma_0 &= 0, \\
\gamma_1 &= \frac{1}{(4\pi)^2}(6 C_F N_f) = \frac{1}{(4\pi)^2} 8 N_f,
\end{aligned} \tag{5.11}$$

using $C_A = 3$, $C_F = 4/3$, and $T_F = 1/2$. At two-loop order, the evolution of α is given by [108]

$$\alpha(\mu) = -\frac{\beta_0}{\beta_1}\frac{1}{1 + W_{-1}(\zeta)}, \qquad \zeta = -\frac{\beta_0^2}{e\beta_1}\left(\frac{\Lambda^2}{\mu^2}\right)^{\beta_0^2/\beta_1}, \tag{5.12}$$

where W_k is the many-valued Lambert function defined by $W_k(\zeta) e^{W_k(\zeta)} = \zeta$. We use the PDG value, $\Lambda_3^{\overline{\text{MS}}} = 332(19)$ MeV [103]. Using $\gamma_0 = 0$, the evolution of the renormalization factor at two-loop order is given by

$$\frac{Z(\mu)}{Z(\mu_0)} = \left(\frac{\beta_0 + \beta_1 \alpha(\mu)}{\beta_0 + \beta_1 \alpha(\mu_0)}\right)^{\gamma_1/\beta_1}. \tag{5.13}$$

5.2.4 Renormalization of the axial current: $N_f = 2 + 1$

Consider the flavor-diagonal axial currents, Eq. (5.8), with $\psi = (u\ d\ s)^T$. We take $a = 3, 8, 0$, with $\mathrm{Tr}(\lambda^a \lambda^b) = \delta^{ab}$

$$\lambda^3 = \frac{1}{\sqrt{2}} \begin{pmatrix} 1 & 0 & 0 \\ 0 & -1 & 0 \\ 0 & 0 & 0 \end{pmatrix}, \ \lambda^8 = \frac{1}{\sqrt{6}} \begin{pmatrix} 1 & 0 & 0 \\ 0 & 1 & 0 \\ 0 & 0 & -2 \end{pmatrix}, \ \lambda^0 = \frac{1}{\sqrt{3}} \begin{pmatrix} 1 & 0 & 0 \\ 0 & 1 & 0 \\ 0 & 0 & 1 \end{pmatrix}. \tag{5.14}$$

Using i, j to label quark flavors, we compute the quark propagator $S_i(p)$ (Eq. (2.63)) for quark flavor-i, nonamputated and amputated Green's functions (Eq. (2.64), Eq. (2.65)) for mixed quark flavors-i and -j, $G^{\mathcal{O}}_{i,j}(p', p)$, and $\Lambda^{\mathcal{O}}_{ij}(p', p)$, respectively. These renormalize as

$$\Lambda^{A^a_\mu}_{R,ij}(p', p) = \frac{Z_A^{ab}}{\sqrt{Z_q^i Z_q^j}} \Lambda^{A^b_\mu}_{ij}(p', p). \tag{5.15}$$

For $N_f = 2 + 1$, the renormalization pattern is

$$Z_A = \begin{pmatrix} Z_A^{33} & 0 & 0 \\ 0 & Z_A^{88} & Z_A^{80} \\ 0 & Z_A^{08} & Z_A^{00} \end{pmatrix}, \tag{5.16}$$

and for $N_f = 3$, this reduces to two independent factors since $Z_A^{88} = Z_A^{33}$ and $Z_A^{80} = Z_A^{08} = 0$. In a RI′-MOM or RI-SMOM scheme, the renormalization condition for Z_A involves tracing Λ^{A_μ} with some projector P_μ at kinematics corresponding to the scale μ^2 (see Sec. 2.6.1). In the case of multiple flavors, this becomes

$$\sum_{ij} \lambda^a_{ji} \, \mathrm{Tr} \left[\Lambda^{A^b_\mu}_{R,ij} P_\mu \right]_{\mu^2} = \delta^{ab}, \tag{5.17}$$

so that we get

$$(Z_A^{-1}(\mu))^{ba} = \sum_{ij} \lambda^a_{ji} \, \mathrm{Tr} \left[\frac{1}{\sqrt{Z_q^i Z_q^j}} \Lambda^{A^b_\mu}_{ij} P_\mu \right]_{\mu^2}. \tag{5.18}$$

Specifically, this yields for $N_f = 2+1$

$$(Z_A^{-1})^{33} = \frac{1}{2Z_q^l}\,\mathrm{Tr}\left[\left(\Lambda_{u,u}^{A_\mu^{u-d}} - \Lambda_{d,d}^{A_\mu^{u-d}}\right) P_\mu\right] = \frac{1}{Z_q^l}\Sigma_{l,\mathrm{conn}}, \tag{5.19}$$

where $\Sigma_{l,\mathrm{conn}}$ is the connected contribution to the (u or d)-quark amputated axial vertex function, traced with P_μ. This corresponds to the usual isovector result. Writing $\Sigma^i_{j,\mathrm{disc}}$ for the disconnected contribution to the amputated vertex function with the flavor-i axial current and flavor-j external quark states, traced with P_μ, we get

$$\begin{aligned}(Z_A^{-1})^{88} &= \frac{1}{6}\,\mathrm{Tr}\left[\left(\frac{1}{Z_q^l}\Lambda_{u,u}^{A_\mu^{u+d-2s}} + \frac{1}{Z_q^l}\Lambda_{d,d}^{A_\mu^{u+d-2s}} - \frac{2}{Z_q^s}\Lambda_{s,s}^{A_\mu^{u+d-2s}}\right) P_\mu\right] \\ &= \frac{1}{3}\left(\frac{1}{Z_q^l}\Sigma_{l,\mathrm{conn}} + \frac{2}{Z_q^s}\Sigma_{s,\mathrm{conn}}\right) + \frac{2}{3}\left(\frac{1}{Z_q^l}\Sigma^{l-s}_{l,\mathrm{disc}} - \frac{1}{Z_q^s}\Sigma^{l-s}_{s,\mathrm{disc}}\right),\end{aligned} \tag{5.20}$$

$$\begin{aligned}(Z_A^{-1})^{80} &= \frac{1}{3\sqrt{2}}\,\mathrm{Tr}\left[\left(\frac{1}{Z_q^l}\Lambda_{u,u}^{A_\mu^{u+d-2s}} + \frac{1}{Z_q^l}\Lambda_{d,d}^{A_\mu^{u+d-2s}} + \frac{1}{Z_q^s}\Lambda_{s,s}^{A_\mu^{u+d-2s}}\right) P_\mu\right] \\ &= \frac{\sqrt{2}}{3}\left(\frac{1}{Z_q^l}\Sigma_{l,\mathrm{conn}} - \frac{1}{Z_q^s}\Sigma_{s,\mathrm{conn}}\right) + \frac{\sqrt{2}}{3}\left(\frac{2}{Z_q^l}\Sigma^{l-s}_{l,\mathrm{disc}} + \frac{1}{Z_q^s}\Sigma^{l-s}_{s,\mathrm{disc}}\right),\end{aligned} \tag{5.21}$$

$$\begin{aligned}(Z_A^{-1})^{08} &= \frac{1}{3\sqrt{2}}\,\mathrm{Tr}\left[\left(\frac{1}{Z_q^l}\Lambda_{u,u}^{A_\mu^{u+d+s}} + \frac{1}{Z_q^l}\Lambda_{d,d}^{A_\mu^{u+d+s}} - \frac{2}{Z_q^s}\Lambda_{s,s}^{A_\mu^{u+d+s}}\right) P_\mu\right] \\ &= \frac{\sqrt{2}}{3}\left(\frac{1}{Z_q^l}\Sigma_{l,\mathrm{conn}} - \frac{1}{Z_q^s}\Sigma_{s,\mathrm{conn}}\right) + \frac{\sqrt{2}}{3}\left(\frac{1}{Z_q^l}\Sigma^{2l+s}_{l,\mathrm{disc}} - \frac{1}{Z_q^s}\Sigma^{2l+s}_{s,\mathrm{disc}}\right),\end{aligned} \tag{5.22}$$

$$\begin{aligned}(Z_A^{-1})^{00} &= \frac{1}{3}\,\mathrm{Tr}\left[\left(\frac{1}{Z_q^l}\Lambda_{u,u}^{A_\mu^{u+d+s}} + \frac{1}{Z_q^l}\Lambda_{d,d}^{A_\mu^{u+d+s}} + \frac{1}{Z_q^s}\Lambda_{s,s}^{A_\mu^{u+d+s}}\right) P_\mu\right] \\ &= \frac{1}{3}\left(\frac{2}{Z_q^l}\Sigma_{l,\mathrm{conn}} + \frac{1}{Z_q^s}\Sigma_{s,\mathrm{conn}}\right) + \frac{1}{3}\left(\frac{2}{Z_q^l}\Sigma^{2l+s}_{l,\mathrm{disc}} + \frac{1}{Z_q^s}\Sigma^{2l+s}_{s,\mathrm{disc}}\right).\end{aligned} \tag{5.23}$$

It is clear that $(Z_A^{-1})^{80}$ and $(Z_A^{-1})^{08}$ vanish when $N_f = 3$, and the disconnected contribution to $(Z_A^{-1})^{88}$ is doubly suppressed by approximate $SU(3)_f$ symmetry.

Having evaluated an effective Z_A^{-1} in some scheme at a scale μ, we can invert the matrix and evolve to the target scale of 2 GeV

$$Z_A^{8i}(2\text{ GeV}) = Z_A^{8i}(\mu), \qquad Z_A^{0i}(2\text{ GeV}) = \left(\frac{Z_A^0(2\text{ GeV})}{Z_A^0(\mu)}\right)_{\text{pert}} Z_A^{0i}(\mu), \tag{5.24}$$

where the perturbative flavor-singlet evolution is given by Eq. (5.13). Finally, we fit with a polynomial in $a^2\mu^2$ to remove lattice artifacts. If we want to obtain a single-flavor axial current, such as the strange, we can write, e.g.,

$$\begin{aligned} A_\mu^{R,s} &= \frac{1}{\sqrt{3}} A_\mu^{R,0} - \sqrt{\frac{2}{3}} A_\mu^{R,8} \\ &= \frac{1}{3}\left(Z_A^{00} + 2Z_A^{88} - \sqrt{2}Z_A^{80} - \sqrt{2}Z_A^{08}\right) A_\mu^s \\ &\quad + \frac{1}{3}\left(Z_A^{00} - Z_A^{88} + \frac{1}{\sqrt{2}} Z_A^{08} - \sqrt{2}Z_A^{80}\right) A_\mu^{u+d} \\ &\equiv Z_A^{s,s} A_\mu^s + Z_A^{s,u+d} A_\mu^{u+d}. \end{aligned} \tag{5.25}$$

Similarly, we can evaluate the renormalized $u+d$ current

$$\begin{aligned} A_\mu^{R,u+d} &= \frac{2}{\sqrt{3}} A_\mu^{R,0} + \sqrt{\frac{2}{3}} A_\mu^{R,8} \\ &= \frac{1}{3}\left(2Z_A^{00} + Z_A^{88} + \sqrt{2}Z_A^{80} + \sqrt{2}Z_A^{08}\right) A_\mu^{u+d} \\ &\quad + \frac{2}{3}\left(Z_A^{00} - Z_A^{88} + \frac{1}{\sqrt{2}} Z_A^{08} - \sqrt{2}Z_A^{80}\right) A_\mu^s \\ &\equiv Z_A^{u+d,u+d} A_\mu^{u+d} + Z_A^{u+d,s} A_\mu^s. \end{aligned} \tag{5.26}$$

In order to study the disconnected light-quark current by itself, we introduce a quenched third light quark r, degenerate with u and d. Then the *connected* contribution to the matrix elements of the $u+d$ current is the same as matrix elements of the $u+d-2r$ current. Since this is a nonsinglet flavor combination formed from degenerate light quarks, it has the same renormalization factor as the isovector current.

To find the *disconnected* light-quark contribution, we take the difference

$$\begin{aligned} A_\mu^{R,l,\text{disc}} = A_\mu^{R,r} &= \frac{1}{2}(A_\mu^{R,u+d} - A_\mu^{R,u+d-2r}) \\ &= \frac{1}{2}(Z_A^{u+d,u+d}A_\mu^{u+d} + Z_A^{u+d,s}A_\mu^s - Z_A^{33}A_\mu^{u+d,\text{conn}}) \\ &= Z_A^{u+d,u+d}A_\mu^{l,\text{disc}} + \frac{1}{2}\left((Z_A^{u+d,u+d} - Z_A^{33})A_\mu^{u+d,\text{conn}} + Z_A^{u+d,s}A_\mu^s\right). \end{aligned} \tag{5.27}$$

5.2.5 Volume-source approach and reuse of disconnected diagrams

We evaluate our observables using quark propagators with four-dimensional volume plane-wave sources $D_q^{-1}(x|p) \equiv \sum_y D_q^{-1}(x,y)e^{ipy}$. For a quark-bilinear operator $\mathcal{O} = \bar{q}\Gamma q$ ($\Gamma = \gamma_\mu\gamma_5$ for the axial current), the connected contribution to the Green's function is obtained using

$$G_{\mathcal{O},\text{conn}}(p',p) = \frac{1}{V}\left\langle \sum_y e^{i(p'-p)y}\gamma_5 D_q^{-1}(y|p')^\dagger \gamma_5 \Gamma D_q^{-1}(y|p)\right\rangle_U, \tag{5.28}$$

where $\langle\ldots\rangle_U$ denotes the average over gauge configurations. We obtain the disconnected contribution by correlating the plane-wave-source propagators with the previously-computed disconnected loops[4] $T_\mu^q(\vec{k},t)$ (Eq. (5.1))

$$G_{\mathcal{O},\text{disc}}(p',p) = \frac{L_t}{V}\left\langle \sum_x e^{-ip'x} D_{q'}^{-1}(x|p) e^{ik_4 t} T_\mu^q(\vec{0},t)\right\rangle_U, \tag{5.29}$$

where q and q' are the quark flavors of the operator and the external quark states, and we choose $p'-p = (\vec{0},k_4)$. Translation invariance implies that this expression is independent of t, and we average over all timeslices on which the disconnected loops were computed.

[4] Recall that the loops are gauge invariant and thus do not need to be transformed to Landau gauge.

5.2.6 Results

In order to minimize cut-off effects we choose momenta on the diagonal of the Brillouin zone $p, p' \in \frac{2\pi k}{L_s}(1,1,1,\pm 1)$ for $k \in \{2,3,...,8\}$. Therefore, our momenta span the range $0.6 < a^2\mu^2 < 10$. We used for this calculation about 200 gauge configurations. This procedure involves the following steps:

1. Compute Landau gauge-fixed quark propagators and Green's functions for both light and strange quarks as outlined in the previous section. Form the amputated vertex functions.

2. On the connected diagrams, impose the RI′-MOM or RI-SMOM vector current renormalization conditions, together with the renormalization factors from Sec. 5.2.1, to find estimates for Z_q^l and Z_q^s at each scale μ.

3. Trace the axial amputated vertex functions with P_μ to obtain Σ^l_{conn}, Σ^s_{conn}, $\Sigma^l_{l,\text{disc}}$, $\Sigma^s_{l,\text{disc}}$, $\Sigma^l_{s,\text{disc}}$, and $\Sigma^s_{s,\text{disc}}$ at each scale $|p|$. By combining the different Σ following Eqs. (5.19–5.23), form the matrix Z_A^{-1}.

4. Invert the matrix and evolve from scale μ to 2 GeV.

5. Optionally, convert the Z_A matrix from the basis $\{A^3_\mu, A^8_\mu, A^0_\mu\}$ to $\{A^{u-d}_\mu, A^{u+d}_\mu, A^s_\mu\}$, using Eqs. (5.25) and (5.26).

6. Extrapolate μ to zero to remove $O(a^2\mu^2)$ lattice artifacts.

For estimating the statistical and systematic errors in removing the $O(a^2\mu^2)$ artifacts, we apply linear and quadratic fits for each matrix element, $Z_A^{ij} = c_0^{ij} + c_1^{ij}(a\mu)^2$ and $Z_A^{ij} = c_0^{ij} + c_1^{ij}(a\mu)^2 + c_2^{ij}(a\mu)^4$. We apply these fits in different ranges of $a^2\mu^2$, all of which lie within the range $[2.5, 10]$, i.e., always excluding the first two points. This fit procedure is applied to results from both RI′-MOM and RI-SMOM schemes. We take then three best fits in each scheme (yielding six values), average all of them to get the central value and statistical uncertainty, and use the root-mean-square difference between the six values and the average to get the systematic uncertainty. Figures 5-9

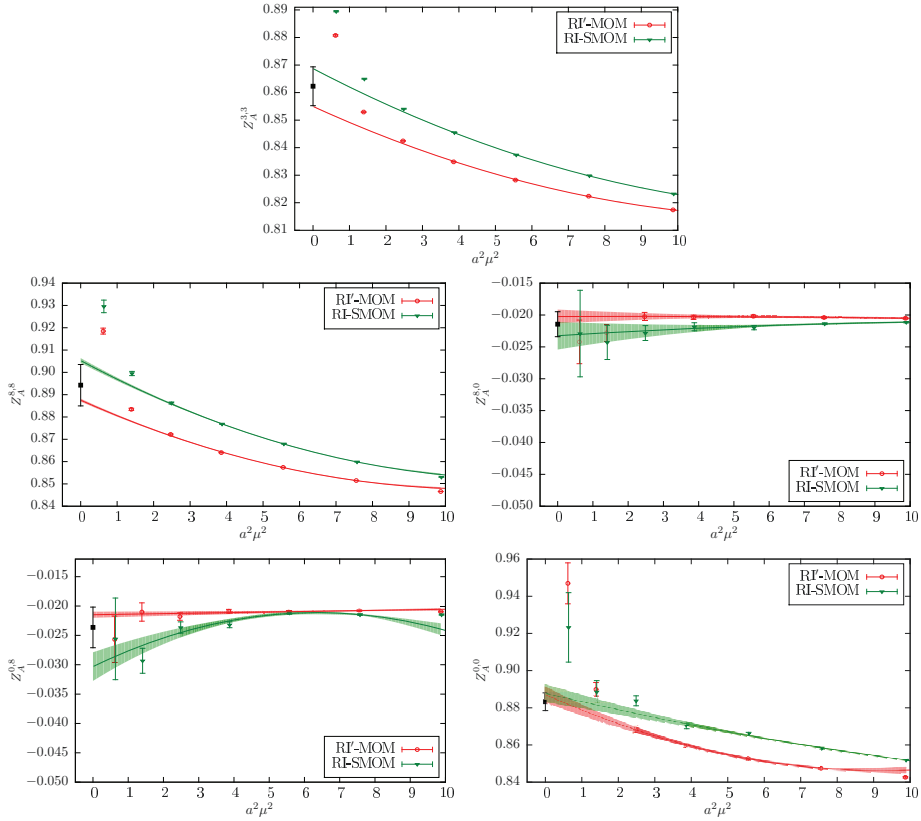

Figure 5-9: Z_A matrix elements for the $\{A^3_\mu, A^8_\mu, A^0_\mu\}$ basis, in the $\overline{\text{MS}}$ scheme at scale 2 GeV. Each plot shows the data versus the matching point $a^2\mu^2$ for the two intermediate schemes, as well as an illustrative fit curve for each scheme used to extrapolate to $a^2\mu^2 = 0$. The black point at $a^2\mu^2 = 0$ shows the value and the combined statistical and systematic uncertainty, based on these and other fits.

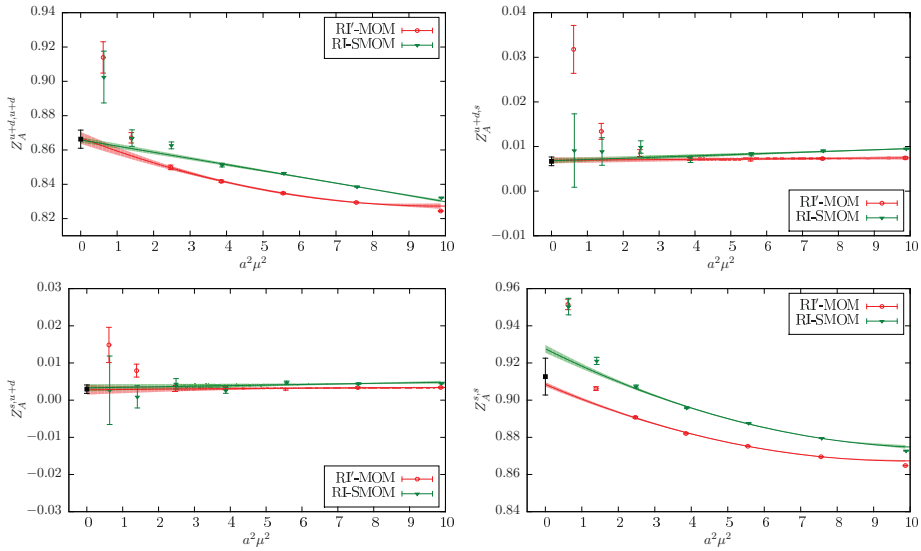

Figure 5-10: Z_A matrix elements for $\{A_\mu^{u+d}, A_\mu^s\}$. See the caption of Fig. 5-9.

and 5-10 show illustrative fits for obtaining the matrix elements in the different bases from both RI′-MOM and RI-SMOM schemes. We obtain the following Z_A matrices:

$$\begin{pmatrix} A_\mu^{R,3} \\ A_\mu^{R,8} \\ A_\mu^{R,0} \end{pmatrix} = \begin{pmatrix} 0.8623(1)(71) & 0 & 0 \\ 0 & 0.8942(6)(93) & -0.0214(13)(14) \\ 0 & -0.0236(1)(33) & 0.8832(30)(36) \end{pmatrix} \begin{pmatrix} A_\mu^3 \\ A_\mu^8 \\ A_\mu^0 \end{pmatrix}, \tag{5.30}$$

$$\begin{pmatrix} A_\mu^{R,u-d} \\ A_\mu^{R,u+d} \\ A_\mu^{R,s} \end{pmatrix} = \begin{pmatrix} 0.8623(1)(71) & 0 & 0 \\ 0 & 0.8662(26)(45) & 0.0067(8)(5) \\ 0 & 0.0029(10)(5) & 0.9126(11)(98) \end{pmatrix} \begin{pmatrix} A_\mu^{u-d} \\ A_\mu^{u+d} \\ A_\mu^s \end{pmatrix}. \tag{5.31}$$

Note that these two different matrices were obtained from independent fits to remove $O(a^2\mu^2)$ artifacts, and thus they are not related exactly by Eqs. (5.25) and (5.26). For renormalizing our nucleon form factor data, we use the latter matrix. Finally, the contribution from the bare connected light axial current to the renormalized disconnected light axial current depends on the difference $Z_A^{u+d,u+d} - Z_A^{33}$, as shown

in Eq. (5.27). In order to reduce uncertainties, we computed this difference by itself using the above procedures, and found $Z_A^{u+d,u+d} - Z_A^{33} = 0.0061(18)(10)$.

From Eq. (5.2) and the full mass-dependent $O(a)$ improvement in Ref. [23], $Z_A^{u+d,s}$ and $Z_A^{s,u+d}$ first appear at two-loop order in lattice perturbation theory; since the mass-dependent part is further suppressed by am_s, it follows that these are largely sensitive to the singlet-nonsinglet difference[5]. These elements are less than one percent of the diagonal ones, indicating a small difference, which is consistent with previous studies. For example, Ref. [39] found a singlet-nonsinglet difference $\bar{Z}_A - Z_A = 0.020(3)$, using a similar lattice action. In the $SU(3)$ flavor limit, this corresponds to $\bar{Z}_A - Z_A = 3Z_A^{s,u+d} = \frac{3}{2}Z_A^{u+d,s}$, so that those mixing factors are about twice as large as ours.

5.3 Axial form factors

5.3.1 G_A form factors

The isovector axial form factor is shown in Fig. 5-11 (left). From the fit, we find $g_A = 1.208(6)(16)(1)(10)$ and $r_A^2 = 0.213(6)(13)(3)(0)$ fm^2, where the uncertainties are due to statistics, excited states, fitting, and renormalization, respectively. The dominant uncertainty is excited-state effects. The fitted value of g_A is quite compatible with the value taken from the form factor at $Q^2 = 0$, $1.206(7)(19)(0)(10)$, with slightly smaller uncertainties. The axial charge was recently determined in a mostly independent calculation using the same ensemble [123], with somewhat higher statistics and different methodology. If we examine the bare quantity to avoid differences in renormalization factors, we get $g_A^{\text{bare}} = 1.401(7)(18)(2)$, which differs from the result in Ref. [123], $g_A^{\text{bare}} = 1.431(15)$, by slightly more than one standard deviation. We can compare the axial radius with the recent reanalysis of neutrino-deuteron scattering data [97] that found $r_A^2 = 0.46(22)$ fm^2. Our result is slightly more than one standard deviation smaller.

[5] This is in contrast with, e.g., $Z_A^{0,0} - Z_A^{8,8}$, which has a contribution at tree level proportional to $ab_A(m_s - m_{ud})$.

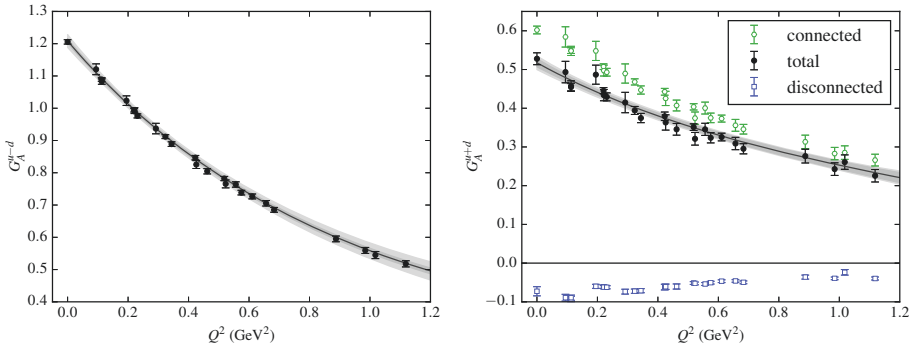

Figure 5-11: Isovector and light isoscalar axial form factors $G_A^{u-d}(Q^2)$ (left) and $G_A^{u+d}(Q^2)$ (right), and z-expansion fits to them. The lattice data and the inner error band for the fit show statistical uncertainties, whereas the outer error band for the fit shows the quadrature sum of statistical and systematic uncertainties. In addition, for the light isoscalar axial form factor, the corresponding form factors from the renormalized connected and disconnected diagrams are also shown.

Figure 5-11 (right) shows the light-quark isoscalar form factor $G_A^{u+d}(Q^2)$. The fit yields $g_A^{u+d} = 0.517(11)(14)(1)(3)$ and $(r_A^2)^{u+d} = 0.197(21)(21)(4)(0)$ fm^2. The statistical errors are relatively much larger than for the isovector case, and the dominant source of these errors is the connected diagrams. The uncertainty due to renormalization in g_A^{u+d} is mostly due to the diagonal element of the renormalization matrix; the effect of mixing with strange quarks is very small.

In Fig. 5-12 we show the strange and light disconnected axial form factors. The strange axial form factor $G_A^s(Q^2)$ is the most important case for mixing between light and strange axial currents, since it is small and it mixes under renormalization with $G_A^{u+d}(Q^2)$, which has a contribution from connected diagrams and is much larger. The effect of this mixing is shown in the left plot: it reduces the magnitude of the form factor by up to 10%, although this effect is smaller than the total statistical uncertainty. In these plots the block-correlated nature of the statistical uncertainties is clearly visible, particularly at low Q^2: the data that are strongly correlated form clusters of nearby points, but there are large fluctuations between different clusters. This effect was previously seen in the disconnected electromagnetic form factors computed using the same dataset [65]. Fits using the z expansion to

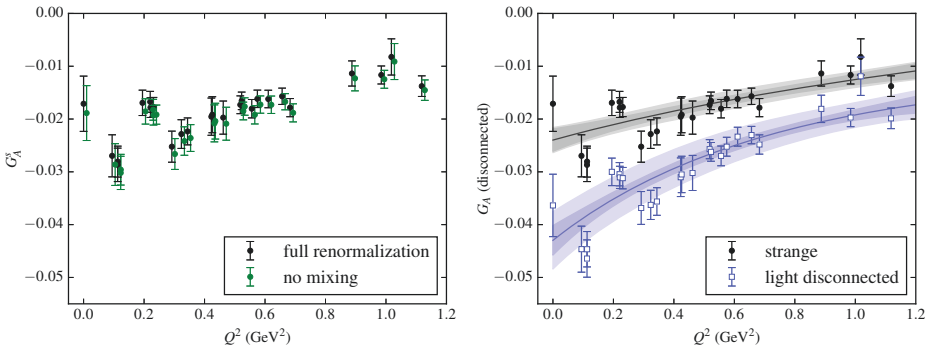

Figure 5-12: Disconnected axial form factors. Left: strange form factor, both with the full renormalization matrix and after setting the mixing with light quarks to zero. Right: strange and disconnected light-quark axial form factors, including z-expansion fits to them. See the caption of Fig. 5-11.

the strange and light disconnected form factors are shown in the right plot. From these fits we obtain $g_A^s = -0.0240(21)(8)(2)(7)$ and $g_A^{l,\text{disc}} = -0.0430(28)(46)(6)(8)$. The fit has the effect of averaging over several uncorrelated clusters of data, and produces a considerably smaller uncertainty than the value taken directly from the form factor at $Q^2 = 0$. The leading uncertainties are statistical and (for the light-quark case) excited-state effects. The uncertainty due to renormalization is dominated by uncertainty in the off-diagonal part of the renormalization matrix. We also obtain the radii $(r_A^2)^s = 0.155(73)(57)(7)(2)$ fm^2 and $(r_A^2)^{l,\text{disc}} = 0.248(57)(28)(18)(0)$ fm^2. Within their uncertainties, all of the squared axial radii are compatible with 0.2 fm^2.

5.3.2 Quark spin contributions

The axial form factors at zero momentum transfer, $g_A^q \equiv G_A^q(0)$, determined in the previous subsection, give the contribution from the spin of quarks q to the proton spin. We can compare against standard experimental inputs used for phenomenological determinations of these quark spin contributions. Using isospin symmetry, the $u - d$ combination is determined from the axial charge in neutron beta decay, $g_A^{u-d} = 1.2723(23)$ [103]. Our result is about 5% lower, which could be attributed to our heavier-than-physical pion mass.

q	g_A^q
u	0.863(7)(14)
d	−0.345(6)(9)
s	−0.0240(21)(11)

Table 5.2: Quark spin contributions to the nucleon spin.

The flavor nonsinglet combination $u+d-2s$ is typically obtained from semileptonic decays of octet baryons, assuming SU(3) flavor symmetry. Although there have been efforts to improve this determination using chiral perturbation theory (dating back to the original paper on the heavy baryon approach [81]), it was shown in Ref. [89] that at full next-to-leading order, there is a new low-energy constant that contributes to g_A^{u+d-2s} but not to the octet baryon decays. Thus, in the absence of additional input, this combination cannot be predicted at NLO. The leading-order fit to octet baryon decay data [89] yields $g_A^{u+d-2s} = 3F - D = 0.608(30)$. It is therefore useful to have a lattice QCD calculation of this quantity, even for a heavy pion mass, since it will enable full NLO chiral perturbation theory analyses to be done. Our result is $g_A^{u+d-2s} = 0.565(11)(13)$.

We find the total contribution from quark spin to the nucleon spin at $\mu = 2$ GeV is $g_A^{u+d+s} = 0.494(11)(15)$, about half. The other half must come from gluons and from quark orbital angular momentum. This is somewhat larger than results from phenomenological determinations of polarized parton distribution functions: recent analyses [54, 100, 110] give values from 0.18 to 0.28, with an uncertainty ranging from 0.04 to 0.21. There are a few possible sources for this discrepancy. First, that this is caused by our heavier-than-physical pion mass. This would require that the flavor singlet axial case be more sensitive than the isovector one to the pion mass. Second, that the unaccounted-for systematic uncertainties at this pion mass are large. These include effects due to finite lattice spacing and $O(\alpha^2)$ corrections to the matching of the flavor singlet axial current to $\overline{\text{MS}}$. In particular, the latter does not affect the flavor nonsinglet combinations, which are in better agreement with phenomenology. A third possibility is that the phenomenological values are incorrect. The behavior at small momentum fraction x is poorly constrained, and a recent estimate [86] in

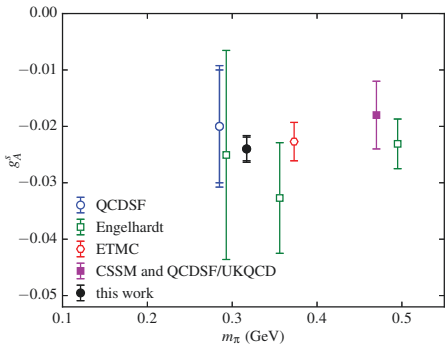

Figure 5-13: Lattice QCD values for g_A^s [13, 50, 1, 40], keeping only peer-reviewed results that use dynamical fermions and nonperturbative renormalization for at least the nonsinglet Z_A.

the large-N_c limit of the small-x asymptotics suggests that improved results at small x would lead to higher values of g_A^{u+d+s}.

The individual quark contributions are summarized in Tab. 5.2. Our result for g_A^s is compared with other lattice QCD results in Fig. 5-13. The results are all mutually consistent, and ours is the most precise. Our improved precision is due to much higher statistics than most previous calculations, as well as the use of a large volume and the additional constraints from data at nonzero Q^2 in the z-expansion fits. We also note the calculation at the physical pion mass by ETMC that was presented at Lattice 2016 [4], which found $g_A^s = -0.042(10)$. This differs from our result by almost two standard deviations, suggesting that the strange spin contribution to the nucleon spin becomes larger (more negative) as the light quark mass is decreased.

5.3.3 G_P form factors

Figure 5-14 shows the isovector induced pseudoscalar form factor $G_P^{u-d}(Q^2)$. As discussed in Sec. 5.1.4, we remove the pion pole that is present in this form factor before fitting using the z expansion. With the pion pole removed, the dependence on Q^2 is much weaker. At low Q^2, there is a large systematic uncertainty from excited-state contributions. For comparison with experiment, we consider ordinary muon capture of muonic hydrogen, which (assuming isospin symmetry) is sensitive to

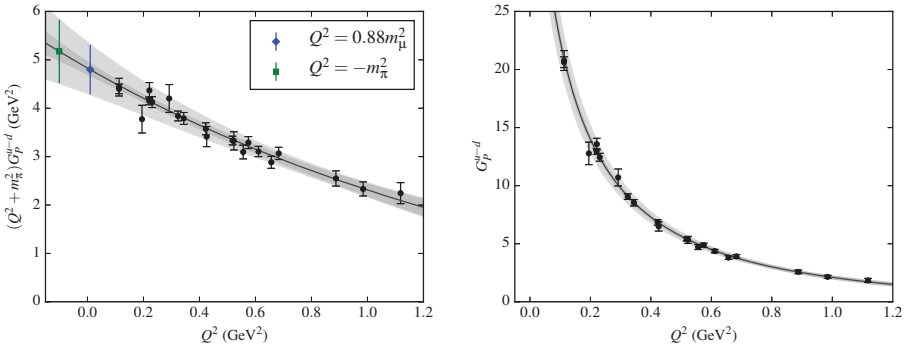

Figure 5-14: Isovector induced pseudoscalar form factor $G_P^{u-d}(Q^2)$ and the z-expansion fit to it. The left plot shows the form factor with the pion pole removed (which is directly fitted using the z expansion), and the right plot has the pole restored in the fit curve. The left plot also shows the extrapolations needed to obtain g_P^{norm} and $g_{\pi NN}$. See the caption of Fig. 5-11.

$g_P^* \equiv \frac{m_\mu}{2m_N} G_P^{u-d}(Q_*^2)$, where $Q_*^2 = 0.88 m_\mu^2$. To remove the strong dependence on the pion mass arising from the pion pole, we consider [9]

$$g_P^{\text{norm}} \equiv \frac{m_\mu}{2m_N} \frac{Q_*^2 + m_\pi^2}{Q_*^2 + m_{\pi,\text{phys}}^2} G_P^{u-d}(Q_*^2) \xrightarrow{m_\pi \to m_{\pi,\text{phys}}} g_P^*. \tag{5.32}$$

Using a modest extrapolation of our fit, we find $g_P^{\text{norm}} = 8.47(21)(87)(2)(7)$, which is consistent with the measurement by the MuCap experiment [6], $g_P^* = 8.06(55)$. We can also determine the residue of the pion pole: this is related to the pion decay constant F_π and the pion-nucleon coupling constant $g_{\pi NN}$ [57]

$$\lim_{Q^2 \to -m_\pi^2} (Q^2 + m_\pi^2) G_P^{u-d}(Q^2) = 4 m_N F_\pi g_{\pi NN}. \tag{5.33}$$

The required extrapolation in Q^2 is about twice as far as was required for g_P^*, but is still small compared with our probed range of Q^2. Using $F_\pi = 106$ MeV computed on this ensemble, we obtain $g_{\pi NN} = 11.5(4)(1.4)(1)(0)$. This is slightly more than one standard deviation below the recent result [17] determined using pion-nucleon scattering lengths from measurements of pionic atoms: $g_{\pi NN}^2/(4\pi) = 13.69(20)$, or $g_{\pi NN} = 13.12(10)$. In the chiral limit, the pion-nucleon coupling constant is related

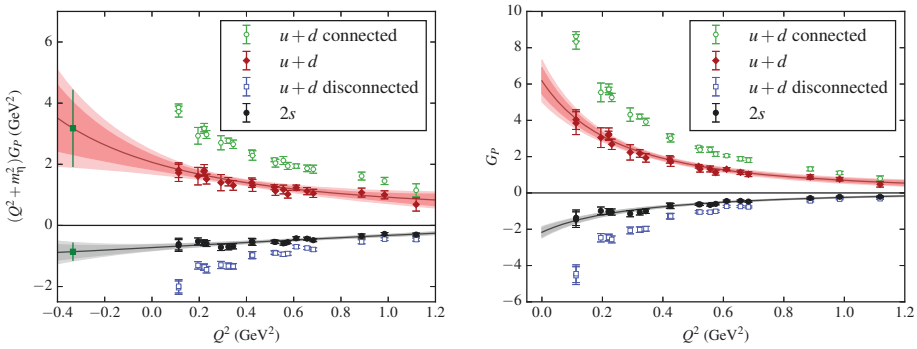

Figure 5-15: Light and strange isoscalar induced pseudoscalar form factors $G_P^{u+d}(Q^2)$ and $G_P^s(Q^2)$ and the z-expansion fits to them. In addition, for the light isoscalar form factor, the corresponding form factors for the renormalized connected and disconnected diagrams are also shown. The left plot shows the form factors with the eta pole removed (which is directly fitted using the z expansion), and the right plot has the pole restored in the fit curves. The left plot also shows the extrapolations to the eta pole. See the caption of Fig. 5-11.

to the axial charge via the Goldberger-Treiman relation, $g_{\pi NN} = g_A^{u-d} m_N / F_\pi$; on our ensemble the right hand side equals 12.1, and thus our precision is insufficient to resolve a nonzero Goldberger-Treiman discrepancy.

The isoscalar induced pseudoscalar form factors are shown in Fig. 5-15. As these contain an eta pole, we again remove the pole before fitting with the z expansion. The eta mass is estimated using the leading-order relation from partially quenched chiral perturbation theory, $m_\eta^2 = (m_\pi^2 + 2m_{\eta_s}^2)/3$, yielding $m_\eta \approx 578$ MeV. Relative to the connected diagrams, the contributions from disconnected diagrams are not small, which is in contrast with what we saw for the G_A form factors. This can be understood by considering the partially quenched theory, under which the connected contributions to $G_P^{u+d}(Q^2)$ are equal to $G_P^{u+d-2r}(Q^2)$, where r is a third valence light quark, degenerate with u and d. We would expect that this form factor has a pseudoscalar pole from the π_8 meson[6] (which is part of the octet of pseudo-Goldstone bosons under the exact $SU(3)$ symmetry of the valence u, d, and r quarks) at $Q^2 = -m_\pi^2$. The sharp rise of this form factor at low Q^2 is consistent with this expectation. Since the

[6]The presence of this pole was already argued in Ref. [93].

physical isoscalar form factor does not contain a pole at $Q^2 = -m_\pi^2$, the pole must be canceled by the disconnected diagrams, which explains why the disconnected contribution to G_P^{u+d} must also rise sharply (with opposite sign) at low Q^2. Similarly, the expectation that the octet axial current A_μ^8 couples more strongly than the singlet current A_μ^0 to the eta meson suggests that G_P^s and G_P^{u+d} should have opposite sign, as seen in the data.

We can attempt to quantify the couplings to the eta meson by studying the generalization of Eq. (5.33)

$$\lim_{Q^2 \to -m_\eta^2} (Q^2 + m_\eta^2) G_P^a(Q^2) = 2 m_N f_\eta^a g_{\eta NN}, \tag{5.34}$$

where the eta decay constants are defined[7] by $\langle 0 | A_\mu^a | \eta(p) \rangle = f_\eta^a p_\mu$ [52]. As Fig. 5-15 shows, the extrapolation to the eta pole is rather difficult and the results have a large uncertainty. Since we have not separately computed the eta decay constants on this ensemble, we cannot determine the eta-nucleon coupling constant in this way. However, we can take the singlet-octet ratio f_η^0 / f_η^8, which we find to be 0.96(16)(21)(4)(1). This is larger than expected, and three standard deviations above the value obtained from the phenomenological parameters in Ref. [52], $f_\eta^0 / f_\eta^8 = 0.16(3)$. In particular, since our pion mass is heavier than physical, we would expect the reduced breaking of flavor $SU(3)$ symmetry to yield a value closer to zero. This unexpected behavior is likely caused by the difficulty in such a large extrapolation in Q^2; direct calculations of these decay constants such as in Ref. [98] are much more reliable since they do not require a kinematical extrapolation. If we ignore this issue, and assume the $SU(3)$ relation $f_\eta^8 = f_\pi^3$, then from $G_P^8 \equiv (G_P^{u+d} - 2G_P^s)/\sqrt{6}$ we obtain an estimate for the eta-nucleon coupling constant, $g_{\eta NN} = 5.2(1.0)(1.0)(0.2)(0)$.

Assuming flavor $SU(3)$ symmetry, the eta-nucleon coupling constant can also be obtained from the connected contribution to G_P^{u+d}. Provided that the considerations from the partially quenched theory are valid, the residue of the pion pole is proportional to $F_\pi g_{\pi_8 NN}$, where the π_8-nucleon coupling constant is equal (up to $SU(3)$

[7] Note that using this definition for the pion decay constant would yield $f_\pi^3 = \sqrt{2} F_\pi$, where the physical value is $f_\pi^3 \approx 130$ MeV.

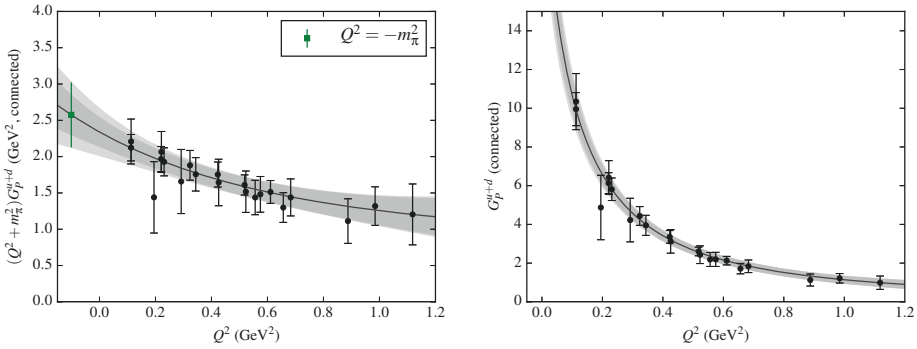

Figure 5-16: Connected light isoscalar induced pseudoscalar form factor $G_P^{u+d,\mathrm{conn}}(Q^2)$ and the z-expansion fit to it. See the caption of Fig. 5-14.

breaking corrections) to $g_{\eta NN}$. Alone, the connected contribution does not benefit from the cancellation of excited-state effects with the disconnected contribution that we have seen. Therefore, to better control these effects, we determine this form factor using the summation method in the same way as G_P^{u-d}; this is shown in Fig. 5-16. We obtain $g_{\pi_8 NN} = 3.29(35)(45)(3)(0)$. The eta-nucleon coupling constant is not so well known phenomenologically, but both of these estimates are compatible with the value obtained using a generalized Goldberger-Treiman relation, $g_{\eta NN} = 3.4(5)$ [53].

5.4 Discussion and conclusions

As with the previous study of electromagnetic form factors [65], our approach of using hierarchical probing for disconnected loops and high statistics for nucleon two-point functions is effective at producing a good signal for disconnected nucleon axial form factors. In contrast with the previous study, however, we find that the gauge noise is dominant over the noise from stochastic estimation of the loops, so that further improvements in the latter would be of limited value.

A useful feature of disconnected loops is that they can be reused for calculating many different observables. We did this for computing the axial renormalization factors nonperturbatively, and we were again able to obtain a reasonable signal. At the scale $\mu = 2$ GeV, the effect of mixing between light and strange axial currents

is small: $G_A^s(Q^2)$, which is most affected, is reduced in magnitude by up to 10%. The accuracy of our renormalization is limited by the unknown $O(\alpha^2)$ term in the matching of the flavor singlet axial current to the $\overline{\text{MS}}$ scheme. Our use of two different intermediate schemes may provide some estimate of this term, but it is possible that the effect in converting between the two intermediate schemes is smaller than in converting to $\overline{\text{MS}}$. A smaller flavor-singlet renormalization factor would make both g_A^{u+d+s} and f_η^0/f_η^8 more consistent with expectations. This highlights the need for higher-order conversion factors. In the flavor-nonsinglet case, these factors have been computed up to three-loop order for some operators [59, 60]. As lattice calculations of disconnected diagrams have made great progress, there is now a need for similar matching calculations in the flavor-singlet sector.

Since this work was performed using only one lattice ensemble, we do not provide an estimate of systematic uncertainties due to the heavier-than-physical pion mass or due to discretization effects. The former have been investigated in many lattice calculations of the isovector axial charge, where generally only modest effects have been seen. Generalizing this, we don't expect large dependence on the pion mass for $G_A^q(Q^2)$. On the other hand, the G_P form factors — especially the isovector one — will have a significant dependence on light quark masses due to the presence of pseudoscalar poles. Discretization effects for this lattice ensemble have been studied in Ref. [123], where it is compared with another ensemble with similar pion mass and smaller lattice spacing. The isovector axial charge computed on the two ensembles is consistent within one standard deviation, or about 3%, which gives a rough estimate of uncertainty due to finite lattice spacing. We expect that these effects are of similar size for other nucleon matrix elements involving the axial current.

We found that the statistical correlations between the values of a form factor at different Q^2 behave differently for connected and disconnected diagrams. In the latter case, data with different spatial momentum transfers are nearly uncorrelated. This has the result of better constraining fits to the form factors; using these fits, we were able to obtain a precise value for the strange axial charge on our ensemble, $g_A^s = -0.0240(21)(11)$, which is consistent with previous lattice calculations.

For $G_A(Q^2)$, the disconnected diagrams are small compared with the connected ones. For instance, $g_A^{u+d,\mathrm{disc}}/g_A^{u+d} = -0.17$, and the strange disconnected diagrams are about half as large as the light ones. However, this is somewhat larger than we saw for the electromagnetic form factors [65], where the disconnected light magnetic moment, $\mu^{u+d,\mathrm{disc}} \approx 0.11$, is about 4% of the full experimental value $\mu^{u+d} = 3(\mu^p + \mu^n) \approx 2.6$, and the disconnected $G_E(Q^2)$ is even smaller relative to the full experimental form factor. This may change closer to the physical pion mass, since the disconnected light-quark matrix elements are expected to grow as the quark mass is decreased.

For $G_P(Q^2)$, the situation is different, with disconnected diagrams not nearly as suppressed. This can be understood from the dominant influence of the pseudoscalar poles in these form factors, which leads to a significant cancellation between the connected and disconnected contributions to $G_P^{u+d}(Q^2)$. As the pion mass is decreased toward the physical point, we expect that $G_P^{u+d}(Q^2)$ will vary only mildly, but at low Q^2 the individual connected and disconnected contributions will become much larger since the location of the pion pole will approach $Q^2 = 0$. This growing cancellation may make it difficult to obtain a good signal for the full form factor at the physical pion mass and low Q^2.

Chapter 6

Summary

In this work, we have performed calculations of various nucleon structure observables using the framework of lattice QCD. This includes the calculations of the following observables:

- Nucleon isovector axial, scalar, and tensor charges.
- The nucleon isovector charge and axial radii, magnetic moment, and the induced pseudoscalar form factor at $Q^2 = 0$.
- The axial form factors of individual quark flavors.

The first two calculations were performed on two $2 + 1$-flavor ensembles with a 2-HEX-smeared Wilson-clover action and at the physical point with different lattice spacings. We have demonstrated control over excited-state contaminations by the use of multiple source-sink separations and employing different fitting strategies. The renormalization factors were computed using the Rome-Southampton approach.

As mentioned in the introduction, the nucleon axial charge is experimentally well known, its PDG value is $g_A = 1.2724(23)$, which provides a crucial test for lattice QCD. Unlike the axial charge, the scalar and tensor charges are much less well-determined from phenomenology. Our final measurements of the axial and tensor charges have uncertainties of roughly 4%. Within errors, our estimate of the axial charge is compatible with the value quoted by the PDG. While we were able to

reproduce the axial charge at the level of 4%, the experimental result is more precise by an order of magnitude. We found a much larger uncertainty in the case of the scalar charge which is due to the large uncertainty found in the renormalization factor and the large difference we observe in the central values between the two ensembles.

On the same two ensembles mentioned before, we performed calculations of the isovector electromagnetic and axial nucleon form factors. We presented a momentum-derivative approach for the computation of nucleon form factors at zero momentum transfer in addition to the direct evaluation of the charge and axial radii. This approach is model-independent and helps to avoid the large extrapolation included in the traditional approach for computing such quantities. We presented two variants of the derivative approach, one where we compute momentum derivatives of the matrix elements with respect to the initial-state momentum and another variant that involves the computation of mixed-derivatives with respect to both the initial- and final-state momenta. We found that both derivative approaches suffer from large statistical uncertainties when compared to the traditional approach, although the mixed-derivative approach was successful in reducing the statistical uncertainties on the nucleon radii and $G_P(0)$ compared to the first variant of that method. Additionally, we had significant inconsistencies between the two ensembles for the form factors at $Q^2 = 0$ which indicates that the finite volume and the discretization effects are significant in those cases.

The third study in this work is a continuation of a previous one that was performed by our group where the strange electromagnetic form factors were computed on a single lattice ensembles with close-to-physical parameters [65]. The used lattice includes 2+1 flavors of dynamical see quarks, implemented using a clover-improved Wilson action and with a pion mass of 317 MeV. For computing the nucleon form factors of the strange quark, the disconnected loops need to be evaluated. The disconnected loops can then be contracted with two-point functions to evaluate the disconnected contributions to the three-point functions. We showed that using the hierarchical probing for disconnected loops and high statistics for nucleon two-point functions is effective at producing a good signal for the disconnected nucleon axial form factors.

We found that for $G_A(Q^2)$, the disconnected contribution is small compared to the connected one and the strange contribution is about half as large as the light one. In contrast to $G_A(Q^2)$, we found that for $G_P(Q^2)$ and relative to the connected diagrams, the disconnected diagrams are not small which is due to the existence of pseudoscalar poles. In addition, we computed the total contribution from quark spin to the nucleon spin and found it to be about half at $\mu = 2$ GeV, which is larger than the phenomenological determination of 0.18 to 0.28.

Calculations for this project were done using the Qlua software suite [104], and some of them made use of the QOPQDP adaptive multigrid solver [11, 101]. Fixing to Landau gauge was done using the Fourier-accelerated conjugate gradient algorithm [78].

Bibliography

[1] A. Abdel-Rehim et al. "Disconnected quark loop contributions to nucleon observables in lattice QCD". In: *Phys. Rev. D* 89 (2014), p. 034501. DOI: 10.1103/PhysRevD.89.034501. arXiv: 1310.6339 [hep-lat].

[2] M. Albanese et al. "Glueball Masses and String Tension in Lattice QCD". In: *Phys. Lett.* B192 (1987), pp. 163–169. DOI: 10.1016/0370-2693(87)91160-9.

[3] C. Alexandrou et al. "Nucleon scalar and tensor charges using lattice QCD simulations at the physical value of the pion mass". In: *Phys. Rev. D* 95 (2017). [erratum: Phys. Rev. D **96** (2017) 099906], p. 114514. DOI: 10.1103/PhysRevD.95.114514. arXiv: 1703.08788 [hep-lat].

[4] Constantia Alexandrou et al. "Nucleon spin and quark content at the physical point". In: *PoS* LATTICE2016 (2016), p. 153. arXiv: 1611.09163 [hep-lat].

[5] Constantia Alexandrou et al. "Nucleon axial form factors using $N_f = 2$ twisted mass fermions with a physical value of the pion mass". In: *Phys. Rev. D* 96 (2017), p. 054507. DOI: 10.1103/PhysRevD.96.054507. arXiv: 1705.03399 [hep-lat].

[6] V. A. Andreev et al. "Measurement of Muon Capture on the Proton to 1% Precision and Determination of the Pseudoscalar Coupling g_P". In: *Phys. Rev. Lett.* 110 (2013), p. 012504. DOI: 10.1103/PhysRevLett.110.012504. arXiv: 1210.6545 [nucl-ex].

[7] Aldo Antognini et al. "Proton Structure from the Measurement of 2S-2P Transition Frequencies of Muonic Hydrogen". In: *Science* 339.6118 (2013), pp. 417–420. ISSN: 0036-8075. DOI: 10.1126/science.1230016.

[8] S. Aoki et al. “FLAG Review 2019”. In: (2019). arXiv: 1902.08191 [hep-lat].

[9] Yasumichi Aoki et al. “Nucleon isovector structure functions in (2+1)-flavor QCD with domain wall fermions”. In: *Phys. Rev. D* 82 (2010), p. 014501. DOI: 10.1103/PhysRevD.82.014501. arXiv: 1003.3387 [hep-lat].

[10] J. Ashman et al. “A Measurement of the Spin Asymmetry and Determination of the Structure Function g_1 in Deep Inelastic Muon-Proton Scattering”. In: *Phys. Lett. B* 206 (1988), p. 364. DOI: 10.1016/0370-2693(88)91523-7.

[11] R. Babich et al. “Adaptive multigrid algorithm for the lattice Wilson-Dirac operator”. In: *Phys. Rev. Lett.* 105 (2010), p. 201602. DOI: 10.1103/PhysRevLett.105.201602. arXiv: 1005.3043 [hep-lat].

[12] P. A. Baikov and K. G. Chetyrkin. “New four loop results in QCD”. In: *Nucl. Phys. B (Proc. Suppl.)* 160 (2006), pp. 76–79. DOI: 10.1016/j.nuclphysbps.2006.09.031.

[13] G. S. Bali et al. “Strangeness Contribution to the Proton Spin from Lattice QCD”. In: *Phys. Rev. Lett.* 108 (2012), p. 222001. DOI: 10.1103/PhysRevLett.108.222001. arXiv: 1112.3354 [hep-lat].

[14] G. S. Bali et al. “Non-perturbative renormalization of flavor singlet quark bilinear operators in lattice QCD”. In: *PoS* LATTICE2016 (2016), p. 187. arXiv: 1703.03745 [hep-lat].

[15] Gunnar S. Bali et al. “Nucleon isovector couplings from $N_f = 2$ lattice QCD”. In: *Phys. Rev. D* 91 (2015), p. 054501. DOI: 10.1103/PhysRevD.91.054501. arXiv: 1412.7336 [hep-lat].

[16] Oliver Bär. “Chiral perturbation theory and nucleon–pion-state contaminations in lattice QCD”. In: *Int. J. Mod. Phys.* A32.15 (2017), p. 1730011. DOI: 10.1142/S0217751X17300113. arXiv: 1705.02806 [hep-lat].

[17] V. Baru et al. “Precision calculation of the $\pi^- d$ scattering length and its impact on threshold πN scattering”. In: *Phys. Lett. B* 694 (2011), pp. 473–477. DOI: 10.1016/j.physletb.2010.10.028. arXiv: 1003.4444 [nucl-th].

[18] Silas R. Beane and Martin J. Savage. "Baryon axial charge in a finite volume". In: *Phys. Rev. D* 70 (2004), p. 074029. DOI: 10.1103/PhysRevD.70.074029. arXiv: hep-ph/0404131.

[19] Paulo F. Bedaque. "Aharonov-Bohm effect and nucleon nucleon phase shifts on the lattice". In: *Phys. Lett.* B593 (2004), pp. 82–88. DOI: 10.1016/j.physletb.2004.04.045. arXiv: nucl-th/0402051 [nucl-th].

[20] J. C. Bernauer et al. "High-precision determination of the electric and magnetic form factors of the proton". In: *Phys. Rev. Lett.* 105 (2010), p. 242001. DOI: 10.1103/PhysRevLett.105.242001. arXiv: 1007.5076 [nucl-ex].

[21] Bhubanjyoti Bhattacharya, Richard J. Hill, and Gil Paz. "Model independent determination of the axial mass parameter in quasielastic neutrino-nucleon scattering". In: *Phys. Rev.* D84 (2011), p. 073006. DOI: 10.1103/PhysRevD.84.073006. arXiv: 1108.0423 [hep-ph].

[22] Bhubanjyoti Bhattacharya, Gil Paz, and Anthony J. Tropiano. "Model-independent determination of the axial mass parameter in quasielastic antineutrino-nucleon scattering". In: *Phys. Rev.* D92.11 (2015), p. 113011. DOI: 10.1103/PhysRevD.92.113011. arXiv: 1510.05652 [hep-ph].

[23] Tanmoy Bhattacharya et al. "Improved bilinears in lattice QCD with non-degenerate quarks". In: *Phys. Rev. D* 73 (2006), p. 034504. DOI: 10.1103/PhysRevD.73.034504. arXiv: hep-lat/0511014.

[24] Tanmoy Bhattacharya et al. "Probing Novel Scalar and Tensor Interactions from (Ultra)Cold Neutrons to the LHC". In: *Phys. Rev. D* 85 (2012), p. 054512. DOI: 10.1103/PhysRevD.85.054512. arXiv: 1110.6448 [hep-ph].

[25] Tanmoy Bhattacharya et al. "Dimension-5 CP-odd operators: QCD mixing and renormalization". In: *Phys. Rev. D* 92 (2015), p. 114026. DOI: 10.1103/PhysRevD.92.114026. arXiv: 1502.07325 [hep-ph].

[26] Tanmoy Bhattacharya et al. "Axial, Scalar and Tensor Charges of the Nucleon from 2 + 1 + 1-flavor Lattice QCD". In: *Phys. Rev. D* 94 (2016), p. 054508. DOI: 10.1103/PhysRevD.94.054508. arXiv: 1606.07049 [hep-lat].

[27] Thomas Blum, Taku Izubuchi, and Eigo Shintani. "New class of variance-reduction techniques using lattice symmetries". In: *Phys. Rev. D* 88 (2013), p. 094503. DOI: 10.1103/PhysRevD.88.094503. arXiv: 1208.4349 [hep-lat].

[28] Philippe Boucaud et al. "Quark propagator and vertex: Systematic corrections of hypercubic artifacts from lattice simulations". In: *Phys. Lett. B* 575 (2003), pp. 256–267. DOI: 10.1016/j.physletb.2003.08.065. arXiv: hep-lat/0307026.

[29] Philippe Boucaud et al. "Artifacts and A^2 power corrections: Reexamining $Z_\psi(p^2)$ and Z_V in the momentum-subtraction scheme". In: *Phys. Rev. D* 74 (2006), p. 034505. DOI: 10.1103/PhysRevD.74.034505. arXiv: hep-lat/0504017.

[30] Ph. Boucaud et al. "mu-Squared Dependent Deviation of the Non Perturbative ZA,MOM from the True Axial Renormalisation Constant, Implied by Ward Identity". In: (2015). arXiv: 1503.09083 [hep-lat].

[31] K. C. Bowler et al. "First lattice study of semileptonic decays of Λ_b and Ξ_b baryons". In: *Phys. Rev.* D57 (1998), pp. 6948–6974. DOI: 10.1103/PhysRevD.57.6948. arXiv: hep-lat/9709028 [hep-lat].

[32] J. Bulava, M. A. Donnellan, and Rainer Sommer. "The $B^*B\pi$ Coupling in the Static Limit". In: *PoS* LATTICE2010 (2010), p. 303. arXiv: 1011.4393 [hep-lat].

[33] Stefano Capitani. "Lattice perturbation theory". In: *Phys. Rept.* 382 (2003), pp. 113–302. DOI: 10.1016/S0370-1573(03)00211-4. arXiv: hep-lat/0211036 [hep-lat].

[34] Stefano Capitani, Stephan Dürr, and Christian Hoelbling. "Rationale for UV-filtered clover fermions". In: *JHEP* 11 (2006), p. 028. DOI: 10.1088/1126-6708/2006/11/028. arXiv: hep-lat/0607006 [hep-lat].

[35] Stefano Capitani et al. "Non-perturbative quark mass renormalization in quenched lattice QCD". In: *Nucl. Phys. B* 544 (1999). [Erratum: Nucl. Phys. B 582, 762 (2000)], pp. 669–698. DOI: 10.1016/S0550-3213(98)00857-8. arXiv: hep-lat/9810063.

[36] Stefano Capitani et al. "Systematic errors in extracting nucleon properties from lattice QCD". In: *PoS* LATTICE2010 (2010), p. 147. arXiv: 1011.1358 [hep-lat].

[37] Stefano Capitani et al. "Isovector axial form factors of the nucleon in two-flavor lattice QCD". In: *Int. J. Mod. Phys. A* 34.02 (2019), p. 1950009. DOI: 10.1142/S0217751X1950009X. arXiv: 1705.06186 [hep-lat].

[38] S. Capitani et al. "Nucleon electromagnetic form factors in two-flavor QCD". In: *Phys. Rev.* D92.5 (2015), p. 054511. DOI: 10.1103/PhysRevD.92.054511. arXiv: 1504.04628 [hep-lat].

[39] A. J. Chambers et al. "A novel approach to nonperturbative renormalization of singlet and nonsinglet lattice operators". In: *Phys. Lett. B* 740 (2015), pp. 30–35. DOI: 10.1016/j.physletb.2014.11.033. arXiv: 1410.3078 [hep-lat].

[40] A. J. Chambers et al. "Disconnected contributions to the spin of the nucleon". In: *Phys. Rev. D* 92 (2015), p. 114517. DOI: 10.1103/PhysRevD.92.114517. arXiv: 1508.06856 [hep-lat].

[41] C. C. Chang et al. "A per-cent-level determination of the nucleon axial coupling from quantum chromodynamics". In: *Nature* 558.7708 (2018), pp. 91–94. DOI: 10.1038/s41586-018-0161-8. arXiv: 1805.12130 [hep-lat].

[42] K. G. Chetyrkin. "Quark mass anomalous dimension to $O(\alpha_s^4)$". In: *Phys. Lett. B* 404 (1997), pp. 161–165. DOI: 10.1016/S0370-2693(97)00535-2. arXiv: hep-ph/9703278.

[43] K. G. Chetyrkin and A. Rétey. "Renormalization and running of quark mass and field in the regularization invariant and $\overline{\text{MS}}$ schemes at three loops and four loops". In: *Nucl. Phys. B* 583 (2000), pp. 3–34. DOI: 10.1016/S0550-3213(00)00331-X. arXiv: hep-ph/9910332.

[44] M. Constantinou et al. "Singlet versus nonsinglet perturbative renormalization of fermion bilinears". In: *Phys. Rev. D* 94 (2016), p. 114513. DOI: 10.1103/PhysRevD.94.114513. arXiv: 1610.06744 [hep-lat].

[45] G. M. de Divitiis, R. Petronzio, and N. Tantalo. "On the discretization of physical momenta in lattice QCD". In: *Phys. Lett.* B595 (2004), pp. 408–413. DOI: 10.1016/j.physletb.2004.06.035. arXiv: hep-lat/0405002 [hep-lat].

[46] G. M. de Divitiis, R. Petronzio, and N. Tantalo. "On the extraction of zero momentum form factors on the lattice". In: *Phys. Lett.* B718 (2012), pp. 589–596. DOI: 10.1016/j.physletb.2012.10.035. arXiv: 1208.5914 [hep-lat].

[47] R. J. Dowdall et al. "The Upsilon spectrum and the determination of the lattice spacing from lattice QCD including charm quarks in the sea". In: *Phys. Rev. D* 85 (2012), p. 054509. DOI: 10.1103/PhysRevD.85.054509. arXiv: 1110.6887 [hep-lat].

[48] Stephan Dürr et al. "Lattice QCD at the physical point meets SU(2) chiral perturbation theory". In: *Phys. Rev.* D90.11 (2014), p. 114504. DOI: 10.1103/PhysRevD.90.114504. arXiv: 1310.3626 [hep-lat].

[49] S. Dürr et al. "Lattice QCD at the physical point: Simulation and analysis details". In: *JHEP* 08 (2011), p. 148. DOI: 10.1007/JHEP08(2011)148. arXiv: 1011.2711 [hep-lat].

[50] M. Engelhardt. "Strange quark contributions to nucleon mass and spin from lattice QCD". In: *Phys. Rev. D* 86 (2012), p. 114510. DOI: 10.1103/PhysRevD.86.114510. arXiv: 1210.0025 [hep-lat].

[51] Zachary Epstein, Gil Paz, and Joydeep Roy. "Model independent extraction of the proton magnetic radius from electron scattering". In: *Phys. Rev.* D90.7 (2014), p. 074027. DOI: 10.1103/PhysRevD.90.074027. arXiv: 1407.5683 [hep-ph].

[52] T. Feldmann, P. Kroll, and B. Stech. "Mixing and decay constants of pseudoscalar mesons". In: *Phys. Rev. D* 58 (1998), p. 114006. DOI: 10.1103/PhysRevD.58.114006. arXiv: hep-ph/9802409 [hep-ph].

[53] Thorsten Feldmann. "Quark structure of pseudoscalar mesons". In: *Int. J. Mod. Phys. A* 15 (2000), pp. 159–207. DOI: 10.1142/S0217751X00000082. arXiv: hep-ph/9907491.

[54] Daniel de Florian et al. "Extraction of Spin-Dependent Parton Densities and Their Uncertainties". In: *Phys. Rev. D* 80 (2009), p. 034030. DOI: 10.1103/PhysRevD.80.034030. arXiv: 0904.3821 [hep-ph].

[55] Justin Foley et al. "Practical all-to-all propagators for lattice QCD". In: *Comput. Phys. Commun.* 172 (2005), pp. 145–162. DOI: 10.1016/j.cpc.2005.06.008. arXiv: hep-lat/0505023.

[56] V. Giménez et al. "Non-perturbative renormalization of lattice operators in coordinate space". In: *Phys. Lett. B* 598 (2004), pp. 227–236. DOI: 10.1016/j.physletb.2004.07.053. arXiv: hep-lat/0406019.

[57] M. L. Goldberger and S. B. Treiman. "Form Factors in β Decay and μ Capture". In: *Phys. Rev.* 111 (1958), pp. 354–361. DOI: 10.1103/PhysRev.111.354.

[58] Martín González-Alonso and Jorge Martin Camalich. "Isospin breaking in the nucleon mass and the sensitivity of β decays to new physics". In: *Phys. Rev. Lett.* 112 (2014), p. 042501. DOI: 10.1103/PhysRevLett.112.042501. arXiv: 1309.4434 [hep-ph].

[59] J. A. Gracey. "Three loop anomalous dimension of non-singlet quark currents in the RI′ scheme". In: *Nucl. Phys. B* 662 (2003), pp. 247–278. DOI: 10.1016/S0550-3213(03)00335-3. arXiv: hep-ph/0304113.

[60] J. A. Gracey. "Three loop anomalous dimensions of higher moments of the non-singlet twist-2 Wilson and transversity operators in the $\overline{\text{MS}}$ and RI′ schemes". In: *JHEP* 10 (2006), p. 040. DOI: 10.1088/1126-6708/2006/10/040. arXiv: hep-ph/0609231.

[61] J. A. Gracey. "RI′/SMOM scheme amplitudes for quark currents at two loops". In: *Eur. Phys. J. C* 71 (2011), p. 1567. DOI: 10.1140/epjc/s10052-011-1567-8. arXiv: 1101.5266 [hep-ph].

[62] J. R. Green et al. "Nucleon Scalar and Tensor Charges from Lattice QCD with Light Wilson Quarks". In: *Phys. Rev. D* 86 (2012), p. 114509. DOI: 10.1103/PhysRevD.86.114509. arXiv: 1206.4527 [hep-lat].

[63] J. R. Green et al. "Nucleon Structure from Lattice QCD Using a Nearly Physical Pion Mass". In: *Phys. Lett. B* 734 (2014), pp. 290–295. DOI: 10.1016/j.physletb.2014.05.075. arXiv: 1209.1687 [hep-lat].

[64] Jeremy Green et al. "Nucleon form factors with light Wilson quarks". In: *PoS* LATTICE2013 (2014), p. 276. arXiv: 1310.7043 [hep-lat].

[65] Jeremy Green et al. "High-precision calculation of the strange nucleon electromagnetic form factors". In: *Phys. Rev. D* 92 (2015), p. 031501. DOI: 10.1103/PhysRevD.92.031501. arXiv: 1505.01803 [hep-lat].

[66] Jeremy Green et al. "Up, down, and strange nucleon axial form factors from lattice QCD". In: *Phys. Rev.* D95.11 (2017), p. 114502. DOI: 10.1103/PhysRevD.95.114502. arXiv: 1703.06703 [hep-lat].

[67] Keith Griffioen, Carl Carlson, and Sarah Maddox. "Consistency of electron scattering data with a small proton radius". In: *Phys. Rev.* C93.6 (2016), p. 065207. DOI: 10.1103/PhysRevC.93.065207. arXiv: 1509.06676 [nucl-ex].

[68] Rajan Gupta et al. "Isovector Charges of the Nucleon from $2 + 1 + 1$-flavor Lattice QCD". In: *Phys. Rev. D* 98 (2018), p. 034503. DOI: 10.1103/PhysRevD.98.034503. arXiv: 1806.09006 [hep-lat].

[69] S. Güsken. "A Study of smearing techniques for hadron correlation functions". In: *Nucl. Phys. Proc. Suppl.* 17 (1990), pp. 361–364. DOI: 10.1016/0920-5632(90)90273-W.

[70] Maxwell T. Hansen and Harvey B. Meyer. "On the effect of excited states in lattice calculations of the nucleon axial charge". In: *Nucl. Phys. B* 923 (2017), pp. 558–587. DOI: 10.1016/j.nuclphysb.2017.08.017. arXiv: 1610.03843 [hep-lat].

[71] Tim Harris et al. "Nucleon isovector charges and twist-2 matrix elements with $N_f = 2 + 1$ dynamical Wilson quarks". In: (2019). arXiv: 1905.01291 [hep-lat].

[72] Nesreen Hasan et al. "Computing the nucleon Dirac radius directly at $Q^2 = 0$". In: *PoS* LATTICE2016 (2016), p. 147. DOI: 10.22323/1.256.0147. arXiv: 1611.01383 [hep-lat].

[73] Nesreen Hasan et al. "Nucleon radii and form factors at $Q^2 = 0$ using momentum derivatives". The 35th International Symposium on Lattice Field Theory (Lattice 2017), Granada, Spain. 2017. URL: https://makondo.ugr.es/event/0/session/95/contribution/279.

[74] Nesreen Hasan et al. "Computing the nucleon charge and axial radii directly at $Q^2 = 0$ in lattice QCD". In: *Phys. Rev. D* 97 (2018), p. 034504. DOI: 10.1103/PhysRevD.97.034504. arXiv: 1711.11385 [hep-lat].

[75] Nesreen Hasan et al. "Nucleon axial, scalar, and tensor charges using lattice QCD at the physical pion mass". In: (2019). arXiv: 1903.06487 [hep-lat].

[76] Douglas W. Higinbotham et al. "Proton radius from electron scattering data". In: *Phys. Rev.* C93.5 (2016), p. 055207. DOI: 10.1103/PhysRevC.93.055207. arXiv: 1510.01293 [nucl-ex].

[77] Richard J. Hill and Gil Paz. "Model independent extraction of the proton charge radius from electron scattering". In: *Phys. Rev.* D82 (2010), p. 113005. DOI: 10.1103/PhysRevD.82.113005. arXiv: 1008.4619 [hep-ph].

[78] R. J. Hudspith. "Fourier Accelerated Conjugate Gradient Lattice Gauge Fixing". In: *Comput. Phys. Commun.* 187 (2015), pp. 115–119. DOI: 10.1016/j.cpc.2014.10.017. arXiv: 1405.5812 [hep-lat].

[79] Ken-Ichi Ishikawa et al. "Nucleon form factors on a large volume lattice near the physical point in 2+1 flavor QCD". In: *Phys. Rev. D* 98 (2018), p. 074510. DOI: 10.1103/PhysRevD.98.074510. arXiv: 1807.03974 [hep-lat].

[80] Karl Jansen et al. "Nonperturbative renormalization of lattice QCD at all scales". In: *Phys. Lett.* B372 (1996), pp. 275–282. DOI: 10.1016/0370-2693(96)00075-5. arXiv: hep-lat/9512009 [hep-lat].

[81] Elizabeth Ellen Jenkins and Aneesh V. Manohar. "Baryon chiral perturbation theory using a heavy fermion Lagrangian". In: *Phys. Lett. B* 255 (1991), pp. 558–562. DOI: 10.1016/0370-2693(91)90266-S.

[82] Xiangdong Ji. "Gauge-Invariant Decomposition of Nucleon Spin". In: *Phys. Rev. Lett.* 78 (4 Jan. 1997), pp. 610–613. DOI: 10.1103/PhysRevLett.78.610. URL: https://link.aps.org/doi/10.1103/PhysRevLett.78.610.

[83] F. -J. Jiang and B. C. Tiburzi. "Flavor Twisted Boundary Conditions and the Nucleon Vector Current". In: *Phys. Rev. D* 78 (2008), p. 114505. DOI: 10.1103/PhysRevD.78.114505. arXiv: 0810.1495 [hep-lat].

[84] J. J. Kelly. "Simple parametrization of nucleon form factors". In: *Phys. Rev.* C70 (2004), p. 068202. DOI: 10.1103/PhysRevC.70.068202.

[85] Jiro Kodaira. "QCD Higher Order Effects in Polarized Electroproduction: Flavor Singlet Coefficient Functions". In: *Nucl. Phys. B* 165 (1980), pp. 129–140. DOI: 10.1016/0550-3213(80)90310-7.

[86] Yuri V. Kovchegov, Daniel Pitonyak, and Matthew D. Sievert. "Small-x asymptotics of the quark helicity distribution". In: *Phys. Rev. Lett.* 118 (2017), p. 052001. DOI: 10.1103/PhysRevLett.118.052001. arXiv: 1610.06188 [hep-ph].

[87] S. A. Larin. "The Renormalization of the axial anomaly in dimensional regularization". In: *Phys. Lett. B* 303 (1993), pp. 113–118. DOI: 10.1016/0370-2693(93)90053-K. arXiv: hep-ph/9302240.

[88] Olivier Ledoit and Michael Wolf. "A well-conditioned estimator for large-dimensional covariance matrices". In: *Journal of Multivariate Analysis* 88.2 (2004), pp. 365–411. DOI: 10.1016/S0047-259X(03)00096-4.

[89] T. Ledwig et al. "Octet-baryon axial-vector charges and SU(3)-breaking effects in the semileptonic hyperon decays". In: *Phys. Rev. D* 90 (2014), p. 054502. DOI: 10.1103/PhysRevD.90.054502. arXiv: 1405.5456 [hep-ph].

[90] G. Peter Lepage. "The Analysis of Algorithms for Lattice Field Theory". In: *Boulder ASI 1989:97-120*. 1989, pp. 97–120.

[91] Jian Liang et al. "Quark spins and Anomalous Ward Identity". In: *Phys. Rev. D* 98 (2018), p. 074505. DOI: 10.1103/PhysRevD.98.074505. arXiv: 1806.08366 [hep-ph].

[92] Huey-Wen Lin et al. "First Monte Carlo Global Analysis of Nucleon Transversity with Lattice QCD Constraints". In: *Phys. Rev. Lett.* 120 (2018), p. 152502. DOI: 10.1103/PhysRevLett.120.152502. arXiv: 1710.09858 [hep-ph].

[93] Keh-Fei Liu. "Flavor singlet axial charge of the nucleon and anomalous Ward identity". In: *Phys. Lett. B* 281 (1992), pp. 141–147. DOI: 10.1016/0370-2693(92)90288-F.

[94] I. T. Lorenz and Ulf-G. Meißner. "Reduction of the proton radius discrepancy by 3σ". In: *Phys. Lett.* B737 (2014), pp. 57–59. DOI: 10.1016/j.physletb.2014.08.010. arXiv: 1406.2962 [hep-ph].

[95] G. Martinelli and C.T. Sachrajda. "A lattice study of nucleon structure". In: *Nuclear Physics B* 316.2 (1989), pp. 355–372. ISSN: 0550-3213. DOI: https://doi.org/10.1016/0550-3213(89)90035-7.

[96] G. Martinelli et al. "A General method for nonperturbative renormalization of lattice operators". In: *Nucl. Phys.* B445 (1995), pp. 81–108. DOI: 10.1016/0550-3213(95)00126-D. arXiv: hep-lat/9411010 [hep-lat].

[97] Aaron S. Meyer et al. "Deuterium target data for precision neutrino-nucleus cross sections". In: *Phys. Rev. D* 93 (2016), p. 113015. DOI: 10.1103/PhysRevD.93.113015. arXiv: 1603.03048 [hep-ph].

[98] Chris Michael, Konstantin Ottnad, and Carsten Urbach. "η and η' masses and decay constants from lattice QCD with $N_f = 2 + 1 + 1$ quark flavours". In: *PoS* LATTICE2013 (2014), p. 253. arXiv: 1311.5490 [hep-lat].

[99] Peter J. Mohr, David B. Newell, and Barry N. Taylor. "CODATA Recommended Values of the Fundamental Physical Constants: 2014". In: *Rev. Mod. Phys.* 88.3 (2016), p. 035009. DOI: 10.1103/RevModPhys.88.035009. arXiv: 1507.07956 [physics.atom-ph].

[100] Emanuele R. Nocera et al. "A first unbiased global determination of polarized PDFs and their uncertainties". In: *Nucl. Phys. B* 887 (2014), pp. 276–308. DOI: 10.1016/j.nuclphysb.2014.08.008. arXiv: 1406.5539 [hep-ph].

[101] James Osborn et al. *QOPQDP*. URL: https://usqcd-software.github.io/qopqdp/.

[102] V. Papavassiliou. "Strangeness in the Nucleon, Cold Dark Matter in the Universe, and Neutrino Scattering off Liquid Argon". In: *AIP Conf. Proc.* 1222 (2010), pp. 186–190. DOI: 10.1063/1.3399287.

[103] C. Patrignani et al. "Review of Particle Physics". In: *Chin. Phys. C* 40 (2016), p. 100001. DOI: 10.1088/1674-1137/40/10/100001.

[104] Andrew Pochinsky. *Qlua*. https://usqcd.lns.mit.edu/qlua.

[105] Randolf Pohl et al. "The size of the proton". In: *Nature* 466.7303 (2010), pp. 213–216. ISSN: 0028-0836. DOI: 10.1038/nature09250.

[106] Randolf Pohl et al. "Laser spectroscopy of muonic deuterium". In: *Science* 353.6300 (2016), pp. 669–673. ISSN: 0036-8075. DOI: 10.1126/science.aaf2468.

[107] Randolf Pohl et al. "Deuteron charge radius and Rydberg constant from spectroscopy data in atomic deuterium". In: *Metrologia* 54 (2017), p. L1. DOI: 10.1088/1681-7575/aa4e59. arXiv: 1607.03165 [physics.atom-ph].

[108] G. M. Prosperi, M. Raciti, and C. Simolo. "On the running coupling constant in QCD". In: *Prog. Part. Nucl. Phys.* 58 (2007), pp. 387–438. DOI: 10.1016/j.ppnp.2006.09.001. arXiv: hep-ph/0607209.

[109] Shoichi Sasaki and Takeshi Yamazaki. "Nucleon form factors from quenched lattice QCD with domain wall fermions". In: *Phys. Rev.* D78 (2008), p. 014510. DOI: 10.1103/PhysRevD.78.014510. arXiv: 0709.3150 [hep-lat].

[110] Nobuo Sato et al. "Iterative Monte Carlo analysis of spin-dependent parton distributions". In: *Phys. Rev. D* 93 (2016), p. 074005. DOI: 10.1103/PhysRevD.93.074005. arXiv: 1601.07782 [hep-ph].

[111] Juliane Schäfer and Korbinian Strimmer. "A Shrinkage Approach to Large-Scale Covariance Matrix Estimation and Implications for Functional Genomics". In: *Statistical Applications in Genetics and Molecular Biology* 4.1 (2005). DOI: 10.2202/1544-6115.1175.

[112] Eigo Shintani et al. "Covariant approximation averaging". In: *Phys. Rev.* D91.11 (2015), p. 114511. DOI: 10.1103/PhysRevD.91.114511. arXiv: 1402.0244 [hep-lat].

[113] Eigo Shintani et al. "Nucleon form factors and root-mean-square radii on a $(10.8\ \mathrm{fm})^4$ lattice at the physical point". In: *Phys. Rev. D* 99 (2019), p. 014510. DOI: 10.1103/PhysRevD.99.014510. arXiv: 1811.07292 [hep-lat].

[114] A. Skouroupathis and H. Panagopoulos. "Two-loop renormalization of vector, axial-vector and tensor fermion bilinears on the lattice". In: *Phys. Rev. D* 79

(2009), p. 094508. DOI: 10.1103/PhysRevD.79.094508. arXiv: 0811.4264 [hep-lat].

[115] Andreas Stathopoulos, Jesse Laeuchli, and Kostas Orginos. "Hierarchical probing for estimating the trace of the matrix inverse on toroidal lattices". In: *SIAM J. Sci. Comput.* 35(5) (2013), S299–S322. DOI: 10.1137/120881452. arXiv: 1302.4018 [hep-lat].

[116] S. N. Syritsyn et al. "Nucleon electromagnetic form factors from lattice QCD using $2+1$ flavor domain wall fermions on fine lattices and chiral perturbation theory". In: *Phys. Rev. D* 81 (3 2010), p. 034507. DOI: 10.1103/PhysRevD.81.034507.

[117] M. Tanabashi et al. "Review of Particle Physics". In: *Phys. Rev. D* 98 (3 2018), p. 030001. DOI: 10.1103/PhysRevD.98.030001.

[118] Brian C. Tiburzi. "Chiral Corrections to Nucleon Two- and Three-Point Correlation Functions". In: *Phys. Rev. D* 91 (2015), p. 094510. DOI: 10.1103/PhysRevD.91.094510. arXiv: 1503.06329 [hep-lat].

[119] J. A. M. Vermaseren, S. A. Larin, and T. van Ritbergen. "The 4-loop quark mass anomalous dimension and the invariant quark mass". In: *Phys. Lett. B* 405 (1997), pp. 327–333. DOI: 10.1016/S0370-2693(97)00660-6. arXiv: hep-ph/9703284.

[120] Walter Wilcox. "Noise methods for flavor singlet quantities". In: *Numerical Challenges in Lattice Quantum Chromodynamics*. Ed. by Andreas Frommer et al. Vol. 15. Lecture Notes in Computational Science and Engineering. Springer Berlin Heidelberg, 2000, pp. 127–141. ISBN: 978-3-540-67732-1. DOI: 10.1007/978-3-642-58333-9_10. arXiv: hep-lat/9911013.

[121] Nodoka Yamanaka et al. "Nucleon charges with dynamical overlap fermions". In: *Phys. Rev. D* 98 (2018), p. 054516. DOI: 10.1103/PhysRevD.98.054516. arXiv: 1805.10507 [hep-lat].

[122] Zhihong Ye et al. “Unveiling the nucleon tensor charge at Jefferson Lab: A study of the SoLID case”. In: *Phys. Lett. B* 767 (2017), pp. 91–98. DOI: 10.1016/j.physletb.2017.01.046. arXiv: 1609.02449 [hep-ph].

[123] Boram Yoon et al. “Isovector charges of the nucleon from 2+1-flavor QCD with clover fermions”. In: *Phys. Rev. D* 95 (2017), p. 074508. DOI: 10.1103/PhysRevD.95.074508. arXiv: 1611.07452 [hep-lat].

Band / Volume 29
Computer simulation of pedestrian dynamics at high densities
C. Eilhardt (2015), viii, 142 pp
ISBN: 978-3-95806-032-6
URN: urn:nbn:de:0001-2015020502

Band / Volume 30
Efficient Task-Local I/O Operations of Massively Parallel Applications
W. Frings (2016), xiv, 140 pp
ISBN: 978-3-95806-152-1
URN: urn:nbn:de:0001-2016062000

Band / Volume 31
A study on buoyancy-driven flows: Using particle image velocimetry for validating the Fire Dynamics Simulator
by A. Meunders (2016), xxi, 150 pp
ISBN: 978-3-95806-173-6
URN: urn:nbn:de:0001-2016091517

Band / Volume 32
Methoden für die Bemessung der Leistungsfähigkeit multidirektional genutzter Fußverkehrsanlagen
S. Holl (2016), xii, 170 pp
ISBN: 978-3-95806-191-0
URN: urn:nbn:de:0001-2016120103

Band / Volume 33
JSC Guest Student Programme Proceedings 2016
edited by I. Kabadshow (2017), iii, 191 pp
ISBN: 978-3-95806-225-2
URN: urn:nbn:de:0001-2017032106

Band / Volume 34
Multivariate Methods for Life Safety Analysis in Case of Fire
B. Schröder (2017), x, 222 pp
ISBN: 978-3-95806-254-2
URN: urn:nbn:de:0001-2017081810

Band / Volume 35
Understanding the formation of wait states in one-sided communication
M.-A. Hermanns (2018), xiv, 144 pp
ISBN: 978-3-95806-297-9
URN: urn:nbn:de:0001-2018012504

Band / Volume 36
A multigrid perspective on the parallel full approximation scheme in space and time
D. Moser (2018), vi, 131 pp
ISBN: 978-3-95806-315-0
URN: urn:nbn:de:0001-2018031401

Band / Volume 37
Analysis of I/O Requirements of Scientific Applications
S. El Sayed Mohamed (2018), XV, 199 pp
ISBN: 978-3-95806-344-0
URN: urn:nbn:de:0001-2018071801

Band / Volume 38
Wayfinding and Perception Abilities for Pedestrian Simulations
E. Andresen (2018), 4, x, 162 pp
ISBN: 978-3-95806-375-4
URN: urn:nbn:de:0001-2018121810

Band / Volume 39
Real-Time Simulation and Prognosis of Smoke Propagation in Compartments Using a GPU
A. Küsters (2018), xvii, 162, LIX pp
ISBN: 978-3-95806-379-2
URN: urn:nbn:de:0001-2018121902

Band / Volume 40
Extreme Data Workshop 2018
Forschungszentrum Jülich, 18-19 September 2018
Proceedings
M. Schultz, D. Pleiter, P. Bauer (Eds.) (2019), 64 pp
ISBN: 978-3-95806-392-1
URN: urn:nbn:de:0001-2019032102

Band / Volume 41
A lattice QCD study of nucleon structure with physical quark masses
N. Hasan (2020), xiii, 157 pp
ISBN: 978-3-95806-456-0
URN: urn:nbn:de:0001-2020012307

Weitere ***Schriften des Verlags im Forschungszentrum Jülich*** unter
http://wwwzb1.fz-juelich.de/verlagextern1/index.asp

IAS Series
Band / Volume 41
ISBN 978-3-95806-456-0

Mitglied der Helmholtz-Gemeinschaft

JÜLICH
Forschungszentrum